Numerical modelling of current transfer in nonlinear anisotropic conductive media

Robert Paul Baranowski

Fitzwilliam College

Cambridge

A dissertation submitted for the degree of Doctor of Philosophy at the University of Cambridge

April 1999

For my mum,
and in loving memory of my father.

Preface

I declare that, except where otherwise stated, this dissertation is the result of my own work and includes nothing which is the outcome of work done in collaboration. No part of this dissertation has been submitted at Cambridge or any other University for a degree, diploma, or other qualification. Some of the work contained in this dissertation has been published.

Robert Paul Baranowski
April 1999

Numerical modelling of current transfer in nonlinear anisotropic conductive media

Summary

Current transfer behaviour in anisotropic superconducting bodies is the central topic of this thesis and focuses on the effect that the nonlinearity of the electric field dependence upon the local current density value and anisotropy have on the nature of current transport. The main motivation for this work was the desire for a better understanding of the conceptually difficult behaviour of current transport in superconducting bodies and examines current transfer quantitatively for a number of important problems on the macroscopic and microscopic scale. This behaviour is examined both experimentally and using computer models. The successful development of a powerful, robust and adaptable numerical model for analysing the complex current transfer behaviour has been the primary aim of this work.

The range of parameters appropriate to macroscopic models of the Bi-2212 CRT system has been experimentally examined using a specifically constructed apparatus for the measurement of current transport characteristics. A study of the self-field properties of the Bi-2212 CRT material using a new experimental technique and mathematical analysis is presented and has allowed the importance of the self-field effect in the numerical model to be assessed. An essential requirement for the practical application of high current superconducting devices is the development of low resistance current contacts. The research presented examines this macroscopic current transfer problem and aims to explain experimentally observed current transfer characteristics at high applied currents. Existing models cannot explain these characteristics. Current transfer on the microscopic scale is also examined. Models of current transfer have been developed from descriptions of specific microstructures that are thought to characterise the microstructure of Bi-2223 and Bi-2212 silver-sheathed tapes. This thesis specifically presents modelling of current transfer between c-axis, low-angle c-axis and edge-on c-axis tilt oriented grain interfaces; the principal current transfer paths between individual current elements of the microstructural models of current flow in polycrystalline HTSs.

Acknowledgements

Foremost, I would like to thank my supervisor *Prof. Jan E. Evetts* for his continuing generous support and critical analysis. Our discussions were invaluable and helped maintain a sense of perspective.

I would also like to thank both *Dan R. Watson* and *Ahmed Kursomovic* for experimental data from electrical measurements of *in-situ* current contacts and *Makan Chen* for samples and the transport measurements included in figure 3.7. I also gratefully acknowledge the assistance of *Dr Archie M. Campbell* in calculating the dimensionally consistent value of t^* of section 5.5 and the assistance of *Nikolaos Adamopoulos* in deriving a method to calculate aspects of the magnetic field profile directly from transport data.

I thank the *Department of Materials Science and Metallurgy* and the *Interdisciplinary Centre in Superconductivity* for the generous provision of their facilities; and *Oxford Instruments* and the *EPSRC* for the generous provision of their money. I would like to thank the numerous scientists that have come and gone over the period of my research at the above named institutions and *7 St Barnabas Rd* for their contributions to the atmosphere in which I worked. I should like to thank *Richard Mosely, Robert Herzog* and *Gavin Burnell* for computer support and *Wilfred Booij* and *John Durrel* for computer time.

I further wish to express my gratitude to the *Department of Engineering* for access to their computer facilities and to *Ms C. A. Salkield* and *Miss S. M. Unwin* for computer support. I also wish to express my appreciation to *Dr Tim J. Flack* and *Dr Arul Britto* for valuable discussions on the subject of numerical and finite element modelling.

I am especially grateful to *Vincent Baranowski* for computer hardware and software (and other) support, without which this work would have taken much longer to complete. I also wish express my thanks to *Alan Baranowski* for financial services rendered along with the rest *my family* for their support in my academic endeavours.

I also have to thank *Dan R. Watson* for being the Krusty to my Sideshow, and for many helpful discussions on subjects ranging from current flow in HTSs to back posture. I must also say that I greatly appreciated *Estella Chesneau* for empathising on the subject of computer modelling and *Steve Isaacs* for stupefying cheeriness ‘in the fight between you and the world’. Finally, I would like to thank *Konrad Bishop* for this state of grace.

Contents

Index of symbols

The use of units complies with the SI convention and units style conventions agree with BIPM standards[1]. A right hand rectangular Cartesian co-ordinate frame with axes x, y and z is used throughout this thesis when discussing physical spaces and is referred to as the global co-ordinate frame. Local Cartesian co-ordinate frames have axes x', y' and z'. Scalars and the magnitude of vectors are shown in italics; vectors and matrices in bold.

μ_0	permeability of free space ($4\pi\times10^{-7} = 12.566...\times10^{-7}$ N·A^{-2})[2]
h	Planks constant (6.6260755×10^{-34} J·s)[2]
e	elementary charge (1.60217733×10^{-19} C)[2]
k_B	Boltzmann constant (1.380658×10^{-23} J·K^{-1})[2]
Φ_0	magnetic flux quantum ($h/2e = 2.06783461\times10^{-15}$ T·m^2)[2]
H	magnetic field strength
E	electric field strength
J	current density vector
B	magnetic field
w	width
t	thickness
l	length
T	temperature
T_c	critical temperature
λ	magnetic penetration depth
λ_L	London magnetic penetration depth
m	effective mass of the superconducting electrons
e_s	effective charge of the superconducting electrons
n_s	density of the superconducting electrons
ψ	superconducting order parameter
ξ	Ginzberg-Landau coherence length
κ	Ginzberg-Landau parameter (λ/ξ)
H_c	thermodynamic critical field
H_{c1}	lower critical field strength
H_{c2}	upper critical field strength
$\mathbf{F}_L$	Lorentz force per unit volume
ρ_f	flux flow resistivity
U_L	energy of the Lorentz force ($U_L = J_c B V_c$)
V_c	volume of flux subject to a Lorentz force
η	flux line jump rate

ω_0	flux line vibration frequency
U	effective activation energy
U_{AK}	effective activation energy of the Anderson-Kim model
I_{app}	applied current
I_c	critical current; usually defined by a voltage criterion
n	critical exponent, where $E \propto J^n$
E_c	critical electric field value
J_c	critical current density; usually defined by a voltage criterion
$J_{c,x}$	x-component of the critical current density
$J_{c,y}$	y-component of the critical current density
J_x	x-component of the current density
J_y	y-component of the current density
α	critical current anisotropy ratio $\alpha = J_{c,x'} / J_{c,y'}$
$J_{c,c}$	critical current density along the crystallographic c-axis
$J_{c,ab}$	critical current density along the crystallographic ab-plane
J_c^{norm}	critical current normal to the tape plane
J^m	macroscopic average current density
J_c^m	macroscopic average critical current density
ρ_n	resistivity in normal region
$\rho_{x'}$	resistivity in the x' axis direction
$\rho_{y'}$	resistivity in the y' axis direction
ρ_c	resistivity in the crystallographic c-axis direction
ρ_{ab}	resistivity in the crystallographic ab-plane
R	sample radius
ΔM	irreversible magnetisation
Λ	current scaling length
$B_\perp$	applied magnetic field perpendicular to the tape plane
$B_\parallel$	applied magnetic field parallel to the tape plane
θ	angle of the applied magnetic field to the tape plane
ϕ_m	effective mean misalignment angle
$B_{c\perp}^*$	critical magnetic field component normal to the tape plane
$J_{c\parallel}$	critical current density value measured with the applied magnetic field parallel to the tape plane
$J_{c\perp}$	critical current density value measured for applied magnetic field perpendicular to the tape plane
H_{irr}	irreversibility field strength
$J_{c,ab}\left(H_{\parallel ab}\right)$	critical current density along the ab plane for applied magnetic field parallel to the tape plane
$J_{c,ab}\left(H_{\perp ab}\right)$	critical current density along the ab plane for applied magnetic field perpendicular to the tape plane

H_x	x-component of the magnetic field strength
H_y	y-component of the magnetic field strength
H_z	z-component of the magnetic field strength
H_{sf}	self-field strength
H_{app}	applied field strength
H^*	the value of H_{app} applied parallel to the surface of a sample and perpendicular to the current for which the field inside the sample is zero at one surface
H_A	field strength at position A in superconducting sample
H_B	field strength at position B in superconducting sample
J_A	current density at position A in superconducting sample
J_B	current density at position B in superconducting sample
ΔH	$H_B - H_A$
ΔH_{sf}	value of ΔH at zero applied field
α_c	propagation constant of TL model
R_c	resistance of a current contact
ΔV	total voltage drop across a current contact
d	length of current contact
ρ_{cm}	resistivity of the contact metal of current contact
R'	transmission line series resistance per unit length
G'	transmission line parallel shunt line conductance per unit length
ρ_i	current contact interface resistivity
t_s	superconductor thickness of *in-situ* or lap current contacts
ϕ_{gc}	angle between the c-axes of two connected colonies/grains
P_{gc}	normalised power dissipation calculated from solutions of the LAC and EOC models
γ	aspect ratio
f	source function
n	vector normal to boundary
D	a smooth function (functional coefficient of Ficks law)
u	unknown function
$\hat{u}$	approximation to u (trial function)
v	test function
Ω	any domain
Ω^e	the domain of an element
Γ	boundary of Ω, or the Gamma function
Γ_u	boundary where Dirirchlet boundary condition applies
Γ_q	boundary where Neumann boundary condition applies
Γ_u^e	element boundary where Dirichlet boundary condition applies

Γ_q^e	element boundary where Neumann boundary condition applies
$\mathbf{N}^e, N_{ji}^e$	element shape matrix and the components of $\mathbf{N}^e$
l, m, n	local nodes on linear triangular element
$\mathbf{U}^e, U_i^e$	nodal values of the solution variables on a particular element and the components of $\mathbf{U}^e$
A^e	element area
$\mathbf{K}^e, K_{ji}^e$	element stiffness matrix and components of $\mathbf{K}^e$
$\mathbf{f}^e, f_j^e$	element load vector and components of $\mathbf{f}^e$
$\mathbf{M}^e, M_{ji}^e$	element damping matrix and components of $\mathbf{M}^e$
$\mathbf{K}, K_{ji}$	global stiffness matrix and components of $\mathbf{K}$
$\mathbf{f}, f_j$	global load vector and components of $\mathbf{f}$
$\mathbf{M}, M_{ji}$	global damping matrix and components of $\mathbf{M}$
$\mathbf{U}$	nodal points of Ω

Index of abbreviations

HTS	high temperature superconductor
Bi-2212	$Bi_2Sr_2CaCu_2O_x$
Y-123	$YBa_2Cu_3O_x$
EJ	the electric field dependence upon the local current density value
Bi-2223	$Bi_2Sr_2Ca_2Cu_3O_x$
TAFF	thermally assisted flux flow
PIT	powder-in-tube
CRT	the composite reaction texturing method
IEEE	Institute of Electrical and Electronics Engineers
SCPI	Standard Communications for Programmable Instruments
ACS	a.c. susceptibility
PDE	partial differential equation
FE	finite element
BE	boundary element
FD	finite difference
TL	the Murrmann-Widmann current contact model
LAC	low-angle c-axis
EOC	edge-on c-axis

References

1 *The International System of Units (SI)* (U. S. Govt. Printing Office, Washington D.C., 1998).

2 E. R. Cohen and B. N. Taylor, Journal of Research of the National Bureau of Standards **92,** 85-95 (1987).

CHAPTER 1

Introduction and thesis overview

1.1 Introduction

The phenomenon of superconductivity was first discovered by Heike Kamerlingh Onnes and his colleagues in 1911. While studying the temperature dependence of the d.c. electrical resistivity of mercury, it was observed that, over a small temperature interval, the measured value of the resistivity of mercury became zero below a temperature of around 4.2 K. The temperature at which this effect occurs is known as the critical temperature T_c. The material undergoes a transition from the resistive (normal) state to the superconducting state when the temperature rises above this characteristic critical value. Further investigation revealed that the normal state of a superconductor can be restored at a temperature below T_c by applying a magnetic field, known as the thermodynamic critical field, H_c. Superconductors also exhibit the property of perfect diamagnetism, often referred to as the Meissner effect, which was discovered by Meissner and Ochsenfeld[1]. They observed that, not only is magnetic flux excluded from a superconductor below T_c, consistent with the expected behaviour of a perfect conductor, but also that at a field below H_c magnetic flux is expelled from the interior of an originally normal sample as it is cooled through the transition temperature. Various theoretical descriptions of the underlying physics of superconducting bodies have been proposed and are discussed in chapter 2.

In 1986 Bednorz and Müller[2] discovered a new superconducting compound in the La-Ba-Cu-O system that has a T_c of 35 K. This was the first of a new class of materials called high temperature superconductors (HTSs). Since this discovery, a number of HTSs have been found, including $Bi_2Sr_2CaCu_2O_x$ (Bi-2212) and $YBa_2Cu_3O_x$ (Y-123); the subscript x indicates the content/doping of an individual element in the compound. The highest T_c currently reported is 164 K[3]. These materials have a number of other properties that distinguish them from their low temperature counterparts. These include larger theoretical values for the maximum magnetic field under which HTSs can prevent full

penetration of magnetic flux and a layered structure that results in highly anisotropic physical properties. However, the principal technological significance of the discovery of HTSs is that most are superconducting at temperatures above the boiling point of liquid nitrogen, rather than helium in the case of low temperature superconductors. This reduces cooling power costs, affords easier cryogenic management, and thereby offers substantial potential for the practical application of HTSs.

1.2 Subject and aim of this thesis

Current transfer behaviour in anisotropic superconducting bodies is the central topic of this thesis. This behaviour is examined both experimentally and using computer models. The main motivation for this work has been the desire for a better understanding of the conceptually difficult behaviour of current transport in superconducting bodies. This study focuses on the effect that the anisotropy and nonlinearity of the electric field dependence upon the local current density value (EJ characteristic) have on the nature of current transport. Local transport properties on the macroscopic and microscopic scales have been found to play an important, and often dominant, role in the global (macroscopic) transfer of transport current. The recent review by Prester[4] of current transfer and initial dissipation in HTSs introduces the topic by asking the following question. *'What do the current paths in high-T_c superconductors (HTSs) really look like on various spatial scales and how are these paths determined by local properties?'*

Given reasonable assumptions, this thesis hopes to answer this question quantitatively for a number of important problems on the macroscopic and microscopic scale. In order to answer this question a uniquely powerful, robust and adaptable numerical model for analysing this complex nonlinear current transfer behaviour has been developed; the mathematical description, exhaustive model validation and computer implementation of which are described. The numerical model represents a useful tool for analysing current transport behaviour in anisotropic nonlinear conductive media and the successful development of a model has been the primary aim of this work.

The models developed examine current transport in nonlinear media and are therefore applicable to superconducting systems in general. However they principally, but not exclusively, model the behaviour of the composite reaction textured Bi-2212 system, and for this reason the range of parameters appropriate to macroscopic models has been examined experimentally. A study of the self-field properties of the composite reaction

textured Bi-2212 material is also presented and examines a basic assumption of the mathematical description of the current flow models.

An essential requirement for the practical application of high current superconducting devices is the development of low resistance current contacts. Research has concentrated on processing techniques that reduce the value of the contact interface resistance, and little work has been done on the nature of current transfer through current contacts to bulk superconductors. The research presented examines this macroscopic current transfer problem and aims to explain experimentally observed current transfer characteristics at high applied currents. Existing models cannot explain these characteristics. Furthermore, this system allows the comparison of experimentally accessible physical parameters with the results of numerical models of similar systems.

Current transfer on the microscopic scale is also examined. Bulk superconductor optimisation has focused upon understanding the current transfer mechanism within the microstructure of polycrystalline HTSs. Models of current transfer have been developed from descriptions of the specific microstructure characterising the real material and have concentrated on the microstructure of $Bi_2Sr_2Ca_2Cu_3O_x$ (Bi-2223) and Bi-2212 silver-sheathed tapes. This thesis specifically presents modelling of current transfer between c-axis, low-angle c-axis, and edge-on c-axis tilt oriented grain interfaces. These grain connexions represent the principal current transfer paths between individual current elements of the microstructures of these models. Quantitative and qualitative results have been derived from these mainly qualitative microstructural descriptions.

1.3 Overview of the thesis

This chapter has presented a short summary of some of the history of superconductivity as well as a brief discussion of the specific subject area and objectives of this thesis. An overview of the individual chapters of the thesis is also outlined here.

Chapter 2 presents a brief introduction to the theory of critical currents in type II superconductors and focuses on the principal concepts used in this thesis. These include the nonlinearity of the EJ characteristic, the critical state, anisotropy, and microstructural models of current transfer in HTSs. Some aspects of the basic phenomenological theory are also discussed.

Chapter 3 describes the experimental equipment and techniques used. The processing methods and basic electrodynamic characteristics of composite reaction textured Bi-2212 are the subject of the first part of this chapter. An apparatus for the measurement of current transport characteristics has been constructed and is described. A study of the self-field properties of the composite reaction textured Bi-2212 material using a new experimental technique is presented. A mathematical analysis is also outlined that enables part of the magnetic field profile to be deduced directly from transport measurements.

Chapter 4 discusses the principal approaches used in the numerical solution of partial differential equations and introduces the electromagnetic formulation used to express mathematically the physical model of current flow as a partial differential equation. An overview of the finite element representation employed in the numerical solution of the partial differential equation is presented and examined in detail. The computational efficiency and accuracy of various numerical solution methods have been examined and are reported. The issues involved in developing and executing the data processing and visualisation programs used in this work are also considered.

Chapter 5 presents a comparison of the solutions of numerical models against exact analytical solutions and the solutions of problems that can be arrived at intuitively. The validity of the finite element technique and computer implementation is verified by the comparison of results with intuitive and analytical models in the steady state and transient regimes for both isotropic and anisotropic models. Further verification is derived from the comparison of the solutions of a steady state and a transient model in the long-time limit for the isotropic and anisotropic cases. A preliminary discussion of the characteristic behaviour of current flow in nonlinear conductive media is presented and the specific case of current transport near macroscopic defects that form permanent barriers to current flow in superconductors is considered. A discussion of active current paths in polycrystalline superconductors is presented in chapter 7.

Chapter 6 describes modelling of current transport in the contact region of *in-situ* current contacts to isotropic and anisotropic HTSs. The nature of current transport in this system is examined and three different models are presented. The numerical solutions of various models are compared to the results of experimental studies of current transfer in *in-situ* current contacts to composite reaction textured Bi-2212.

Chapter 7 presents modelling of current transfer between c-axis, low-angle c-axis, and edge-on c-axis tilt oriented grain interfaces. The brick-wall and railway-switch models are reviewed. The first part of this chapter examines current transfer behaviour in a weak link free brick-wall model. The later part of this chapter presents the results of a model of current transfer in strongly connected low-angle c-axis and edge-on c-axis tilt grain boundaries.

Chapter 8 reviews the principal conclusions presented in this thesis. Modifications to the numerical model developed in this work and studies of other interesting current flow problems that could be analysed are suggested.

1.4 References

1 W. Meissner and R. Ochsenfeld, Naturwissenschaften **21,** 787 (1933).

2 G. Bednorz and K. A. Müller, Z. Phys. **B64,** 189 (1986).

3 L. Gao, Y. Y. Xue, F. Chen, Q. Xiong, R. L. Meng, D. Ramirez, C. W. Chu, J. H. Eggert, and H. K. Mao, Physical Review B-Condensed Matter **50,** 4260-4263 (1994).

4 M. Prester, Superconductor Science & Technology **11,** 333-357 (1998).

CHAPTER 2

Magnetic flux and critical currents in high-T_C superconductors

2.1 Basic phenomenological theory

Two years after the discovery of the Meissner effect, the first phenomenological theory to describe the properties of a superconducting body was proposed by H. London and F. London. They derived the following electrodynamic equations

$$\mathbf{E} = \frac{\delta}{\delta t}\left(\lambda_L{}^2 \mu_0 \mathbf{J}\right) \tag{2.1}$$

$$\mathbf{B} = -\nabla \times \left(\lambda_L{}^2 \mu_0 \mathbf{J}\right) \tag{2.2}$$

where

$$\lambda_L{}^2 = \frac{m}{\mu_0 n_s e_s{}^2} \tag{2.3}$$

and m, e_s and n_s are the effective mass, the effective charge, and the density of the superconducting electrons respectively. The zero resistivity property of a superconductor cannot be described by Ohm's law and is replaced by equation (2.1) which describes the acceleration of the superconducting electrons by an electric field in the absence of scattering. The solution of equation (2.2) and the fourth Maxwell equation ($\mu_0 \mathbf{J} = \nabla \times \mathbf{B}$) with respect to the magnetic field in the quasi-static limit describes an exponential decay of the magnetic field at the surface of a superconductor with characteristic length scale, λ_L, called the London penetration depth.

The phenomenological theory of Ginzburg and Landau is based on the theory of the second order phase transition at the superconducting transition and as such only really applies near T_c, however it is often used outside this realm of applicability. Ginzburg and Landau proposed that a complex pseudo-wavefunction, ψ, describe the order parameter of the superconducting electrons. The density of the superconducting electrons, n_s, is represented by the square of the modulus of the order parameter, $|\psi|^2$, which is zero in the

normal state. Ginzburg-Landau theory derives two coupled differential equations from the minimisation of the Gibbs free energy functional as represented by a series expansion in powers of $|\psi|^2$. Two important length scales, ξ and λ, which are closely related to the coefficients of these differential equations can be introduced and determine the scale of the spatial variations of the order parameter and the magnetic field respectively.

Abrisokov calculated[1] general solutions of the Ginzburg-Landau differential equations, which can be classified into two groups depending on the value of the Ginzburg-Landau parameter, $\kappa = \lambda/\xi$. If κ is less than $1/\sqrt{2}$ the surface energy between a superconducting and a normal region within a sample is positive (type I). As a consequence, the superconducting state undergoes a sudden transition to the normal state on the application of magnetic fields greater than H_c (in samples with zero demagnetisation factor). However, if κ is greater than $1/\sqrt{2}$ the surface energy is negative (type II) and the superconducting state exhibits perfect diamagnetism only in applied field strengths less than the lower critical field, H_{c1}. At applied field strengths greater than H_{c1} the magnetic field penetrates the sample as a periodic structure of flux tubes (the flux line lattice) with each tube containing one flux quantum, Φ_0, ($h/2e = 2.07\times10^{-15}$ T·m^2). For a type II superconductor it becomes favourable energetically to enter a mixed state of superconducting and normal regions. The mixed state persists until the upper critical field value, H_{c2}, is reached. The flux line lattice was first observed directly by Essman and Träuble[2] in 1967 by a decoration technique in which iron particles were evaporated onto the surface of a mixed state superconductor.

2.2 Flux lines in type II superconductors

Attractive forces can trap moving flux lines as they pass defects within a sample and ‘pin’ them to the site of the defect. Motion of the flux line lattice leads to the dissipation of energy and the loss of the perfect conducting state. Even in the pinned state, the resistivity is not exactly zero at temperatures above absolute zero, because flux lines can become thermally activated and move between pinning sites. This resistive component influences the EJ characteristic. The nature of flux pinning, the thermal activation of flux lines, and the representation of the EJ characteristic are dealt with in this section.

2.2.1 Flux pinning in type II superconductors

Flux lines predominantly experience an attractive 'pinning' force to defects within a superconducting sample. Defects create a local variation in the free energy of the superconducting system and thereby attract flux lines to low energy sites where the order parameter is locally depressed. Pinning forces also arise from magnetic and vortex current energy distribution considerations. For example, thin films with thickness variations can trap flux at locations of smallest thickness where the flux lines are shortest and therefore the magnetic energy at a minimum.

The application of an external current to a type II superconductor in the mixed state produces a Lorentz force, per unit volume, of

$$\mathbf{F}_L = \mathbf{J} \times \mathbf{B} . \tag{2.4}$$

In the absence of pinning sites, flux lines move freely under the influence of this Lorentz force and, according to Faraday's law, induce electric fields in a direction normal to their movement and the magnetic field direction. This leads to the dissipation of energy and consequently the presence of an electrical resistance. Pinning sites prevent flux lines from moving and hence dissipation.

If the Lorentz force density exceeds the pinning force and removes flux lines from pinning centres, the flux lines begin to move and dissipate energy. The current density necessary to produce such a Lorentz force is known as the critical current density[3], J_c. The free movement of flux lines is called flux flow and a simple model of the dissipation mechanism of flux motion was developed by Bardeen and Stephen. Their model suggests that the resistivity of a superconductor in the flux flow state, ρ_f, can be expressed as

$$\rho_f = \frac{E}{J} = \rho_n \frac{H}{H_{c2}} \tag{2.5}$$

where ρ_n is the normal state resistivity of the superconducting material.

2.2.2 The thermal activation of flux lines in type II superconductors

Even when the pinning force is stronger than the Lorentz force (originating from the transport current) thermal fluctuations enable pinned flux lines or flux bundles to jump from one pinning centre to another by overcoming the intervening energy barrier, U_0 (pinning potential). This hopping motion leads to a diffusive motion of flux in the direction of the Lorentz force. In the absence of an applied transport current, thermal activation causes the flux distribution to slowly equilibrate randomly and therefore with

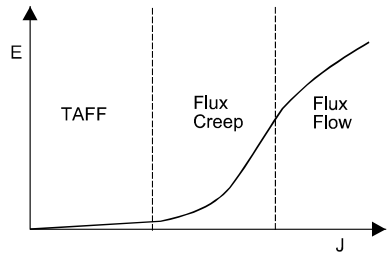

Figure 2.1
The EJ characteristic, indicating different dissipative regimes.

no net voltage developed. Below J_c, flux creep and thermally assisted flux flow (TAFF) are the two principal regimes of thermally activated flux motion and represent limiting cases of a thermally activated flux hopping model first proposed by Anderson and Kim[4,5].

The flux creep regime differs from the TAFF regime in the amount of energy associated with the Lorentz force, $U_L = J_c B V_c$, relative to the thermal energy, $k_B T$; V_c is the volume of the flux subject to the Lorentz force. The activation of a flux line can occur if the sum of these two energies exceeds the energy barrier U_0. Flux creep occurs when $U_L >> k_B T$, whereas TAFF occurs when $U_L << k_B T$ and requires a comparatively smaller current density to unpin flux lines. The flux motion mechanisms of TAFF, flux creep and flux flow lead to three regimes of dissipation within the superconductor as characterised by the different dependencies of the electric field and current density, as described by the EJ curve of figure 2.1.

Models of thermally activated flux motion principally use the Arrhenius rate equation to describe the effective jump rate of flux lines

$$\eta = \omega_0 \exp\left(-U/k_B T\right) \tag{2.6}$$

where ω_0 is a characteristic vibration frequency of the flux lines and U the effective activation energy. Models differ in the functional form of the activation energy and are either physically or phenomenologically based. The simplest model is the Anderson-Kim model, which assumes an effective activation energy of the form

$$U_{AK}\left(1 - J/J_c\right)$$

and corresponds to a sawtooth shaped pinning potential tilted by the energy potential of the applied current. Further developments of this model provide a more realistic shape, for which U can be written

$$U_{AK}\left(1 - J/J_c\right)^p$$

where the exponent $p = 1.5 - 2$ is related to the curvature of the pin potential (see figure 2.2). Other models include the phenomenological logarithmic[6] and the vortex-glass[7] activation barrier functions.

2.2.3 Flux creep and the EJ characteristic

The electric field due to flux creep can be written as

$$E = J\rho_0 \exp\left(-U\left(J/J_c, B, T\right)/k_B T\right) \tag{2.7}$$

where ρ_0 is an effective flux flow resistivity[8] and the exponential term gives the probability of a thermally activated flux hop. On substitution of the activation barrier function into equation (2.7), various expressions for the EJ curve can be obtained. These are often employed in the numerous studies examining magnetic diffusion in 1D and rectangular geometries possessing electrical material properties governed by a nonlinear EJ characteristic. Gurevich has performed theoretical analyses of nonlinear flux diffusion[9] and shows that the relaxation of the electric field proves to be similar for different models while the long-time decay of the magnetic moment is essentially model dependent.

The model presented in this thesis introduces an alternative numerical method of generating solutions to flux diffusion problems, however the principal aim of this thesis is to analyse the current transfer behaviour in nonlinear media as few studies have examined this. Throughout this work, I use a power law expression for the EJ characteristic of the superconducting electrically conductive media, which in the isotropic case is of the form

$$\mathbf{E}(J) = E_c \left|J/J_c\right|^n \mathbf{J}/J \qquad \text{where } 1 \le n < \infty. \tag{2.8}$$

This power law behaviour is observed in numerous experiments, including the experimental work on Bi-2212 presented in this thesis, and was used in theories on creep[10,11] and flux penetration[12,13]. This corresponds to the logarithmic current dependence of the activation energy described in the previous section. This representation in isotropic form contains only two independent parameters, $E_c/J_c^{\,n}$ and n, and interpolates from Ohmic ($n=1$) behaviour over the creep regime ($n=2-20$) to hard superconductors with Bean behaviour ($n \to \infty$).

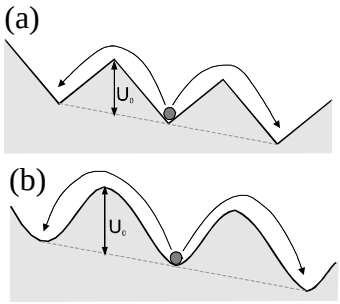

Figure 2.2
(a) Tilted sawtooth pinning potential. (b) Sawtooth pinning potential with curvature. The hopping motion of a flux line is indicated schematically.

The nonlinear nature of the EJ characteristic can also be attributed to sample inhomogeneity. The curved EJ characteristics of heterogeneous structures such as multifilamentary composites and granular superconductors can often be approximated using the power law expression of equation (2.8). It has been shown that the degree of inhomogeneity of a sample is directly related to the n-value of the EJ curve and that $n \approx \left(\langle J_c \rangle / \sigma_J\right)^{5/3}$; where $\langle J_c \rangle$ is the mean critical current density and σ_J the standard deviation

of $\langle J_c \rangle$. The critical current, I_c, is often defined as the current at which the electric field reaches some specific critical value, E_c, and a value of 1×10^{-4} V·m^{-1} is used throughout the rest of this thesis. The critical current density is typically defined as the critical current divided by the cross sectional area through which current flows normal to the plane of the area. If this cross section covers the entire plane through the superconductor then this is referred to as the macroscopic critical current density, J_c^m, to differentiate this current density from the local critical current density.

2.3 The critical state model

Critical state models describe how the spatial distribution of magnetic flux within a sample changes when applied fields or currents change. The presence of pinning centres impedes the movement of magnetic flux within a superconducting sample. The pinning of magnetic flux creates a flux gradient inwards from the sample surface and gives rise to irreversible magnetisation and hysteresis. The concept of the critical state was introduced independently by Bean[14,15] and London[16], and assumes that the magnitude of the local current density is either zero or equal to the critical current density. Solutions of the magnetic field distribution, and hence the current distribution and magnetisation, in a sample can be determined from the force balance equation, which equates the pinning forces within the sample to the magnetic driving force

$$BJ_c = \left|\mathbf{B}\times\left(\nabla\times\mathbf{H}\right)\right|. \qquad (2.9)$$

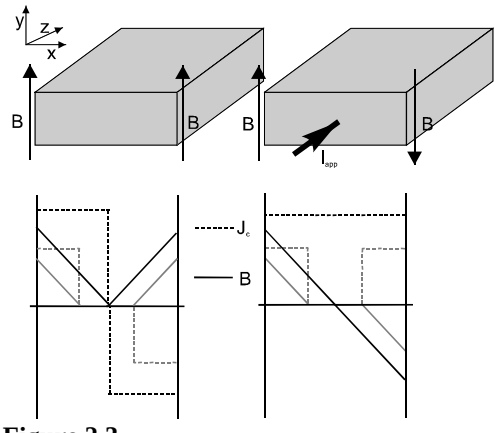

Figure 2.3
Local magnetic flux density profile, according to the critical state model, in a slab geometry for increasing applied magnetic field and applied current, I_{app}. Grey and black lines indicate two different applied field and current values.

Regions within a sample at which the local current density exceeds the critical current density enter the resistive flux flow state, as determined by the EJ characteristic of the sample. This allows further magnetic flux penetration until the local current density value again equals the critical state value. Reversing the applied field leads to a set of negative currents penetrating from the sample surface and reducing the local field value. Examples of the local flux density profile, according to the Bean critical state model, in the rectangular slab geometry in

uniform applied field and self-field are shown schematically in figure 2.3.

The Bean model of the critical state assumes that the value of the critical current density is constant and independent of the local value of the magnetic field. Extensions of the Bean model that use phenomenological expressions to take into account a local magnetic field dependence of the critical current can also be used but the Bean approximation is often more than sufficient for a first approximation. The magnetic field distribution in superconducting bodies with rectangular slab and other simple geometries have been calculated using numerical computer models[17] and are often calculated using the Bean approximation[12,18]. As previously mentioned, the numerical simulations presented in this thesis also calculate the magnetic flux distribution but present the results as an analysis of current distribution.

2.4 Models of current transfer in polycrystalline HTS

Polycrystalline high-T_c superconductors consist of an array of superconducting particles, which are to some degree weakly linked. Current transfer within this system is determined not only by flux pinning but also by defects in the microstructure that control the connectivity of the superconducting particles. Some defects such as cracks, voids and large second phase particles act as permanent barriers to current flow, while others exhibit a weak coupling that is often field and temperature dependent. This spatial distribution of the superconducting paths available for current transfer produces percolative current flow. Clearly minimisation of the number and size of permanent obstacles to current flow improves current transfer and increases critical current density values in bulk HTS artefacts. With respect to the current carrying volume of polycrystalline HTSs, it is now well established that the type and/or properties of the boundaries between the superconducting particles control the macroscopic current transfer of all polycrystalline high-T_c superconductors. A number of analytical, but principally qualitative, models have been proposed to describe current transfer. The task is a challenging one, as direct evidence of the behaviour of current flow on a microscopic scale is inconclusive[19-21], and the suggested contributing factors are numerous and difficult to quantify. The first models to describe current transfer in superconductors employed the percolation theory of networks[22] and looked at the factors influencing the critical path within networks of various types of weak links; predominantly Josephson-coupled weak links. Alternative models of current transfer have been developed from descriptions of the specific

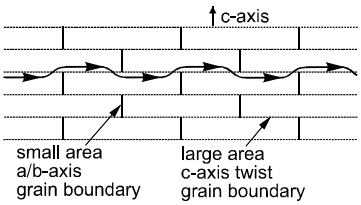

Figure 2.4
Schematic representation of the brick-wall model, showing meandering current flow via c-axis twist grain boundaries.

microstructure characterising the real material. These have focused on the microstructure of Bi-2223 and Bi-2212 silver-sheathed tapes. These tapes are fabricated by a process known as the powder-in-tube[23] (PIT) technique which produces a textured microstructure that is characterised by plate-like grains or colonies (see section 2.5) that are well aligned with the crystallographic c-axis of the grains preferentially oriented normal to the tape plane.

The first model of this type was the brick-wall model[24], which has a microstructure with a grain configuration that can be described as a stack of rectangular blocks (see figure 2.4). Current transfer between grains occurs exclusively at c-axis twist grain boundaries, which act as weakly coupled short Josephson junctions. Alternative descriptions based upon the brick-wall morphology have also been suggested[25]. Microstructural analysis and electrical transport measurements suggest that the current transfer mechanism described by the brick-wall model is not the dominant mechanism of current transfer in high temperature superconductors[26-28].

An extension of the brick-wall model is the railway-switch model[26]. This model suggests that current flow is restricted to the ab-planes, and frequent low-angle c-axis grain boundaries provide current paths in the ab-plane and indirectly in the c-axis direction (see figure 2.5) forming a complex 3D superconducting network. Numerous recent reports present a modified railway-switch model and suggest that low-angle ab-axis rather than low-angle c-axis grain boundaries are the predominant intergranular route of current transfer[20,28-30]. Limiting the number of grain boundaries, and therefore current limitation, by increasing the aspect ratio of the grains using improved texturing techniques is a suggested method of increasing the macroscopic critical current density common to both the brick-wall and railway-switch models.

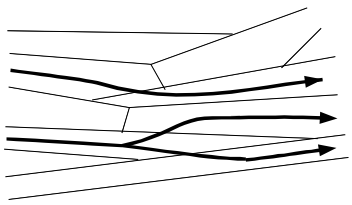

Figure 2.5
Schematic of the railway-switch microstructural model, showing current flow via low-angle c-axis grain boundaries.

A recent addition to these microstructural models is the freeway model[31]. This proposes that significant current transfer occurs through edge colony boundaries, facilitated by c-axis current redistribution. Due to the complexity implied in these predominantly qualitative descriptions, recent numerical analyses have returned to using percolation theory to describe limiting cases of the railway-switch

model[32,33]. Specific models are discussed in greater detail in chapter 7.

2.5 Anisotropy of HTS materials

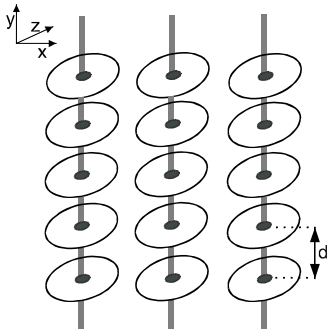

Figure 2.6
Schematic diagram of flux pancakes showing 2D coupled stacks.

Most high-T_c oxide superconductors consist of a highly anisotropic layered orthorhombic or tetragonal structure made up of CuO_2 planes, coincident with the ab-plane of the atomic structure, separated by planes of other oxides. The CuO_2 layers of this structure are, to various degrees, insulated from adjacent CuO_2 layers and it is believed that charge transport is mainly confined to the CuO_2 planes[34]. This layered structure gives rise to a very large resistive anisotropy above T_c of $\rho_c/\rho_{ab} \approx 10^4 - 10^5$ for Bi-2212[27] and $\rho_c/\rho_{ab} \approx 100$ for Y-123[35]. At temperatures below around 75 K for Y-123[36] and at practically all temperatures below T_c in the remaining high-T_c superconductors, the coherence length becomes smaller than the CuO_2 layer spacing, d, and the layered structure must be explicitly taken into account.

The Lawrence-Doniach model[37] treats the layered superconductor as a stack of Josephson-coupled superconducting layers. In the 2D limit, the flux line can be considered as composed of a stack of pancake vortices parallel to the c-axis, and Josephson vortices parallel to the ab-plane[38]. Instead of a cylinder of current circulating the individual flux lines perpendicular to the ab-plane, the layered structure separates the current cylinder into disks of current, pancake vortices, that circulate in the ab-plane of the superconducting layers coupled by lower current densities crossing between the adjacent layers (see figure 2.6). The Josephson junction currents between superconducting layers break the ellipticity, due to the anisotropic penetration depth, of the current streamlines of the Josephson vortex core (see figure 2.7). If the thermal energy of the pancake vortices becomes greater than the Josephson coupling between the superconducting layers the pancake vortices decouple and move within the superconducting layers independently of the vortices in other layers, transforming the 3D pancake lattice into a 2D planar vortex structure.

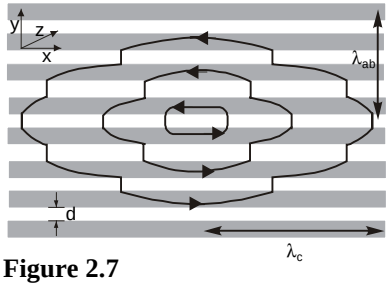

Figure 2.7
Schematic of the current distribution around a Josephson vortex in a layered superconductor. Grey layers are superconducting and insulating layer are white.

The high-T_c oxide superconductors exhibit strong critical current anisotropy. Fabrication techniques also impart anisotropy to J_c by producing an anisotropic distribution of pinning centres or highly textured grain structures. The behaviour of current transfer and therefore critical current anisotropy can be considered on both the microscopic and bulk polycrystalline macroscopic scales.

2.5.1 Anisotropy of HTS materials on the microscopic scale

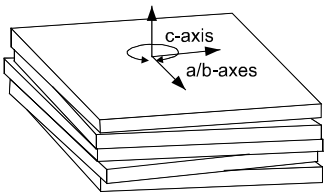

Figure 2.8
Schematic representation of a grain colony. Adjacent grains are separated by c-axis twist grain boundaries.

The microscopic scale involves current flow within individual grains or colonies of grains. A colony is a stack of grains with a common c-axis (see figure 2.8) and are thought to be a basic transfer element of current transport in many polycrystalline HTS materials. The anisotropy of the transport properties manifests itself in a strongly reduced critical current density along the crystallographic c-axis, $J_{c,c}$, in comparison to the critical current along the ab-planes, $J_{c,ab}$. The value of the critical current falls off more strongly for field applied perpendicular to the ab-plane than for fields parallel to the ab-plane. Typical values of the c-axis critical current for lead doped and undoped Bi-2212 single crystals are presented in table 2.1. In the superconducting state, dissipation for currents along the ab-planes and c-axis is thought to occur by two different mechanisms. The magnitude of the ab-plane intralayer current is determined by the motion of pancake vortices[39]; whereas current transfer along the c-axis seems to be limited by Josephson coupling between the adjacent layers[40]. The critical current densities $J_{c,c}$ and $J_{c,ab}$ have different temperature dependencies. Ginzburg-Landau theory predicts dependencies close to T_c of the form

$$J_{c,c} \propto (T_c - T)$$

and

$$J_{c,ab} \propto (T_c - T)^{3/2}.$$

The value of the critical current anisotropy on the microscopic scale, $J_{c,ab}/J_{c,c}$, is therefore temperature dependent and ranges in value.

The experimental determination of the Bi-2212 single crystal value of $J_{c,c}(T)$ at temperatures close to T_c suggests a number of possible dependencies[40,41], .such as $J_{c,ab} \propto (T_c - T)^{1/2}$ and $J_{c,c} \propto \tanh(1/T)$ consistent with c-axis Josephson coupling.

Recent results suggest that current flow is predominantly at the edges of Bi-2212 single crystals rather than in the bulk due to the presence of strong Bean-Livingston and/or geometric surface barriers[44,45]. However strong bulk pinning, relative to surface barrier strength, could dominate the effect on current flow, particularly at low temperatures. Uniform current flow is also found at elevated temperatures for which the HTS is in a highly dissipative state. It is also suggested that very weak bulk pinning could overcome the effects of surface pinning, placing a stringent limit on the regime in which surface barriers would dominate the behaviour of current flow[46].

Table 2.1 *Values of* $J_{c,c}$ *and* $J_{c,ab}/J_{c,c}$ *in lead doped and undoped single crystal Bi-2212.*

Reference	HTS	Temperature K	$J_{c,c}$ A·m^{-2}	Anisotropy $J_{c,ab}/J_{c,c}$
Kleiner[41]	$Bi_2Sr_2CaCu_2O_8$	4.2	1.5×10^6	-
Kleiner[41]	$(Bi_{1-x}, Pb_x)_2Sr_2CaCu_2O_8$	4.2	70×10^6	-
Latyshev[42]	$Bi_2Sr_2CaCu_2O_8$	0 (extrapolated)	1.0×10^6	-
Cho[43]	$Bi_2Sr_2CaCu_2O_8$	82	0.24×10^6	-
Cho[43]	$Bi_2Sr_2CaCu_2O_8$	84	0.0725×10^6	-
Cho[43]	$Bi_2Sr_2CaCu_2O_8$	0 (extrapolated)	2.0×10^6	-
Martin[40]	$Bi_2Sr_2CaCu_2O_8$	86	0.15×10^6	833
Martin[40]	$Bi_2Sr_2CaCu_2O_8$	87	0.05×10^6	1000

2.5.2 Anisotropy of HTS materials on the macroscopic scale

Current flow on the macroscopic scale of polycrystalline bulk samples exhibits different behaviour to current flow on the microscopic scale. Texturing techniques that induce a degree of alignment to individual grains within a sample result in an anisotropy of the macroscopic critical current. Measurements of the macroscopic anisotropy have been performed on silver-sheathed superconducting tapes, melt textured Y-123, and composite reaction textured Bi-2212. The studies using HTS tape and melt textured Y-123 have measured the critical current normal to the tape plane, J_c^{norm}, and parallel to the tape plane, J_c, and expressed the macroscopic critical current density as the ratio, J_c/J_c^{norm}. Values of J_c/J_c^{norm} are presented in table 2.2. A study of the critical current anisotropy of the composite reaction textured Bi-2212 is presented in section 3.4.3. In the

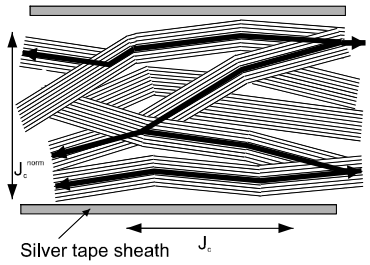

Figure 2.9
Schematic of the macroscopic (intercolony) current flow in Bi-2223 tapes, showing the zig-zag current path. The macroscopic critical current densities parallel , J_c, and normal, J_c^{norm}, to the tape plane are also indicated.

framework of the railway-switch model, the current path for J_c^{norm} consists of a zigzag route from one side of the tape core to the other (see figure 2.9) and as such represents a macroscopic average. Whereas the value of the macroscopic anisotropy does not bear an academic interest within microstructural models of current transport in polycrystalline materials, it is a realistic value to use in models of current transfer in bulk HTS devices.

Table 2.2 *Macroscopic anisotropy values for HTS polycrystalline materials.*

Reference	HTS	B, T	Critical current anisotropy, J_c / J_c^{norm}
Hensel[47]	$(Bi,Pb)_2Sr_2CaCu_2O_{10}$	B=0 T, T=77 K	≈ 10
Cho[29]	$Bi_2Sr_2CaCu_2O_8$	B=0.1 T, T=77 K	≈ 5
Chen[48]	$Bi_2Sr_2CaCu_2O_8$ (CRT)	B=0.1 T, T=77 K	≈ 30
Gao[49]	$YBa_2Cu_3O_x$	B=0 T, T=77 K	≈ 100

2.6 References

1 A. A. Abrikosov, Zh. Eksp. Teor. Fiz. **36,** 1442 (1957).

2 U. Essmann and H. Träuble, Phys. Lett. **A 24,** 526 (1967).

3 J. E. Evetts, *Concise Encyclopedia of Magnetic & Superconducting Materials*, 1st ed. (Pergamon Press Ltd, Oxford, 1992).

4 P. W. Anderson, Phys. Rev. B **9,** 309-311 (1962).

5 P. W. Anderson and Y. B. Kim, Reviews of Modern Physics **36,** 39-43 (1964).

6 E. Zeldov, N. M. Amer, G. Koren, A. Gupta, M. W. McElfresh, and R. J. Gambino, Applied Physics Letters **56,** 680-682 (1990).

7 M. P. A. Fisher, Physical Review Letters **62,** 1415-1418 (1989).

8 P. Berghuis, R. Herzog, R. E. Somekh, J. E. Evetts, R. A. Doyle, F. Baudenbacher, and A. M. Campbell, Physica C **256,** 13-32 (1996).

9 A. Gurevich and H. Kupfer, Physical Review B-Condensed Matter **48,** 6477-6487 (1993).

10 J. Gilchrist and C. J. Vanderbeek, Physica C **231,** 147-156 (1994).

11 T. Schuster, H. Kuhn, E. H. Brandt, M. V. Indenbom, M. Klaser, G. Mullervogt, H. U. Habermeier, H. Kronmuller, and A. Forkl, Physical Review B-Condensed Matter **52,** 10375-10389 (1995).

12 E. H. Brandt, Physical Review B-Condensed Matter **54,** 4246-4264 (1996).

13 T. Schuster, M. V. Indenbom, H. Kuhn, E. H. Brandt, and M. Konczykowski, Physical Review Letters **73,** 1424-1427 (1994).

14 C. P. Bean, Phys. Rev. Lett. **8,** 250 (1962).

15 C. P. Bean, Reviews of Modern Physics **36** (1964).

16 H. London, Phys. Lett. **36,** 162 (1963).

17 E. H. Brandt, Physical Review B-Condensed Matter **52,** 15442-15457 (1995).

18 L. Prigozhin, Ieee Transactions On Applied Superconductivity **7,** 3866-3873 (1997).

19 Y. Yan, J. E. Evetts, B. Soylu, and W. M. Stobbs, Physica C **261,** 56-64 (1996).

20 A. E. Pashitski, A. Polyanskii, A. Gurevich, J. A. Parrell, and D. C. Larbalestier, Physica C **246,** 133-144 (1995).

21 A. E. Pashitski, A. Gurevich, A. A. Polyanskii, D. C. Larbalestier, A. Goyal, E. D. Specht, D. M. Kroeger, J. A. DeLuca, and J. E. Tkaczyk, Science **275,** 367-369 (1997).

22 L. R. Ford and D. R. Fulkerson, *Flows in Networks* (Princeton Univ, 1962).

23 Z. Han, P. SkovHansen, and T. Freltoft, Superconductor Science & Technology **10,** 371-387 (1997).

24 L. N. Bulaevskii, J. R. Clem, L. I. Glazman, and A. P. Malozemoff, Physical Review B-Condensed Matter **45,** 2545-2548 (1992).

25 N. Adamopoulos and J. E. Evetts, Preprint, for ACS (1992).

26 B. Hensel, J. C. Grivel, A. Jeremie, A. Perin, A. Pollini, and R. Flukiger, Physica C **205,** 329-337 (1993).

27 M. P. Maley, J. H. Cho, J. Y. Coulter, J. O. Willis, L. N. Bulaevskii, L. R. Motowidlo, and P. Haldar, Ieee Transactions On Applied Superconductivity **5,** 1290-1293 (1995).

28 Y. H. Li, J. A. Kilner, M. Dhalle, A. D. Caplin, G. Grasso, and R. Flukiger, Superconductor Science & Technology **8,** 764-768 (1995).

29 J. H. Cho, M. P. Maley, J. O. Willis, J. Y. Coulter, L. N. Bulaevskii, P. Haldar, and L. R. Motowidlo, Applied Physics Letters **64,** 3030-3032 (1994).

30 L. Miu and S. Popa, Physica C **265,** 243-250 (1996).

31 G. M. Riley, A. P. Malozemoff, Q. Li, S. Fleshler, T. G. Holesinger, JOM-Journal of the the Minerals Metals & Materials Society **49,** 24 (5 pages) (1997).

32 E. G. Specht, A. Goyal, D. M. Kroeger, Physical Review B-Condensed Matter **53,** 3585-3589 (1996).

33 A. S. Goyal, E. D. Specht, D. K. Christen, D. M. Kroeger, A. Pashitski, A. Polyanskii, D. C. Larbalestier, JOM-Journal of the Minerals Metals & Materials Society **48,** 24-29 (1996).

34 A. W. Sleight, Science **242,** 1519-1527 (1988).

35 H. Safar, P. L. Gammel, D. A. Huse, S. N. Majumdar, L. F. Schneemeyer, D. J. Bishop, D. Lopez, G. Nieva, and F. Delacruz, Physical Review Letters **72,** 1272-1275 (1994).

36 J. R. Clem, Superconductor Science & Technology **11,** 909-914 (1998).

37 W. E. Lawrence and S. Doniach, in *Theory of layer structure superconductors*, Kyoto, Keigaku, Tokyo, 1970, p. 361-362.

38 J. R. Clem, Physical Review B-Condensed Matter **43,** 7837-7846 (1991).

39 T. T. M. Palstra, B. Batlogg, L. F. Schneemeyer, and J. V. Waszczak, Physical Review Letters **61,** 1662-1665 (1988).

40 S. Martin, A. T. Fiory, R. M. Fleming, G. P. Espinosa, and A. S. Cooper, Applied Physics Letters **54,** 72-74 (1989).

41 R. Kleiner and P. Muller, Physical Review B-Condensed Matter **49,** 1327-1341 (1994).

42 Y. I. Latyshev and A. F. Volkov, Physica C **182,** 47-51 (1991).

43 J. H. Cho, M. P. Maley, S. Fleshler, A. Lacerda, and L. N. Bulaevskii, Physical Review B-Condensed Matter **50,** 6493-6496 (1994).

44 D. T. Fuchs, E. Zeldov, M. Rappaport, T. Tamegai, S. Ooi, and H. Shtrikman, Nature **391,** 373-376 (1998).

45 S. F. W. Rycroft, R. A. Doyle, D. T. Fuchs, E. Zeldov, R. J. Drost, P. H. Kes, T. Tamegai, S. Ooi, and D. T. Foord, Submitted for publication in Physical Review B-Condensed Matter (1999).

46 A. Mazilu, H. Safar, D. Lopez, W. K. Kwok, G. W. Crabtree, P. Guptasarma, and D. G. Hinks, Physical Review B-Condensed Matter **58,** R8913-R8916 (1998).

47 B. Hensel, G. Grasso, and R. Flukiger, Physical Review B-Condensed Matter **51,** 15456-15473 (1995).

48 M. Chen, D. M. Glowacka, B. Soylu, D. R. Watson, J. K. S. Christiansen, R. P. Baranowski, B. A. Glowacki, and J. E. Evetts, Ieee Transactions On Applied Superconductivity **5,** 1467-1470 (1995).

49 L. Gao, R. L. Meng, Y. Y. Xue, P. H. Hor, and C. W. Chu, Applied Physics Letters **58,** 92-94 (1991).

CHAPTER 3

Bi-2212 CRT: Experimental characterisation and assessment

3.1 Introduction

One of the main tasks in the development of bulk HTSs for large-scale application is the further improvement of the critical current density value achievable in these materials. In order to fabricate large-scale artefacts the superconductor must be a polycrystalline material. As discussed in section 2.4 the polycrystalline microstructure of bulk superconducting samples limits current transfer in HTSs and textured microstructures favour high critical current values. A number of techniques have been employed to induce texture in HTSs including melt texture processing[1] and deformation processing of PIT tape[2]. The material studied in this thesis is Bi-2212 prepared by the composite reaction texturing (CRT) method[3,4], where a composite aligned MgO fibre/Bi-2212 preform, prepared by a polymer binding and processing route, undergoes partial melt processing. The MgO fibres provide nucleation sites and lattice matching of the fibres and the melt produces melt growth in the crystallographic ab and c directions, as dictated by the fibre orientation. The processing technique distributes fibres randomly in a planar manner relative to the flat surface of a sample, and can be cast with some preferred fibre alignment, resulting in a textured microstructure with the c-axis preferentially aligned perpendicular to the plane of the fibres.

The implementation of Bi-2212 in power system applications requires characterisation that accurately evaluates the benefits of fabrication procedures and the suitability of the electrodynamic properties for an intended application. To measure the basic characteristics of Bi-2212 CRT superconductors, an apparatus for the measurement of current transport characteristics has been constructed. The basic characteristics and measurement apparatus are the subjects of the first part of this chapter. Although the models developed in this thesis examine current transport in nonlinear media and are therefore applicable to superconducting systems in general, they principally, but not exclusively, model the

behaviour of the Bi-2212 CRT system. For this purpose, the range of parameters appropriate to macroscopic models has been experimentally examined.

The models presented assume the critical state of the superconductor has no magnetic field dependence. The validity of this assumption and the range of parameters used in the models is examined in more detailed measurements in the latter part of the chapter, with specific reference to the aspects of current transfer, anisotropy and the self-field effect.

3.2 Experimental apparatus for current transport measurements

Measurement of the magnetisation of a superconductor is a powerful technique for the study of critical currents. However, transport measurements are in some respects more appropriate. Transport measurements can show how a superconductor will behave in applied situations and are not subject to the same approximations used in the analysis of magnetisation measurements. Current transport measurements have been performed using a specially built apparatus (see figure 3.1). Current-voltage characteristics were measured using the four terminal method with the sample at 77 K in both self-field and applied field. The apparatus is composed of three control/measurement systems:

- Magnetic field control and measurement.
- Current-voltage control and measurement.
- Cryogen control.

Each system has interdependent functions and all are controlled from a single personal computer (see figure 3.2).

3.2.1 Control hardware and software

Data acquisition and control of the transport measurement apparatus is performed using a Viglen P133 personal computer. This uses an IOTECH general purpose interface board and corresponding visual basic driver for communication over an IEEE bus, which employs both standard Keithly IEEE device dependent communication protocols and the SCPI command language. Communication with the computer parallel port uses a dynamic link library supplied with ‘The Visual Basic Programing API’ book. The control and acquisition software is programed in the visual basic 3.0 programing language. The graphical user interface of the control and acquisition program is a standard windows environment and allows the user to set up a series of current-voltage measurements each

Figure 3.1
Picture of critical current measurement apparatus.

with different specifications; such as applied magnetic field, starting current and ramping current increment. Each measurement is plotted as a real time graph and is terminated when a user defined applied current or sample voltage criterion is reached. A datum point is measured every 0.3 s during a measurement of the EJ characteristic. All the settings for each of the instruments can be changed from the user interface and the acquired data can be saved onto disc after the measurement series. The program has extensive error prevention, safe guarding the user from entering incorrect values or values that are out of the instrumentation's range. In addition, the program has extensive capabilities for handling and trapping errors that occur in the program code or that arise from serial requests.

3.2.2 Magnetic field control and measurement

During the measurement of an EJ characteristic, a magnetic field can be applied to the sample. A Helmholtz split pair of solenoids produces the magnetic field, with iron pole pieces at their furthest separation, 115 mm. The maximum field produced is 0.43 T and is homogenous to ±1 mT within a volume 20 mm perpendicular to the pole piece axis. The accuracy of the applied field is 0.3 mT and was confirmed with a hand held probe over the 150 mT range. The magnet is powered by a 35 A, 60 V Hewlett Packard 6574A power supply operating in the constant current mode. The field direction can be changed by reversing the direction of the applied current and is accomplished using a Telemechanique contactor, which is switched from a mains supply controlled by the output of channel 0 of the computer parallel port, LPT2. The relay can only be switched at zero applied voltage. This prevents the emf of the magnet damaging the power supply if accidentally switched. The magnet cycles before a measurement series to ensure the magnet calibration is reproducible and not affected by magnetic hysteresis within the iron pole pieces. An offset current is applied to the electromagnet to ensure an initial applied field value of zero. The magnetic field strength is measured at each measurement datum point using a Seimens

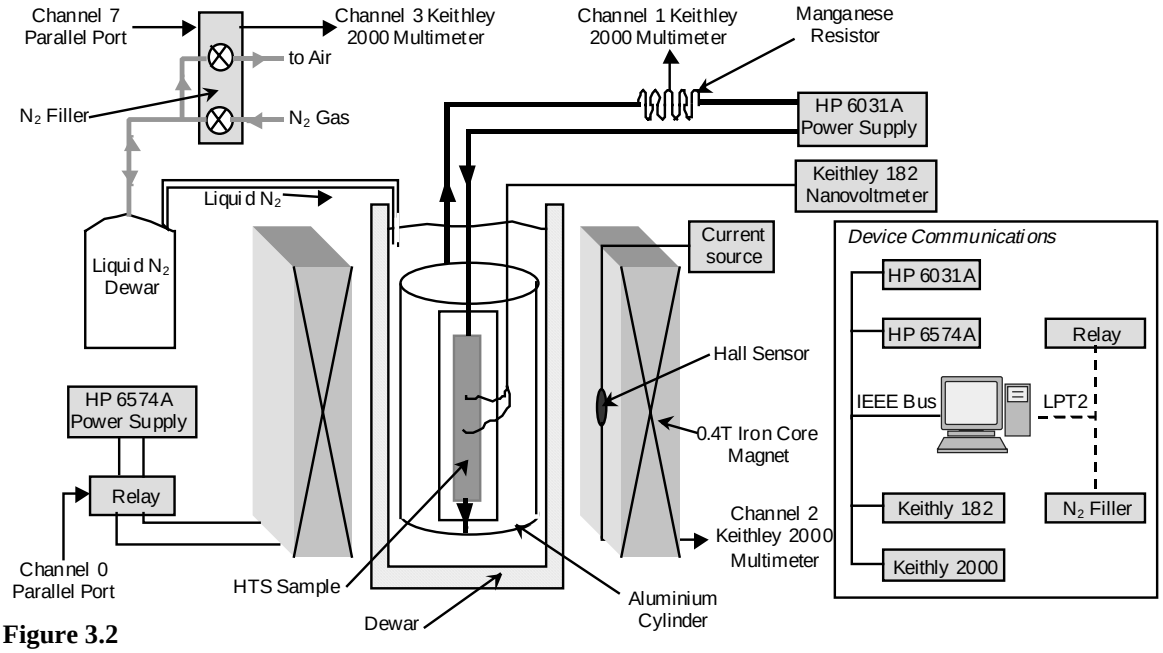

Figure 3.2
Schematic representation of apparatus for current transport measurements, inset shows instrumentation communication bus.

KSY10 Hall effect probe, mounted on a magnet pole piece. The Hall probe is supplied by a current source, stable to 0.01 %, which ensures a similarly stable field dependent Hall probe voltage response. This voltage is measured using a Keithly 2000 digital multimeter and scan card. The Hall effect probe has been calibrated with respect to Hall probe voltage using a Hirst GM04 gaussmeter. The calibrated field value is deduced from two 3rd order polynomials, covering two different field ranges. The computer magnet control uses a calibration of field against applied current to approach the user defined set field quickly and iterative measurement of the Hall probe voltage to attain the user defined set field.

The angle, which the plane of the sample surface makes with the applied field direction, can also be changed, to an accuracy of 0.01 degrees, by the rotation of a goniometer in which the sample mount rests. At high currents, the applied current return lead from the sample generates a magnetic field, which in measurements on Bi-2212 does not have a negligible effect on the sample. To eliminate this effect an aluminium cylinder, in which the sample is at the centre, acts as the applied current return path.

3.2.3 Current-voltage control and measurement

The applied sample current is supplied by a Hewlett Packard 6031A power supply in constant current mode and can supply a maximum current of 122 A accurate to 10 mA. The value of the sample current is monitored using the voltage across a 0.01 Ω manganese

resistor in series with the sample current circuit. The voltage across the sample is measured using a Keithley 182 nanovoltmeter.

Thermal emfs are the principal cause of noise in the voltage measurement. Noise is minimised by using low noise contacting techniques and minimising thermal gradients in the voltage leads. Because the noise changes slowly over time, using the nanovoltmeters pre-programed filters or changing the signal integration time is ineffective. In order to further reduce the effect of thermal emf noise several EJ characteristics are measured and averaged.

3.2.4 Cryogen control

Measurements are taken with the sample immersed in a liquid nitrogen reservoir. Liquid nitrogen must be periodically added to the reservoir to compensate for nitrogen gas boil off. This is performed by a specially designed nitrogen filler and controlled by the computer. An led sensor at a prescribed height in the reservoir monitors the liquid nitrogen level, when the level is low the reservoir is filled. The nitrogen filler controls the filling and the computer controls when this can be performed in order to avoid filling during a measurement. Two electronically controlled valves are used to fill the reservoir from a nitrogen dewar, one to fill the sample space and one to release dewar overpressure. Attempts were made to vary the sample temperature by using the lower partial pressure of liquid nitrogen in a pumped helium-nitrogen mix to vaporise liquid nitrogen, the enthalpy of which would cool the surrounding liquid nitrogen[5]; however, this proved unsuccessful.

3.3 Basic characteristics of Bi-2212 CRT current leads

Some of the basic properties of the Bi-2212 CRT material are examined in this section. These include grain connectivity, the temperature dependencies of the critical current and resistivity, and because of its importance in the specification of the models presented in this thesis, the nonlinearity of the EJ characteristic.

3.3.1 Transport current-voltage characteristics

The apparatus described above allows for more detailed, accurate and reliable d.c. transport measurements of the Bi-2212 CRT material than previously available. The self-field EJ characteristic of the material (see figure 3.3) is well described by a power law curve fit (see subplot of figure 3.3) and typically has an exponent of 6-8. The sample annealing and reaction process can further modify this range. The room temperature

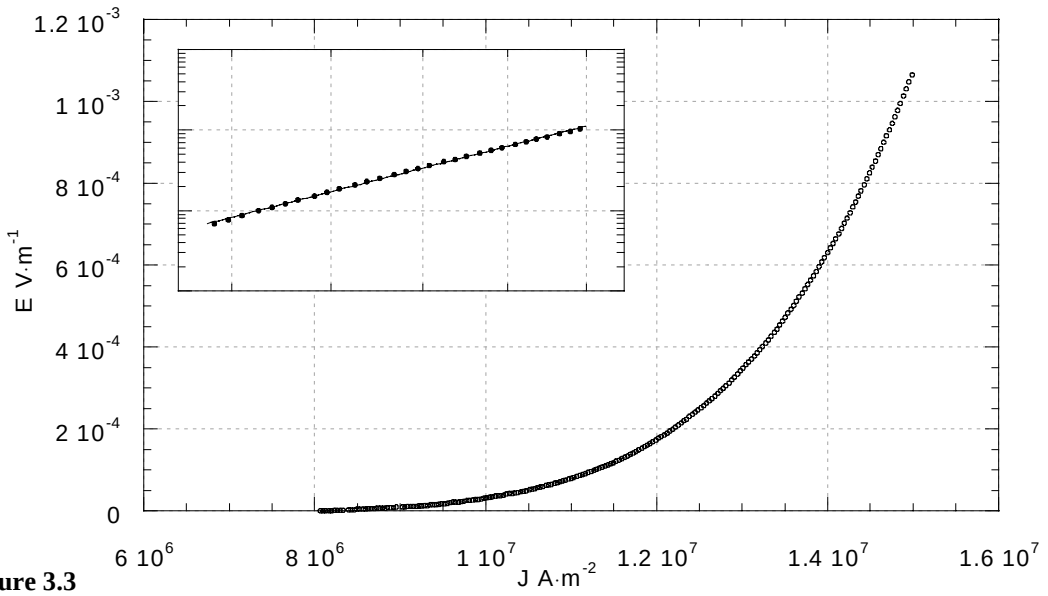

Figure 3.3
A plot of a typical EJ characteristic. The inset shows a log-linear plot of the EJ curve, and demonstrates power law behaviour. The EJ curve presented has an n -value of 8.

normal state resistivity of this material is 2×10^{-5} Ω·m. Transport measurements of the EJ characteristic of Bi-2212 CRT samples in magnetic field have been performed. All measurements are field cooled and as such could include magnetic field history effects. The hysteretic behaviour of the samples in applied field has been examined. Measurement of the transport J_c of the Bi-2212 CRT material at 77 K as a function of increasing (upward leg) and decreasing (downward leg) applied field over a 120 mT field range (see figure 3.4), the largest field applied of the transport measurements presented, does not show any hysteretic behaviour on the scale of 0.25 A; the current increment for all of the

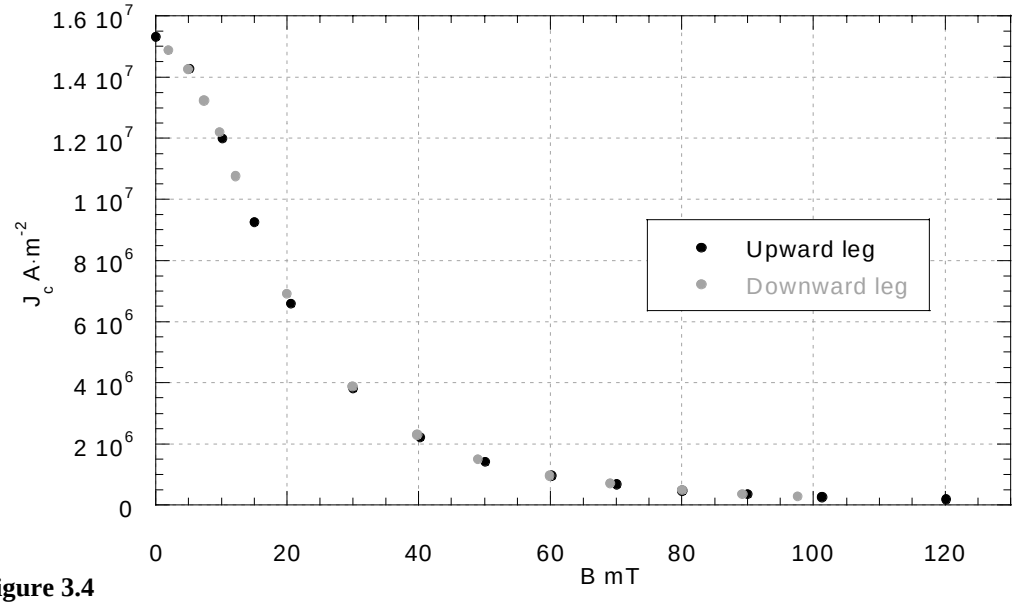

Figure 3.4
Plot of critical current *versus* applied magnetic field; closed black symbols indicate increasing field and closed grey symbols indicate decreasing field.

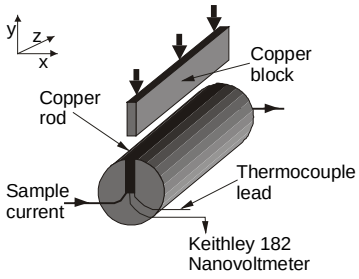

Figure 3.5
Schematic of apparatus used to measure T_c of bulk Bi-2212 current leads.

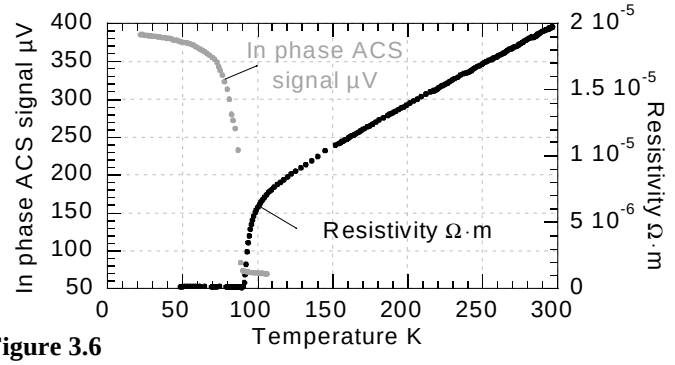

Figure 3.6
Plot of in phase voltage signal *versus* temperature (ACS measurement) and resistivity *versus* temperature (transport measurement), both indicate $T_c \approx 90$ K.

transport measurements presented in this chapter. Hysteretic behaviour is only likely to occur for inhomogeneous or granular superconductors which have very different values of J_c in the grains and the grain boundaries; this leads to flux motion between grains while flux within grains remains pinned[6]. The nonhysteretic behaviour of the Bi-2212 CRT material suggests the samples are homogeneous and possess good grain connectivity. This is corroborated in section 3.3.3 where the length scales over which current loops circulate in magnetised samples is discussed and found to be of the same scale as the sample dimension.

3.3.2 Measurement of the transition temperature in bulk Bi-2212 leads

As discussed in section 1.1 the transition temperature is an important characteristic of superconducting materials. It was decided to develop a non-destructive T_c measurement method for bulk Bi-2212 leads since existing apparatus could measure the T_c of only small samples. The sample was placed within a slot in a large copper block, with sample current leads, voltage sensing leads and a thermocouple attached (see figure 3.5); a copper block was then gently inserted into the slot on top of the sample. The entire arrangement was then cooled in liquid nitrogen, removed, and allowed to warm. On removal from the liquid nitrogen, a small sample current was applied and the voltage drop across the sample and temperature monitored. The T_c of post annealed Bi-2212 CRT material is about 90 K as can be seen from both the transport resistivity measurement and a.c. susceptibility (ACS) measurement of figure 3.6.

3.3.3 Magnetisation measurements

Calculations of the critical current density of the Bi-2212 CRT material from magnetisation measurements have been performed and are based upon the Bean model of

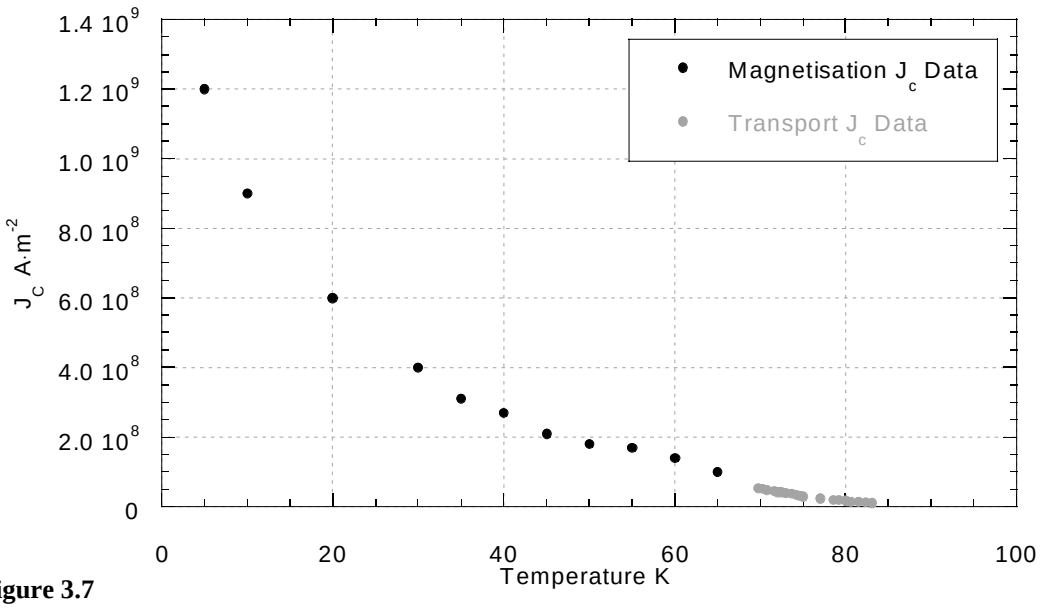

Figure 3.7
Plot of critical current density as a function of temperature, calculated from transport current and magnetisation measurements on Bi-2212 CRT material; transport measurements (grey closed circles) courtesy of M. Chen.

the critical state[7]. Measurements were taken using an Oxford Instruments vibrating sample magnetometer[8] with 12 T superconducting magnet and continuous flow cryostat with a temperature range of 4.2 K to 300 K. Magnetisation measurements of a sample with dimensions $l = 1.92 \times 10^{-3}$, $w = 1.94 \times 10^{-3}$, $t = 0.41 \times 10^{-3}$ m were used to calculate the magnetisation critical current data presented. The sample was assumed to approximate the geometry of a disc and the following formula[9] used to calculate J_c

$$J_c = \frac{3\Delta M}{2R} \tag{3.1}$$

where R is the radius of the disc ($\approx 1.93 \times 10^{-3}$ m), approximated as $(lw/\pi)^{1/2}$ and ΔM is the irreversible magnetisation of the sample as determined from the magnetic hysteresis cycle. The applied field was perpendicular to the broad face of the sample. This data was combined with transport critical current measurements, courtesy of M. Chen, to evaluate the temperature dependence of J_c in zero field[4] (see figure 3.7). A progressive increase in J_c with decreasing temperature is observed and is approximately linear with temperature in the range 69-82 K, reaching 5.5×10^7 A·m^{-2} at 69 K and tailing off at around 90 K in agreement with the transport and ACS measured value of T_c. The marked increase in J_c below 20 K leads to a value of 1×10^9 A·m^{-2} in zero field at 5 K and is in excess of 6×10^8 A·m^{-2} at 5 K and 12 T.

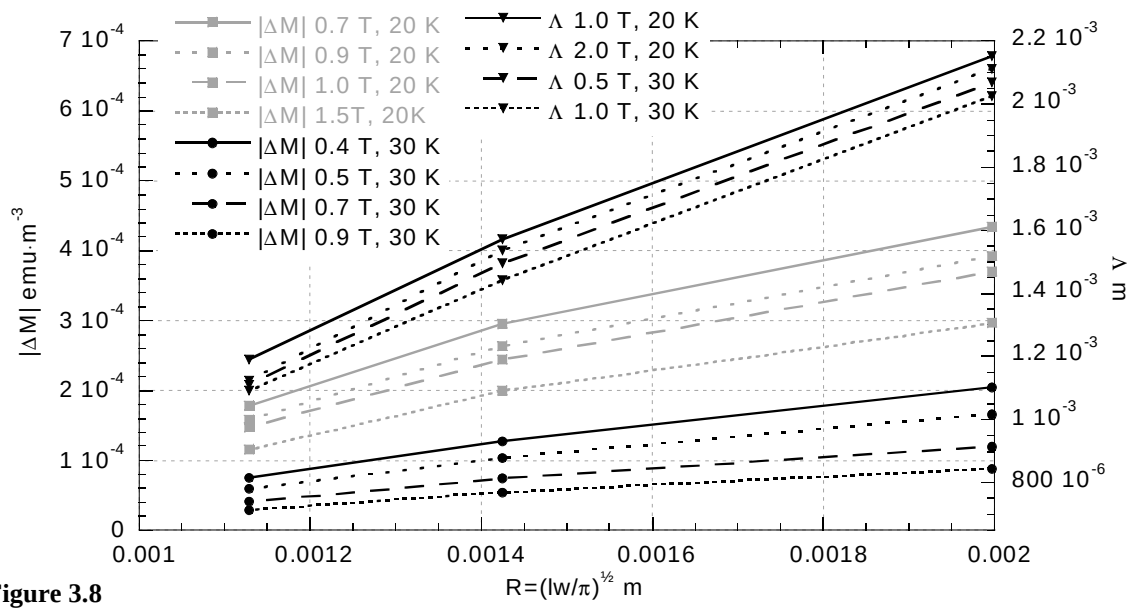

Figure 3.8

Plot of current length scale, Λ, and absolute magnetisation, $|\Delta M|$, *versus* the approximated radius of a sample which is progressively reduced in size. The plot presents data at several magnetic field and temperature values.

The J_c calculated from magnetisation data in polycrystalline HTS materials requires careful interpretation. Poor grain connectivity can hinder the magnetically induced current, preventing flow between neighbouring grains (intergranular current) and constraining flow to within the volume of single grains (intragranular current). Measuring the irreversible magnetisation for a sample with successively reduced dimension, R, allows one to clarify which type of current flow is dominant within a measured sample and investigate the grain connectivity. Equation (3.1) implies that if only intragranular currents flow the slope of a plot of ΔM against the sample dimension R should be zero; i.e. cleaving the sample does not effect the current path. Similarly, non-zero gradient implies dominant intergranular current flow. Measurements of the irreversible magnetisation of a successively reduced sample were taken at different temperatures and field values, and plotted against the sample dimension (see figure 3.8). Further analysis of the scale over which current loops circulate in magnetised samples was performed using the current scaling length analysis of Angadi *et al*[10]. This employs the slope of the reverse leg of a magnetic hysteresis loop measurement, as the field is reduced slowly from its maximum value, to determine the length scale, Λ, of the critical current path in the sample. The current scaling length for a thin uniform disc of superconducting material with radius R and thickness t in an applied field perpendicular to the radius is

$$\Lambda = \left(\frac{dm}{dH} \frac{\Theta}{\pi^2} \right)^{\frac{1}{3}} \tag{3.2}$$

where $\Theta = \ln\left(\frac{8R}{t}\right) - \frac{1}{2}$.

Again approximating a square slab geometry to that of a disc the dimension of the current scaling length has been calculated, for a sample at 20 K and 30 K at various field strengths (see figure 3.8), and found to be of approximately the same size as the sample. This indicates that current flow does not occur on a scale of the order of the grain size and that the current path occupies the entire volume of the sample; which implies good grain connectivity in that current flow is inhibited principally by the dimension of the sample and not by grain boundaries. Figure 3.8 shows that both analyses suggest that the current scaling length is of the order of the sample size and that grain connectivity in the Bi-2212 CRT material is good. This indicates that the combination of magnetisation and transport measurements in figure 3.7 is at least justifiable in terms of the current length scales involved.

3.4 Magnetic field and critical current anisotropy of Bi-2212 CRT

The magnetic field anisotropy has been investigated to characterise the Bi-2212 CRT material and assess its contribution to the self-field effect in anisotropic HTSs. The measurements have also been used to study the texture of this system. Finally, for the purposes of modelling macroscopic systems the value of the critical current anisotropy was examined.

3.4.1 Magnetic field anisotropy

The Bi-2212 system has one of the largest critical current anisotropies of the HTS systems. The magnetic field anisotropy of the critical current parallel to the tape plane was characterised with the magnetic field applied perpendicular, $B_{\perp}$, and parallel, $B_{\parallel}$, to the tape plane; the critical current was determined from the average of 20 EJ curves per field value. For $B_{\parallel}$ the reduction of J_c with increasing field can be divided into two regions, demarked by a change in slope occurring at 12 mT (see figure 3.9). The different behaviour of J_c with field direction confirms that the sample is anisotropic, and is an indication of a textured microstructure. The kink is absent in untextured Bi-2212 without

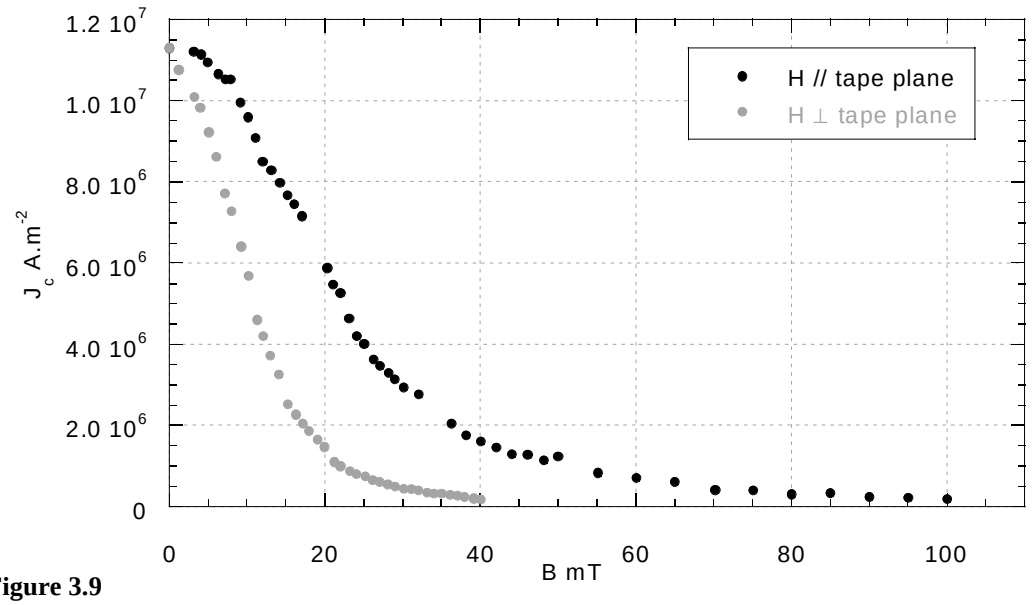

Figure 3.9
Plot of the critical current as a function magnetic field applied both parallel and perpendicular to the sample surface and perpendicular to the applied current direction.

MgO fibres and comparison with Bi-2212 single crystal $J_c(B)$ data[4,11] further suggests that grains within the sample are aligned.

3.4.2 Magnetic field anisotropy and texture

Single crystal and tape measurements[12] indicate that the magnetic field limitation of the critical current is primarily a function of the magnetic field component normal to the CuO_2 planes[13]; i.e. parallel to the c-axis. This suggests that in granular materials the misalignment of individual grains with respect to the tape plane is the principal cause of the magnetic field limitation of the critical current. Analysis has been performed to investigate granular misalignment in Bi-2212 CRT. Following the analysis of Hensel *et al*[14], using $J_c(B)$ data for applied field directions along a range of angles, $J_c(B,\theta)$, to the tape plane (see figure 3.10, plot a) the effective mean misalignment angle, ϕ_m, which determines the decay of J_c for field directions parallel to the tape plane, has been determined. The effective mean misalignment angle can be calculated by scaling $J_c(B,\theta)$ as $J_c(B\cos\theta)$ and using the expression

$$\cos(90^o - \phi_m) = B^*_{c\perp} / B$$

where $B^*_{c\perp}$ is the critical field component normal to the tape plane, defined by Hensel as the intersection of the plateau value with the master curve (see figure 3.10, plot b). Values are presented in table 3.1. Note $J_c(B)$ for B parallel to the c-axis is represented by the master curve and shows an exponential decay of J_c with field.

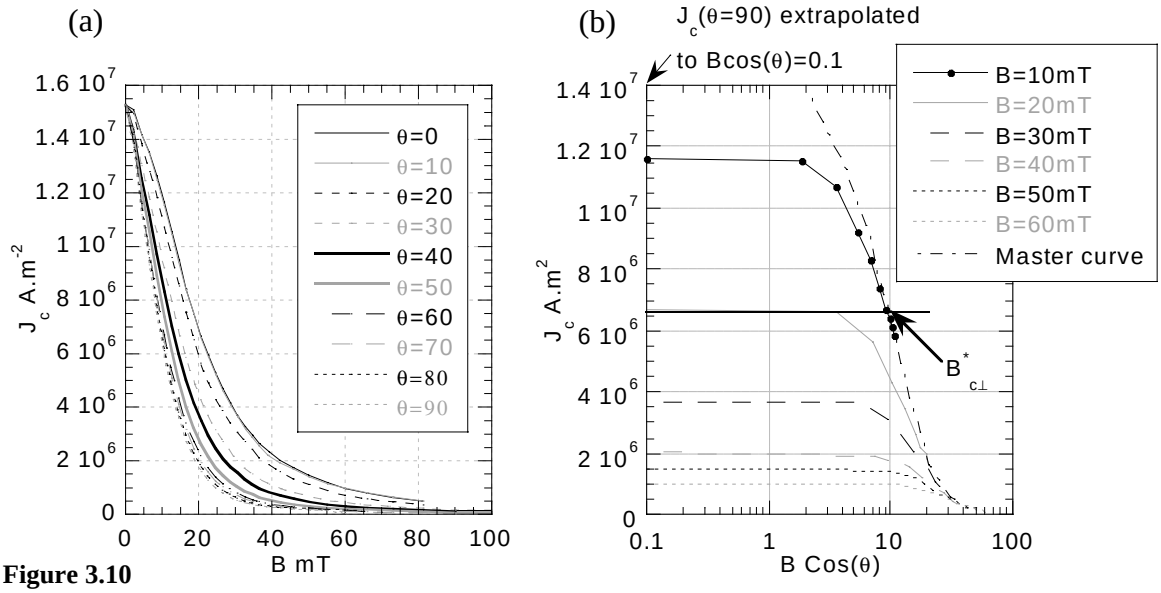

Figure 3.10
Plot (a), magnetic field dependence of the critical current density at 77 K for various field directions relative to the tape plane. Plot (b), data of plot (a) replotted as $J_c(\cos\theta)$, and $B^*_{c\perp}$ indicated.

The mean misalignment angle measured from the sample surface, S, or more accurately the mean texture plane, has also been calculated from $J_c(B)$ data for field directions parallel, $J_c\left(H_{\parallel S}\right)$, and perpendicular, $J_c\left(H_{\perp S}\right)$, to the sample surface, employing the relation[15]

$$J_c\left(H_{\parallel S}\right) = J_c\left(H_{\perp S}\tan\phi_m\right).$$

For the samples measured the values for the two methods agree within their standard deviations (see table 3.1). A range of misalignment angles is found with values which predominantly indicate poor texture. The 10° misalignment angle calculated for sample 246 is in approximate agreement with pole figure analysis which reveals that over 70% of the Bi-2212 grains are aligned to within 15° of the normal to the texture plane in this sample.

Table 3.1 *Study of misalignment angle in Bi-2212 CRT, sample 246 results courtesy of M. Chen.*

Sample name	ϕ_m (Hensel)	ϕ_m (Miu)
246		10°
an05		22°
rb3a	Mean=26°±2° (std)	25°
an02	Mean=25°±2° (std)	27°

3.4.3 Critical current anisotropy

The flexibility of the CRT process allows for the production of large section textured samples. This enables the application of voltage taps across the thickness of a sample and

thereby the measurement of the critical current normal to the tape plane, J_c^{norm}. The self-field critical current density value normal to the tape plane of a thick textured sample is 2.4×10^6 A·m^{-2} which gives a critical current anisotropy ratio, J_c / J_c^{norm}, of 5. An anisotropy value of 3 was obtained on a similar sample by A. Kursumovic. In contrast a value of 30 was obtained by M. Chen[4] prior to this work. Whereas this comparatively high value could be attributed to a reduction of the J_c of recently measured samples, both the values of J_c and J_c^{norm} have decreased and increased respectively compared to the values of reference 4. A range of anisotropy ratios and by implication varying degrees of texture has been found in the samples measured. This is thought to be a consequence of the sensitivity to processing conditions and MgO fibre quality of the Bi-2212 CRT material. Development problems encountered in the large-scale production of MgO fibres, in preparation for, and during the technology transfer of the Bi-2212 CRT HTS system, along with changes in sample processing personnel has meant that throughout the experimental period of this work the texture quality of the samples available has been poorer. This has in turn lead to smaller critical current density values and less significant magnetic field anisotropy. Recent refinement of the processing techniques has produced samples with J_c values of over 30×10^6 A·m^{-2}, which surpass the J_c values obtained at the beginning of the CRT project.

To investigate the effect on anisotropy in the macroscopic systems modelled, a range of values has been used in order to reflect the range found in the real Bi-2212 CRT system. The range employed is consistent with values obtained by experiment and values in the literature (see section 2.5.2) and is limited only by the convergence criteria of the solution. The appropriate description of anisotropy in both microscopic and macroscopic modelled systems is not trivial and is discussed at greater length in section 4.3.

3.5 The self-field in HTS

The models of current flow described in this thesis assume that the superconductor has no critical state field dependence. In this section, a study of the magnitude of the self-field effect on the transport properties of the Bi-2212 system and aspects of the critical state dependence on the magnetic field are presented.

3.5.1 Transport properties and the self-field

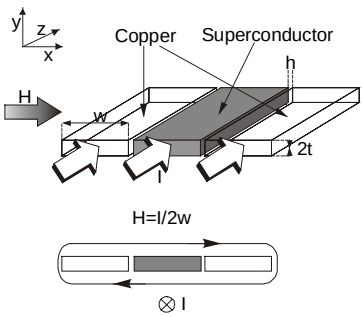

Figure 3.11
Schematic arrangement of the superconductor and the copper conductors for the reduction of the perpendicular component of the self-field. All three conductors carry the same current and have the same dimensions: *w*=6.48mm, 2*t*=0.95mm, *h*=0.2mm.

The transport current through a conductive media possessing slab geometry with width several times its thickness produces a self-field at the edges, with a strong component perpendicular to the sample surface[16,17]. For a thin sample of thickness $2t$ carrying a current density J, the field is purely perpendicular at the edges and approximately of magnitude Jt. In a textured material, with ab-planes parallel to the slab surface this component is perpendicular to the ab-planes. The critical current density along the ab-planes, $J_{c,ab}$, and the irreversibility field, H_{irr}, for anisotropic superconductors is much lower when the magnetic field is perpendicular, $H \perp ab$, to the ab-planes than when the magnetic field is parallel, $H \| ab$, to the ab-planes[18,19]. In such a case, the critical current density is $J_{c,ab}\left(H_{\|ab}\right)$ at the centre of the sample and approaches the smaller value $J_{c,ab}\left(H_{\perp ab}\right)$ towards the edges of the sample resulting in a critical current distribution across the sample cross section. This underestimates the self-field unaffected value of the transport critical current density as measured values are of the macroscopic average critical current density J_c^m, $J_c^m = I_{app} / A$ (see section 2.2.3). Attempts have been made to reduce the

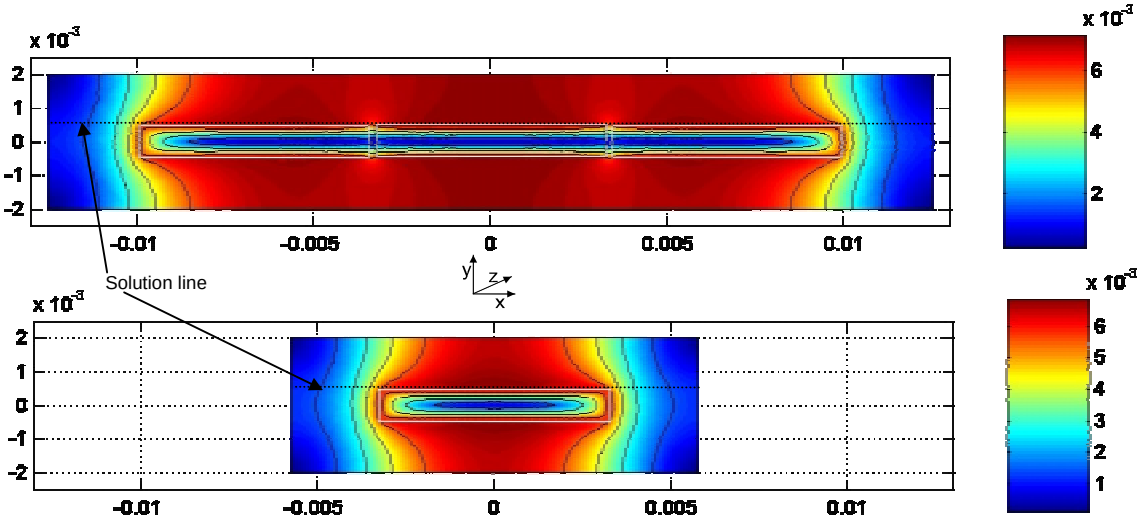

Figure 3.12
Contour plots of magnetic flux density distribution in the vicinity of the three and single conductor configurations, white rectangles delineate conductor cross sections. Each conductor has an applied current which is equal to the I_c of the superconducting device, which is 75A. Dimensions are in metres and the colour index refers to units of magnetic flux density in Tesla.

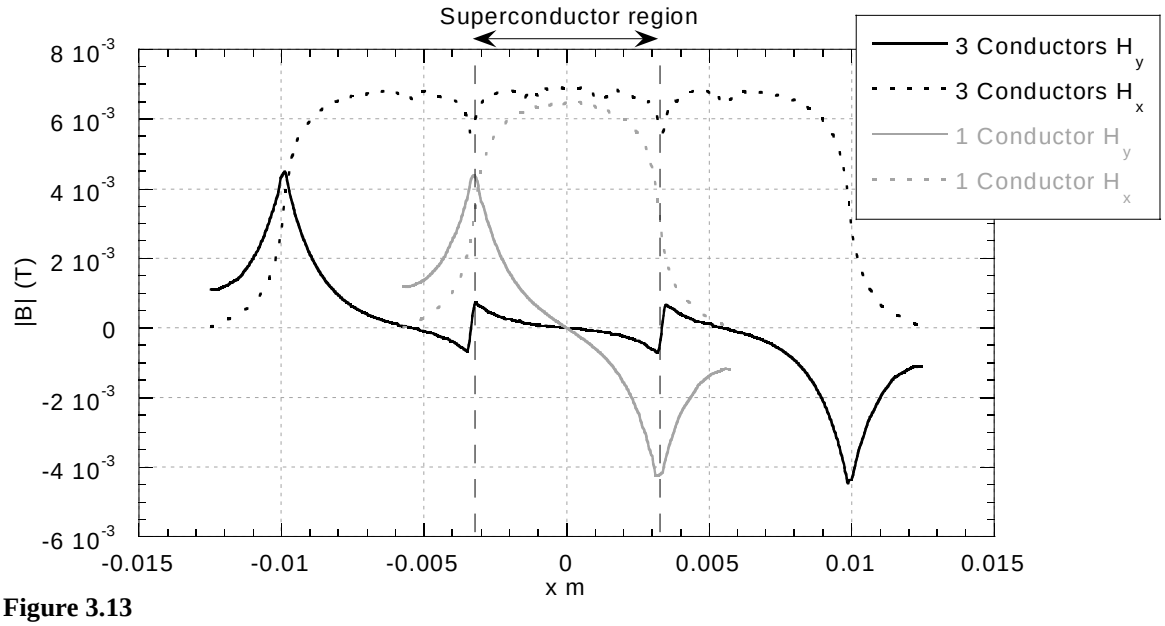

Figure 3.13
Plot of the *x* and *y* components of the magnetic flux density above the current carrying single and three-conductor configurations, see indicated solution line in figure 3.12, as computed by finite element analysis.

self-field effect by aligning two superconductors side by side[20]. In the method presented here two copper conductors with the same cross section as the superconductor are placed on either side of the sample, as shown in figure 3.11, and equivalent currents passed down all three conductors. The magnetic fields of the individual conductors superpose producing, approximately, a field that is homogenous and parallel over the superconductor surface. A computer simulation of the magnetic field of a single conductor and of the three-conductor configuration using a finite element model has been performed. The dimensions used for the model were exactly as stated in figure 3.11. The model assumes all the conductors carry a uniform applied current density equal in magnitude to the critical current density of the superconductor. The specification of a uniform current density distribution is not a limitation of the finite element analysis. Whereas a multiple parameter fit to a generalised critical state model may have given some indication of the form of the current density profile of the sample, direct comparison between a single conductor, which has complicated perpendicular components modifying the field profile within the conductor and the three-conductor model would then not be possible. Figure 3.12 shows a contour plot of the magnetic field density of the different configurations. Plots of the magnitude of the *x* and *y* components of the magnetic flux density along the width of the geometries, calculated just above the upper surface of the conductors (see figure 3.13), indicate that at self-field the maximum perpendicular component of magnetic

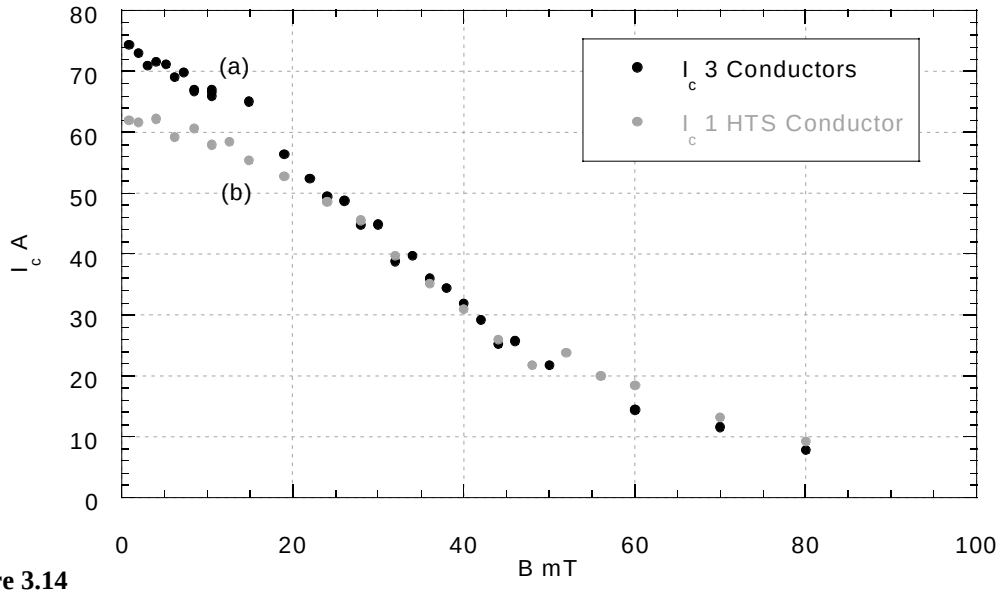

Figure 3.14
Critical current as a function of applied magnetic field applied both parallel to the sample surface and perpendicular to the applied current direction. Curve (a) three-conductor configuration, curve (b) single conductor.

field near the edge of the sample is reduced by a factor of 6; this is of particular significance for anisotropic samples.

The three-conductor geometry allows the critical current density to be measured as a function of field strictly along the ab-planes, by applying a magnetic field along the ab-planes and perpendicular to the current direction. The critical current density as a function of magnetic field is shown in figure 3.14 for two cases: (a) for all three conductors carrying the same current and (b) where only the superconducting sample carries current. In the first case, the critical current at zero applied field, is higher than the second by more than 20 %. At high magnetic fields the two curves are almost indistinguishable and decrease slowly with increasing field.

3.5.2 The critical state field dependence and the self-field

The Bean treatment of the critical state involves a critical current density which is independent of the local magnetic field (see section 2.3) and is constant inside the superconductor. In a slab geometry the internal field varies linearly with position. However, the critical state is often more realistically described by a field dependent critical current density $J_c(B)$ for which the field profile varies with position in a way determined by Maxwell's equation $\nabla \times H = J$; with $J = J_c(B)$ determined by the pinning mechanism and summation model applicable for the particular material[21]. The critical current field dependence is often deduced by performing magnetisation measurements or

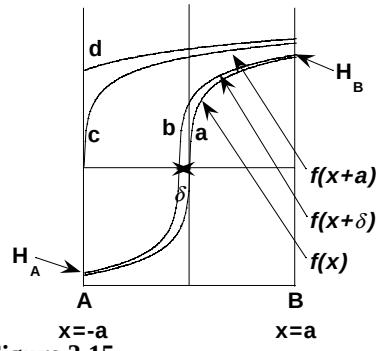

Figure 3.15

A hypothetical field profile, $f(x)$, inside a superconducting slab of width 2a at zero applied field and its evolution under an applied magnetic field parallel to the surface of the sample and perpendicular to the current. The field is shown (a) for the self-field situation, (b) for a small increment of the magnetic field from zero, (c) at a characteristic value H^* and (d) at larger fields.

measurements of a.c. field penetration in superconducting cylinders. Fitting routines are used to distinguish between different critical state models; some involving three unknown parameters[22]. In collaboration with N. Adamopoulos a method that enables the deduction of part of the magnetic field profile directly from transport measurements has been developed[23] which can be applied to any class of HTS material.

For a slab geometry the self-field peaks at the edges of the sample, where it turns around the cross section (see figure 3.13). In the case of an anisotropic high-T_c material textured with the ab-planes parallel to the slab surface, the y-component of the self-field reduces the local value of the critical current density. Other groups have studied this self-field effect by measuring the value of the critical current as a function of sample thickness as the material is progressively thinned[11,24]. Although this demonstrates that the self-field does affect the transport critical current, it is not quantitative, since samples with different thicknesses correspond to different spatial variations of the self-field and therefore y-axis field component. In the three-conductor configuration, the self-field is uniform across the sample width both in direction and magnitude and the field profile inside the material is independent of sample size and determined only by the field dependence of $J_{c,ab}\left(H_{\|ab}\right)$.

A schematic profile is shown in figure 3.15, which qualitatively shows the main properties of the critical state. The current density dH_x/dy is maximum at the centre ($H_x = 0$) and minimum at the surface ($H_x = H_{sf}\left(x = a\right)$). Curve (a) corresponds to the self-field situation, while curves (b), (c) and (d) correspond to different values of the applied field directed parallel to the sample surface. Curve (b) represents the magnetic flux profile for a small increment of the applied magnetic field from zero, for which the profile is displaced along the x-axis. At some characteristic value H^* of the applied field, the field at one surface of the sample becomes zero, curve (c). Since the field gradient is high at the surface, the flux profile is sensitive, locally, to small changes of the magnetic field. At larger fields, the field profile has the shape shown by curve (d). Assuming that the

magnetic field at one surface is $H_A = H(x=-a)$ and $H_B = H(x=a)$ at the other when the magnetic field, H_{app}, is applied, the measured critical current is

$$I_c = |H_B w - H_A w| = w|H_A - H_B| = w\Delta H \tag{3.3}$$

or $$\frac{I_c}{w} = \Delta H$$

with $\Delta H = H_B - H_A$. Correspondingly, the applied field is given by

$$H_{app} = \frac{(H_B + H_A)}{2}. \tag{3.4}$$

For the Bean critical state ΔH, and therefore I_c, remains constant. However, this is not the case for field dependent critical states where ΔH and I_c progressively decrease. When H_{app} reaches some critical value H^*, the magnetic field H_A becomes zero and $H_{app} = \Delta H / 2$. At this point the variation of I_c with H_{app} will show a point of inflection, as any small change of the applied field will affect H_A much more than H_B, due to the high gradient of the flux profile at A. At higher applied fields, the magnetic fields H_A and H_B approach each other, corresponding to a gradual reduction of the critical current with increasing field.

The field distribution inside the sample at self-field possesses some characteristic properties. The field distribution, described by the function $f(x)$ in figure 3.15, once determined, describes the properties of the magnetic flux distribution, and measured critical current, at all levels of the applied field. If J_A and J_B are the current densities at the two surfaces ($J_A = df(x+\delta)/dx|_{x=-a}$ and $J_B = df(x+\delta)/dx|_{x=a}$), from equations (3.3) and (3.4) we have

$$\left|\frac{d(\Delta H)}{dH_{app}}\right| = 2\frac{J_A - J_B}{J_A + J_B}. \tag{3.5}$$

This can also be written as

$$\frac{J_B}{J_A} = \frac{4}{\left|\frac{d(\Delta H)}{dH_{app}}\right| + 2} - 1 = R(H_{app}).$$

Equation (3.5) shows that the quantity $d(\Delta H)/dH_{app}$ attains a maximum value of 2 at $H_{app} = H^*$, in the extremum case when the critical current density J_B approaches zero. At

the point of inflection, where $H_{app} = H^*$ and $\Delta H = 2H^*$, the magnetic field at point B, H_B, will be $2H^*$ and that at point A, H_A, will be 0. Therefore, equation (3.5) becomes

$$J\left(2H^*\right) = R\left(H^*\right)J(0) \tag{3.6}$$

where $R\left(H_{app}\right)$, which is a measured quantity, gives the ratio between J_A and J_B at any instant. Using a series of expansions applied to an arbitrary field profile (see Appendix A) one can find the expression for the ratio of the two defined current densities at A and B, $J(0)$ and $J\left(\Delta H_{sf}/2\right)$ where ΔH_{sf} is the value of ΔH at zero applied field

$$J(0) = J\left(\frac{\Delta H_{sf}}{2}\right)\left(1 - \frac{1}{2}\left|\frac{d(\Delta H)}{dH_{app}}\right\|_{H_{app}=H^*}\right). \tag{3.7}$$

Given the field dependence of the critical current for an applied magnetic field aligned strictly parallel to the ab-planes of a measured sample, equations (3.6) and (3.7) give the field dependence of the self-field unaffected critical current density at the two different field values, $2H^*$ and $\Delta H_{sf}/2$ (normalised with respect to the value at zero magnetic field).

The above analysis assumes perfect cancellation of y-axis components of the self-field at the edges of the superconductor, whereas figure 3.13 shows the magnitude of these components is only reduced. Further, no sample is perfectly textured, and there are always inhomogeneities such as porosity and cracks. In the application of this analysis to real materials these approximations must always be considered. However, for an ideal sample, the above treatment has shown that properties and features of the field profile can be deduced without the use of any fitting routines.

It was believed that the entire field profile could be deduced by just considering the flux profile to be a single function that moves within the bounds of a sample under the influence of an applied field. However such a solution is not analytically soluble and requires fitting routines thereby providing no improvement upon existing methods. If fitting routines are used, the three-conductor configuration allows the field profile to be measured independent of sample size as a function of field strictly along the ab-planes; i.e. subject to the combined field of the applied field and self-field directed parallel to the ab-planes. This allows the horizontal axis of figure 3.14 to be more readily corrected. The magnetic field x-component plotted in figure 3.13 indicates that an offset of 7 mT for the zero field datum point would be reasonable.

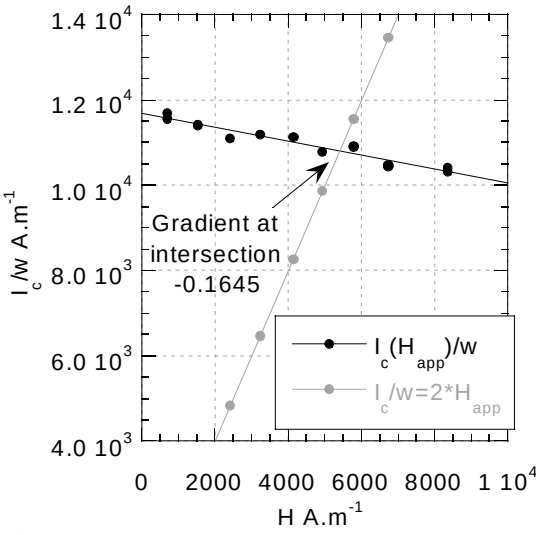

Figure 3.16
Plot of I_c/w *versus* applied magnetic field strength, indicating the intersection of the experimental line $I_c(H_{app})/w$ with the line $I_c/w = 2H_{app}$.

The above analysis of the critical current as a function of the applied field requires that the point of inflection and the first derivative at this point, as well as at subsequent points, can be deduced from the experimental results. A simple way to find the point of inflection is to note that when the applied field reaches H^*, $H_A = 0$ and so $\Delta H = 2H^*$. Therefore, the point of inflection occurs at the field value coinciding with the intersection of the line $I_c/w = 2H_{app}$ with the experimental line $I_c(H_{app})/w$ (see figure 3.16). For the data presented the field value is 6.8 mT. Also the field value corresponding to $\Delta H_{sf}/2$ as employed in equation (3.8) is 7.4 mT. The gradient of the experimental line, $I_c(H_{app})/w$, and the normalised critical current values at these fields are shown in table 3.2.

These normalised values of the self-field unaffected critical current density, suggest a relatively weak magnetic field dependence of the critical current density in the Bi-2212 CRT material. This indicates that the omission of a self-field critical current field dependence in the computer models developed in this thesis is reasonable for this material. Given that there is a 20 % reduction in the critical current density measured for the single conductor in self-field, this weak self-field dependence suggests that the perpendicular component of the self-field gives rise to the underestimate of the measured value of the critical current density as given by curve (a) of figure 3.14. This further suggests, that this Bi-2212 CRT sample is anisotropic which indicates that this sample of the material is well textured, an assumption of this analysis, and that it is this anisotropy that is the principal

Table 3.2 *Critical current normalised with respect to* $J(0)$.

Field at which critical current density calculated	Field value mT	Absolute value of the gradient of $I_c(H_{app})/w$ at field value	Equations used	Self-field unaffected critical current density at field, normalised with respect to $J(0)$
H^*	6.3	0.1645	(3.6)&(3.7)	0.85
$\Delta H_{sf}/2$	7.4	0.1521	(3.8)	0.92

cause of the materials self-field critical current limitation. In contrast the critical current density of sample an02 measured using the three-conductor arrangement is 8 % larger than that measured using a single conductor arrangement and has a relatively large calculated misalignment angle (see section 3.4.2) which suggests it is poorly textured.

The above treatment has implications for a wide class of materials and measurement configurations. The self-field effect is expected to be enhanced in samples with thickness comparable to their width, in which the field non-uniformity extends deep inside the material and away from the edges. In thin films, the edges are subjected to a stronger field than the middle part, and the strong perpendicular component will severely affect the depinning of vortices[25]. These issues have to be addressed for a meaningful comparison of results taken from different samples and under different conditions.

3.6 Summary

An apparatus for current transport measurements and, briefly, the processing methods of the Bi-2212 CRT material have been described. The basic characteristics of the Bi-2212 CRT material have been determined such as T_c, the temperature dependence of J_c in zero field and the current scaling length. The range and value of suitable input parameters for models of the macroscopic behaviour of this material have been studied. It has been shown that the EJ characteristic of the Bi-2212 CRT material can be described well by a power law and has n-values typically in the range 6-8. The critical current anisotropy, J_c / J_c^{norm}, in this material covers a range from near isotropic to possibly as high as 30.

Properties of the self-field of the Bi-2212 CRT material have been studied using a method to measure the critical current density as a function of field strictly along the ab-planes of a HTS sample, which is only nominally affected by perpendicular magnetic field components. Further, a mathematical analysis has been developed that enables the deduction of part of the magnetic field profile directly from transport measurements which can be applied to any class of HTS material. Employing this analysis it has been found that the Bi-2212 CRT material has a weak critical current field dependence and that the magnetic field anisotropy is the principal cause of this materials self-field critical current limitation. Finally, given that the 2D models used throughout this work assume magnetic field z-component derivatives tend to zero, it is reasonable to ignore the self-field effect when modelling this class of materials.

3.7 References

1 M. Murakami, N. Sakai, T. Higuchi, and S. I. Yoo, Superconductor Science & Technology **9,** 1015-1032 (1996).

2 R. Zhou, W. L. Hults, R. J. Sebring, J. F. Bingert, J. Y. Coulter, J. O. Willis, and J. L. Smith, Physica C **255,** 275-280 (1995).

3 B. Soylu, N. Adamopoulos, D. M. Glowacka, and J. E. Evetts, Applied Physics Letters **60,** 3183-3185 (1992).

4 M. Chen, D. M. Glowacka, B. Soylu, D. R. Watson, J. K. S. Christiansen, R. P. Baranowski, B. A. Glowacki, and J. E. Evetts, Ieee Transactions On Applied Superconductivity **5,** 1467-1470 (1995).

5 J. Z. Xu, H. J. Jansch, and J. T. Yates, Journal Of Vacuum Science & Technology a-Vacuum Surfaces and Films **11,** 726-727 (1993).

6 J. E. Evetts and B. A. Glowacki, Cryogenics **28,** 641-649 (1988).

7 C. P. Bean, Reviews of Modern Physics **36** (1964).

8 S. Foner, The Review of Scientific Instruments **30,** 548-557 (1959).

9 J. E. Evetts, *Concise Encyclopedia of Magnetic & Superconducting Materials*, 1st ed. (Pergamon Press Ltd, Oxford, 1992).

10 M. A. Angadi, A. D. Caplin, J. R. Laverty, and Z. X. Shen, Physica C **177,** 479-486 (1991).

11 N. Nakamura, G. D. Gu, and N. Koshizuka, Physica C **225,** 65-70 (1994).

12 L. N. Bulaevskii, L. L. Daemen, M. P. Maley, and J. Y. Coulter, Physical Review B-Condensed Matter **48,** 13798-13816 (1993).

13 P. H. Kes, J. Aarts, V. M. Vinokur, and C. J. Vanderbeek, Physical Review Letters **64,** 1063-1066 (1990).

14 B. Hensel, J. C. Grivel, A. Jeremie, A. Perin, A. Pollini, and R. Flukiger, Physica C **205,** 329-337 (1993).

15 L. Miu, Physical Review B-Condensed Matter **45,** 8142-8145 (1992).

16 E. H. Brandt and M. Indenbom, Physical Review B-Condensed Matter **48,** 12893-12906 (1993).

17 A. Forkl and H. Kronmuller, Physica C **228,** 1-14 (1994).

18 T. Nishizaki, F. Ichikawa, T. Fukami, T. Aomine, T. Terashima, and Y. Bando, Physica C **204,** 305-314 (1993).

19 F. M. Sauerzopf, H. P. Wiesinger, W. Kritscha, H. W. Weber, M. C. Frischherz, and H. Gerstenberg, Cryogenics **33,** 8-13 (1993).

20 B. Tenhaken, L. J. M. Vandeklundert, V. S. Vysotsky, and V. R. Karasik, Ieee Transactions On Magnetics **28,** 755-758 (1992).

21 A. M. Campbell and J. E. Evetts, Adv. Phys. **21,** 199 (1972).

22 P. Fournier and M. Aubin, Physical Review B-Condensed Matter **49,** 15976-15983 (1994).

23 N. Adamopoulos and S. K. Patapis, Physical-Review B **57,** 5055-5058 (1998).

24 H. Kliem, A. Weyers, and J. Lutzner, Journal Of Applied Physics **69,** 1534-1537 (1991).

25 E. P. Babic, M. Prester, D. Drobac, Z. Marohnic, P. Nozar, P. Stastny, F. C. Matacotta, S. Bernik, Physical-Review B-Condensed Matter **45,** 913-920 (1992).

CHAPTER 4

A model of current transport in nonlinear media

4.1 Introduction

The mathematical representation of current flow in conductive media can be described by either a partial differential equation (PDE) or an integral equation. Only in the very simplest of cases is it possible to find exact analytical solutions to these equations, and in general one has to rely on numerical techniques to find approximate solutions. The finite element (FE) method is a general technique for numerical solution of differential and integral equations and is the main, but not exclusive, method employed for solving current transfer problems in this thesis. The method was introduced by engineers in the late 1950's and early 1960's for the numerical solution of PDEs in structural engineering. When the mathematical study of the FE method started in the mid 1960's it soon became clear that it is a general technique for the numerical solution of PDEs and integral equations.

This chapter describes the FE method employed in the current flow models presented in this thesis. The principal approaches used in the numerical solution of PDEs and the electromagnetic formulation used to express mathematically the physical model of current flow as a PDE are discussed. An overview of the FE representation of the PDE describing the physical system is presented and examined in detail. Finally, the numerical solution of the FE equation system and other computational aspects are considered.

4.2 Alternative modelling approaches

The approach used to solve numerically PDEs requires considerable investigation and testing to determine the most appropriate modelling methods to use. Three principal methods are used:

- Boundary Element (BE)
- Finite Element (FE)
- Finite Difference (FD)

The BE method was not chosen, as computational costs for large problems are prone to escalate more rapidly than other methods. In addition, these methods are comparatively in their infancy and methods for the solution of regions containing nonlinear media are not widely covered in the literature.

The FE method requires only the co-ordinates of the solution points within the region modelled, PDE coefficient values, and boundary condition information to solve a problem. This generality and flexibility allows for easy application of the method to numerous different physical problems and for this reason was the method chosen to model current transfer in superconducting systems. The principal disadvantages with such methods are that they require complex mathematical analysis and extensive computer programing. Therefore, a commercial package (ABAQUS in conjunction with Femgen) was adopted. This package although used predominantly for structural analysis, does contain options for heat conduction analysis and claims to solve nonlinear problems. Using the electrical conduction analogue for heat conduction an exhaustive set of test models were computed and analysed to assess the software's ability to solve nonlinear problems. It was found that this package could reliably model systems only with very weak nonlinear properties and was abandoned.

A FD method was subsequently successfully developed and employed to calculate current transfer behaviour in current contacts (see section 6.4). This method however is not as general as the FE method and any significantly different current flow problem requires an entirely new program. The FE method was the final approach chosen and the principal method used for the modelling presented in this thesis as further development of nonlinear current transfer models required the flexibility previously mentioned. This was accomplished through the development of a suite of functions and programs written for the Matlab (matrix laboratory) mathematical analysis package. This takes advantage of the high level functionality of this software and most importantly its computational efficiency in handling matrix calculations, the principal mathematical operation of FE computation. Numerous alternatives are available for the FE representation of a PDE and subsequent solution. Each alternative is more appropriate for specific problems than others and considerable effort was invested in choosing the most suitable. The FE method presented

in this chapter is the most robust and general for the particular problem of current flow in nonlinear media.

4.3 The physical model

Numerical methods must be employed to model the current distribution in HTSs principally because of three reasons:

- The composite nature of many superconducting systems.
- The complex geometry of typical systems.
- The nonlinear resistivity of superconducting regions.

Most nonlinear models that describe current flow in HTSs are based on magnetic flux diffusion models and consider either isotropic superconductors[1,2], anisotropic superconductors in simple geometries[3,4] or superconductors in an a.c. magnetic field[5,6]. The principal methods used to solve the magnetic flux diffusion problems are collocation by points[7-9] and FD methods[6,10-13], all of which employ a rectangular grid of solution points. Only of late have a limited number of solutions employing FE methods emerged[2,14]. As far as the author is aware, the model presented in this thesis is the only FE model that solves current flow problems in anisotropic nonlinear media. Further, this is the only model that calculates the solutions of relatively complex geometries, composite structures, and geometries with crystallographic orientation that is not coincident with the global co-ordinate system of the geometry.

4.3.1 Magnetic flux diffusion

The current flow and electric field distribution are derived from the solution of a magnetic flux diffusion equation that describes the problem modelled. Superconducting regions are essentially treated as homogeneous nonlinear conductive media; i.e. the local resistivity of the media is nonlinearly dependent upon the local current density. This can be expressed by a constitutive relation between the local electric field vector, $\mathbf{E}$, and local current density vector, $\mathbf{J}$

$$\mathbf{E} = \rho(\mathbf{J})\mathbf{J} \tag{9.1}$$

which is a local and instantaneous response law on the time and space scales applicable in this model. For the purposes of the mathematical formulation used in the FE analysis and to ensure stable solutions the nonlinear function of resistivity, $\rho(\mathbf{J})$, must be increasingly, and at least weakly, monotonic.

The nonlinear flux diffusion equation is essentially a quasilinear parabolic equation for transient problems, which reduces to a quasilinear harmonic elliptical equation for steady state problems. The differential equation is quasilinear in that the nonlinearity occurs in the coefficients of the PDE and not the partial derivatives. In the low frequency limit, the electromagnetic fields of composite materials, consisting of normal and superconducting regions, can be described by the following Maxwell equation

$$\nabla \times \mathbf{E} = -\mu_0 \frac{d\mathbf{H}}{dt} \tag{9.2}$$

where the quantity μ_0 is the permeability of free space and $\mathbf{H}$ is the magnetic field strength vector. The model neglects the effect of the Meisner current using the simplification that the lower critical field is zero such that $B = \mu_0 H$, in which case the transport current is only related to the pinning forces and can be expressed as

$$\nabla \times \mathbf{H} = \mathbf{J}. \tag{9.3}$$

This is a reasonable approximation for fields larger than H_{c1} in high-κ superconductors for which $H_{c1} << H_{c2}$ [15]. As alluded to previously, the model is defined in a right hand rectangular Cartesian co-ordinate frame with axes x, y and z; referred to as the global frame. The $\mathbf{H}$ field is parallel to the z-axis, for the 2D models described, which for non-zero value of H engenders flux diffusion into the body of any magnetic material present. The induced current is assumed to be confined to the xy-plane. All model geometries are considered slab geometries that extend in the z-axis direction, and physical units are based upon unit integration through the thickness. Components of any fringing effect are assumed zero. Therefore, z-component derivatives of the magnetic field tend to zero and can be ignored. Combining equations (9.1), (9.2) and (9.3) the magnetic flux diffusion equation is derived

$$\mu_0 \frac{dH_z}{dt} = \nabla \bullet \left(\rho(H_z)\nabla H_z\right) \tag{9.4}$$

where the current dependence of ρ is now replaced by a functional dependence upon the gradient components of H_z. The time asymptotic solution of this equation provides the steady state solution of equation (4.4)[16]

$$\nabla \bullet \left(\rho(H_z)\nabla H_z\right) = 0. \tag{9.5}$$

The FE solution using linear interpolative functions over the solution region of equation

(4.5) (see section 4.4.1) is a more accurate but equivalent solution to models of current flow in nonlinear resistor networks.

In a similar manner, it is possible to derive a diffusion equation in terms of the electric field[5], as opposed to the magnetic field formulation presented above

$$\mu_0 \frac{d\mathbf{E}}{dt} = \rho(E)\nabla \bullet \nabla \mathbf{E} . \qquad (9.6)$$

The magnetic field formulation is adopted in this work for two principal reasons. Firstly, the inclusion of a magnetic field dependence in the resistivity term allows for the study of a field dependent EJ characteristic; equation (4.6) cannot be manipulated to provide such a dependence. Secondly, the functional dependence of the EJ characteristic used in this work develops a singularity at $E = 0$ for $\rho(E)$ in the nonlinear regime, which presents difficulties in the numerical solution of equation (4.6). Models using the $\mathbf{E}$ field formulation, with and without approximating the singularity, have been found not to converge using the nonlinear matrix equation numerical solving routines employed in this work.

In order to constrain the solution of equation (4.5) the PDE is supplemented by a set of boundary conditions along the boundary of the geometry, Γ, over which the magnetic diffusion equation is to be applied. The boundary condition required for the definition of the transport current is obtained from the limitation that the current must flow parallel to the surfaces of the model along insulating boundaries, $\mathbf{J} \bullet \mathbf{n} = 0$; where $\mathbf{n}$ is a unit vector normal to Γ. Given that the derivative of a constant valued function is zero, equation (4.3) implies

$$H_z = G \qquad (9.7)$$

where G is a constant. This corresponds to a boundary condition of the first type, also called a Dirichlet boundary condition. The field difference between boundaries of constant field value determines the applied current, which using Ampere's law for unit integration through the thickness for two boundaries, A and B, gives

$$\oint_{\Gamma} \mathbf{H} \bullet d\mathbf{l} = \left| H_A - H_B \right| = I_{app} .$$

At the point of current injection $\mathbf{E} \times \mathbf{n} = 0$, using equation (4.1) and (4.3) this can be expressed in terms of the magnetic field as $\rho(H_z)(\nabla \times \mathbf{H}) \times \mathbf{n} = 0$, which for 2 dimensions reduces to

$$\rho(H_z)\frac{\partial H_z}{\partial \mathbf{n}} = 0 . \qquad (9.8)$$

This corresponds to a zero value boundary condition of the second type, more commonly known as a homogeneous Neumann boundary condition. The application of boundary conditions is further discussed with respect to the FE method in section 4.4.4.

The functional form of equation (4.1) is still yet to be defined. The models presented in this thesis use the functional dependence of ρ adopted by Schuster *et al*[3] for anisotropic superconductors

$$\rho_{x'} = \frac{E_{x'}}{J_{x'}} = E_c \left| \frac{\left(J_{x'}\right)^{n-1}}{\left(J_{c,x'}\right)^{n}} \right| \tag{4.9a}$$

$$\rho_{y'} = \frac{E_{y'}}{J_{y'}} = E_c \left| \frac{\left(J_{y'}\right)^{n-1}}{\left(J_{c,y'}\right)^{n}} \right| \tag{4.9b}$$

$$\alpha = \frac{J_{c,x'}}{J_{c,y'}} \tag{4.10}$$

where the directions of the components of E and J and the critical currents $J_{c,x'}$ and $J_{c,y'}$ are defined in a local co-ordinate frame with axes x' and y', and α is the anisotropy ratio. When $x' \| x$ and $y' \| y$ the prime superscript is omitted. A power law dependence is widely used to describe the EJ characteristic of many superconducting systems and therefore allows the application of this model to very general problems involving superconducting components. This dependence is also typical of the behaviour of the EJ characteristic of Bi-2212 CRT material (see section 3.3.1). A range of values of α and n are used in this work to investigate the influence of these parameters upon current flow and reflect the range found by experiment. Values obtained from measurements on bulk materials are only applicable for use in models of a macroscopic scale, where the density of solution points is still approximately small enough to emulate the behaviour of the bulk material; i.e. the spatial resolution of the model is not on the same scale as the more complex behaviour and geometry of the microstructure of a superconductor. Models on the microscopic scale similarly use a range of values, however this is more for the purposes of qualitative assessment of the effect these parameters have on the current transfer behaviour.

4.4 Finite element approximation of the physical model

The physical problem has already been approximated by the mathematical description of PDE. The representation of the approximate solution to the PDE over the region, or domain Ω, by a matrix equation using the FE method is described in this section. The domain, Ω, is used to describe both the region in $\mathbb{R}^3$ and $\mathbb{R}^2$ over which the physical model and FE approximation applies (see figure 4.1). The surface bounding Ω is denoted by Γ. At this boundary, different conditions apply such as Dirichlet and Neumann boundary conditions, denoted by Γ_u and Γ_q respectively. The principal schemes for forming the FE description of the underlying PDE are the variational and weak formulation methods. Deriving an appropriate energy function for use in the variational method for nonlinear differential equations, or a situation where discontinuous interface conditions exist, is complicated and a suitable function may not even exist. Indeed tests for existence themselves are not trivial. In developing a model that can be used with greatest generality the weak formulation is chosen in preference, since it holds for a large class of problems, including nonlinear PDEs.

A classical solution of equation (4.4) or (4.5) that is defined at every point over Ω must have continuous second order partial derivatives. However, if discontinuities exist in the solution, for example across internal boundaries between dissimilar magnetic media, then this continuity condition no longer holds. This requires the reformulation of the PDE into a weak representation, as described in section 4.4.2, where the requirement for second order continuous derivatives is weakened at the expense of the introduction of another solution variable. The continuous solution of the classical solution is replaced by a discrete solution that applies only at a certain number of points, nodes, over Ω. In the method presented, these nodes coincide with the vertices of planar triangles that tessellate over Ω forming a mesh. Approximating functions are used to describe the solution over the triangle and substituted into the weak formulation of the PDE over the triangle. A matrix equation, which describes the solution over the entire problem, is found by the summation of the weak integral of every triangle in the problem geometry and subsequent application of boundary conditions. The solution of this matrix equation gives the solution of the PDE, or equivalently the coefficients of the approximating

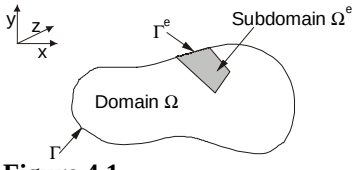

Figure 4.1
Diagram indicating both global and elemental domains and boundaries.

functions, from which the solution is derived.

4.4.1 Overview of the finite element method

The FE method involves separating the continuum of space over which a differential equations applies (the domain Ω) by imaginary lines into a number of polygonal, non-overlapping sub-regions, Ω^e, (finite elements), (see figures 4.1 and 4.2). For the models presented, the element shape is the plane triangle. The solution over the element is assumed to follow a local approximating trial function, $\hat{u}$, and for a plane triangle defined by the three vertices or nodes l, m, n, a component of the solution may be approximated by the simple polynomial

$$\hat{u} = \alpha_1 + \alpha_2 x + \alpha_3 y = \sum_{\Omega^e}^{i=l,m,n} N_i^e(x,y) U_i^e \,. \tag{4.11}$$

The approximation of the solution over each element is generated by functions of position called shape functions, N_i^e, (see Appendix B) that linearly interpolate the local value of the solution with respect to the nodal values that represent the discreet solution, and are the points that correspond to the solution values calculated. The functions N_i^e maintain continuity at the element boundaries in that they satisfy the conditions $N_i^e(x_l, y_l) = 1$ while $N_i^e(x_m, y_m) = N_i^e(x_n, y_n) = 0$, etc. That is, the shape functions preserve the nodal values of the function at the node positions. The derivative of $\hat{u}$ is obtained by direct partial differentiation of equation (4.11) and is calculated at the triangle barycentre. This calculation provides the value of the components of the local current density; the dependent variable of the nonlinear resistivity function used in the FE models of this thesis.

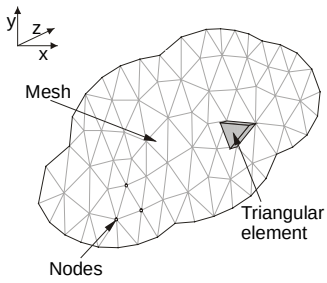

Figure 4.2
Schematic of finite element mesh, indicating the planar triangular element and nodes at triangle vertices.

For the weak formulation FE method employed in this work the PDE representing the physical problem is replaced with an integral equation over the element and the trial function is substituted. By using a weak formulation of the integral equation the continuity conditions of the solution can be reduced at the expense of introducing a weighting function. This is discussed in the next section. Due to the implicit satisfaction of the boundary conditions at element boundaries, the elemental integrals can be

summed to provide the integral over the entire domain Ω by a process known as assemblage. Whereas the homogeneous Neumann boundary conditions used in the models presented are automatically satisfied by the integral equation, in order to satisfy the Dirichlet boundary conditions the integral equation is constrained by specifying the value of the solution at the nodes along the boundary condition. The final integral equation is usually expressed as a matrix equation, the solution of which gives the best fit for the trial function parameters and hence the solution values at the nodes. The solution of matrix equations is a separate branch of numerical mathematics and is considered in greater detail in section 4.5.1.

4.4.2 The weak formulation

The magnetic field solution of the heterogeneous structures of the composite and nonlinear systems modelled in this thesis, where the conductivity changes spontaneously across a region, are in general not smooth functions and therefore can not be differentiated as many times as the governing differential equation requires. Indeed this is why the PDE system is not soluble analytically, in the sense of providing classical solutions. To overcome this problem the differential equation is replaced by an equivalent integral relation. This has the advantage that it involves fewer derivatives of the unknown function than the solution of the equivalent PDE and in this way accommodates solution discontinuities.

Consider the more general form of equation (4.4) with solution variable u

$$\varepsilon \frac{\partial u}{\partial t} - \nabla \bullet \left(D \nabla u \right) = f \qquad \text{on } \Omega \tag{4.12}$$

$$u = l\left(x, y, z, t\right) \qquad \text{on } \Gamma_u \tag{4.13}$$

$$D \frac{\partial u}{\partial n} = 0 \qquad \text{on } \Gamma_q \tag{4.14}$$

and initial condition

$$u = h\left(x, y, z\right) \qquad \text{at } t = 0 \tag{4.15}$$

where $\frac{\partial u}{\partial n} \equiv \nabla u \bullet \mathbf{n}$ is the normal derivative on Γ and $\Gamma = \Gamma_u \cup \Gamma_q$ with $\Gamma_u \cap \Gamma_q$ disjoint; further ε and f are a constants and D is a smooth function which can depend on x, y, z or u as well as the first derivatives of u.

To obtain the integral relation of the above system, the PDE is multiplied by the smooth function, v ($v \in C^2\left(\Omega\right)$), called the test function, and integrated by parts over Ω and Γ using Green's first identity[17,18]

$$\int_\Gamma \Phi K\nabla u \bullet \mathbf{n} d\Gamma = \int_\Omega \Phi\nabla \bullet \left(K\nabla u\right)d\Omega + \int_\Omega \nabla\Phi \bullet \left(K\nabla u\right)d\Omega .$$

This identity is valid for u, K and Φ, together with the first derivatives of u and K, and the second derivative of Φ continuous in Ω ($u \in C^1(\Omega), K \in C^1(\Omega), \Phi \in C^2(\Omega)$).

Integrating by parts

$$\int_\Omega \varepsilon \frac{\partial u}{\partial t} v d\Omega = \int_\Omega v\left(\nabla \bullet \left(D\nabla u\right)\right)d\Omega + \int_\Omega fvd\Omega$$

$$= -\int_\Omega \nabla v \bullet \left(D\nabla u\right)d\Omega + \int_\Gamma vD\nabla u \bullet \mathbf{n} d\Gamma + \int_\Omega fvd\Omega \quad (4.16)$$

and since Γ is the disjoint union of Γ_u and Γ_q

$$\int_\Gamma vD\nabla u \bullet \mathbf{n} d\Gamma = \int_{\Gamma_u} vD\nabla u \bullet \mathbf{n} d\Gamma + \int_{\Gamma_q} vD\nabla u \bullet \mathbf{n} d\Gamma . \quad (4.17)$$

If the choice of u is restricted to satisfy the Dirichlet boundary condition, equation (4.13), then the first term of (4.17) can be omitted by restricting the choice of v to functions that vanish ($v \equiv 0$) near the boundary Γ_u (see section 4.4.4). Applying the homogenous Neumann boundary condition, equation (4.14), the second term of (4.17) becomes zero, such that natural boundary conditions do not explicitly enter equation (4.17). Combining equation (4.16) and (4.17), gives the weak formulation of the system of equations (4.12)-(4.15),

$$\int_\Omega \varepsilon \frac{\partial u}{\partial t} v d\Omega = -\int_\Omega \nabla v \bullet \left(D\nabla u\right)d\Omega + \int_\Omega fvd\Omega . \quad (4.18)$$

The integral now involves only first order differentials and can be calculated for non-zero finite values of the first order derivatives, piecewise continuous, of u, v ($u \in C^0(\Omega), v \in C^0(\Omega)$) and non-zero finite values of D.

If u is a twice differentiable solution of the system of equations (4.12)-(4.15) then u is a classical or strong solution. However, if u is a solution of equations (4.12)-(4.15) but does not have the required number of derivatives to be a classical solution then u is a weak solution. The weak solution reduces the order of the derivative of u in the governing PDE at the price of a higher order of derivative for v. This formulation allows the specification of a system with discontinuous solutions and coefficients.

4.4.3 The Galerkin method

Having specified the governing PDE as an integral relation and introduced the test function v, a choice now remains as to the functional form of v. The function that is most widely used is the same function that approximates u. The FE method that employs this

choice of test function is called the Galerkin method[19] and is chosen in this analysis. This method is considered the most consistent for good accuracy in a wide range of problems and is the most examined in the literature. In linear analyses, this method frequently leads to symmetric matrices and therefore greater computational efficiency (see section 4.5.3).

The solutions of the models presented are in the 2D space of the xy-plane. Expanding the scalar product of the weak formulation of equation (4.18) into the constituent partial derivatives over the elemental domain, Ω^e, and equating all z-derivatives to zero by imposing the zero fringing field condition gives

$$\int_{\Omega^e} \varepsilon \frac{\partial u}{\partial t} v d\Omega = -\int_{\Omega^e} \left(\frac{\partial v}{\partial x} D \frac{\partial u}{\partial x} + \frac{\partial v}{\partial y} D \frac{\partial u}{\partial y} \right) d\Omega + \int_{\Omega^e} f v d\Omega . \tag{4.19}$$

Substitution of the trial function and test function, with shape functions N_j^e, into the weak formulation provides a matrix equation for the solution of u over a single element

$$\mathbf{M}^e \dot{\mathbf{U}}^e + \mathbf{K}^e \mathbf{U}^e + \mathbf{f}^e = \mathbf{0} \tag{4.20}$$

with

$$K_{ji}^e = \int_{\Omega^e} \left(\frac{\partial N_j^e}{\partial x} D \frac{\partial N_i^e}{\partial x} + \frac{\partial N_j^e}{\partial y} D \frac{\partial N_i^e}{\partial y} \right) d\Omega$$

$$f_j^e = -\int_{\Omega^e} N_j^e f d\Omega$$

$$M_{ji}^e = \int_{\Omega^e} N_j^e \varepsilon N_i^e d\Omega$$

$$\dot{\mathbf{U}}^e \equiv \frac{d}{dt} \mathbf{U}^e .$$

The matrix $\mathbf{K}^e$ is known as the element stiffness matrix, the matrix $\mathbf{f}^e$ is the element load vector and $\mathbf{M}^e$ is called the element damping matrix. The integration of these terms is carried out numerically. If D is a function of position over Ω^e then numerical integration is computationally expensive. It is generally more efficient to assume D has a single value over the element and obtain the desired accuracy of the solution by using a finer mesh. This is particularly so in the case of linear elements that often do not describe accurately the solution on coarse meshes. Numerous numerical integration schemes exist. This analysis adopts a scheme using the area co-ordinate system. This is the most appropriate for linear elements with single valued D as the integration can be carried using simple formulae[20] and is therefore computationally inexpensive. These equations only apply over the region of a single element and must be extended to approximate the

solution over the entire region of the problem modelled; this involves the construction of global system matrices.

4.4.4 The global system matrix and application of boundary conditions

The elemental approximation must be extended to cover the entire domain, Ω, and in this analysis is constructed element by element as opposed to nodal composition. The element equations are assembled for the whole problem by superposition, removing redundancy at shared nodes. This process is known as assemblage and forms a matrix equation akin to (4.20) where the locally defined element matrices are replaced by global system matrices. The construction of the global integral from the elemental integral uses the property of the definite integral that over the volume V the total integral is equivalent to the sum of the integrals of the subdomains, V^e, composing V; that is

$$\int_V (\ )dV = \sum \int_{V^e} (\ )dV \ . \tag{4.21}$$

The approximation of u over each element was defined to satisfy automatically the continuity conditions imposed by the weak integral and therefore the inter-element continuity required by (4.21). Therefore

$$K_{ji} = \sum K_{ji}^e$$

$$f_j = \sum f_j^e$$

$$M_{ji} = \sum M_{ji}^e$$

and equation (4.20) can be rewritten as

$$\mathbf{M}\dot{\mathbf{U}} + \mathbf{K}\mathbf{U} + \mathbf{f} = \mathbf{0} \tag{4.22}$$

where $\mathbf{U}$ lists all the nodal points of Ω and $\mathbf{M}$, $\mathbf{K}$, $\mathbf{f}$ are the summations of the element matrices $\mathbf{M}^e$, $\mathbf{K}^e$, $\mathbf{f}^e$ and constitute the global system matrices respectively.

Also, note

$$\dot{\mathbf{U}} \equiv \frac{d}{dt}\mathbf{U} \ .$$

The construction of the global matrices must respect the topology of the elements defined in the mesh constructed over Ω. Various ordering schemes exist to ensure this criterion is met[21,22]. The process of assemblage is one of systematic ordering and offers no insight into the FE formulation and will not be described; other than to say that assemblage orders the global matrix using the local element nodes l, m, n with the global node list $\mathbf{U}$.

The homogeneous Neumann boundary condition is automatically satisfied by equation (4.20) however it remains to apply the conditions necessary to satisfy the Dirichlet boundary conditions. Prescribing the value of the solution at the nodes along the boundary where the Dirichlet condition applies, Γ_u, fixes, and thereby reduces some of the unknowns. There a several methods used to set the value at the nodes along Γ_u, such as wiping columns and rows in the system matrices or the reduced formulation. The models described in this thesis use Lagrange multipliers to specify the constraints placed upon these nodes. Forcing equation (4.22) to satisfy implicitly the Dirichlet boundary condition term ensures the condition $\mathbf{v} \equiv \mathbf{0}$, discussed in section 4.4.2, is met and the first term of equation (4.17) vanishes.

4.4.5 Meshing the problem domain

As stated previously the region over which the PDE system applies is approximated by a union of geometrical objects, elements, that form a mesh (see figure 4.2). A series of Matlab functions are used to generate automatically the mesh for the model geometries presented. Triangular elements are used because they readily describe non-rectilinear geometries, unlike rectangular elements that require finer meshing at oblique boundaries or a transformation of the local co-ordinate system to 'bend' element edges on curved boundaries. The simplicity of the mathematical description of triangular linear elements leads to computational simplicity in the FE analysis and in turn to computational efficiency; i.e. automatic meshing algorithms, shape functions and numerical integration formulae are easily calculated. The construction of a suitable mesh is not an exact science. Experience must often be relied upon to decide how to size and position the component elements optimally, in order to obtain an accurate solution that efficiently uses a finite number of solution points. Indeed, much of the effort involved in defining a new problem is expended in finding a suitable mesh. This has lead to the increasing use of neural networks, taught by FE engineers, to generate suitable meshes for different FE problems[23]. However, there are some general rules that can be applied when defining, or accepting, an automatically generated mesh:

- The sides of a triangular element should run in the direction of greatest change in the approximate solution, such that the greatest change in the approximate solution is integrated along the greatest dimension.
- Equilateral elements are more accurate than long narrow triangular elements.

- The region of greatest change in the solution should be finely meshed. This not only gives greater accuracy of the solution in this region but by more accurately representing the solution over the entire domain leads to greater accuracy in regions where the solution changes little.

4.5 Solution methods, limitations and efficiency

The FE method transforms the PDE representing the physical problem into a matrix equation, the solution of which is a different branch of mathematics. Numerous solution methods have been examined for accuracy and computational efficiency, and are discussed in this section. The range of parameters for which a solution to a model can be found and the influence of the FE mesh are also discussed.

4.5.1 The solution of nonlinear matrix equations

Once the matrix equation (4.22) is constructed it can almost be considered a different problem; that of the numerical solution of simultaneous equations. If the parameter D of equation (4.22) is constant and therefore the system of equations is linear then the solution of (4.22) is simply obtained by the operation of matrix division. However if D is nonlinear then the global stiffness matrix $\mathbf{K}$ has a nonlinear dependence on the solution, $\mathbf{K}(\mathbf{U})$, and an iterative solution process must be used. Equation (4.22) becomes

$$\mathbf{M}\dot{\mathbf{U}} + \mathbf{K}(\mathbf{U})\mathbf{U} + \mathbf{f} = \mathbf{0} \tag{4.23}$$

and in the steady state

$$\mathbf{K}(\mathbf{U})\mathbf{U} + \mathbf{f} = \mathbf{0}\,. \tag{4.24}$$

For the magnetic flux diffusion equation employed in the solution of current transfer problems the dependent solution variable U represents the magnetic field strength, denoted by the variable H.

The nonlinear solution method adopted in this work is the Newton-Raphson method, which is a robust solution process for many nonlinear equations. Nonlinear solution methods invariably rely upon the Jacobian of the nonlinear term of the matrix equation. Quite often, even if the Jacobian can be expressed in explicit functional form, it is so large and/or functionally complex that it is computationally inefficient to use. Two principal methods were used to approximate the Jacobian:

Fixed: The Jacobian of a nonlinear matrix is approximated as equivalent to the nonlinear matrix, $\mathbf{K}(\mathbf{U})$.

Finite Difference: The Jacobian is calculated by a finite difference approximation.

A test model was used to determine the most appropriate Jacobian to use and it was found that both produced solutions accurate to the same significant figure, for a number of different boundary values. Solutions obtained using a fixed Jacobian were fastest, and this approximation has been used in all FE models presented.

Alternatives to, and variations upon, the Newton-Raphson solution method have been examined for accuracy and speed of computation, with steady state models using standard and modified Matlab functions. Newton-Raphson and the Levenberg-Marquardt algorithms using either a cubic, mixed quadratic and cubic, or Armijo-Goldstein line search methods have been tried along with fixed or finite difference approximation of the Jacobian (see table 4.1). All variations failed to provide a solution except certain variations upon the Newton-Raphson method. Either the nonlinear matrix became singular or the solution process was summarily terminated because the solution took a prohibitive amount of time. The Newton-Raphson method employing the Armijo-Goldstein line search strategy was found the fastest and has been used for all the models developed. Numerous different desktop personal computers and workstations have been used during the course of this work and any solution times quoted in this thesis refer to solutions computed using a Pentium II Xeon 400 MHz processor with 512 Kb on board cache and 256 Mb RAM which was dedicated to this work.

Solution of the transient problem, equation (4.23), requires somewhat different numerical methods. Initially, implicit, semi-implicit and explicit methods were coded to solve simple nonlinear transient problems. Whereas implicit methods were found to be faster than explicit methods, convergence to the solution was still slow. The Matlab functions for solving ordinary differential equations have been found to be faster and have replaced the implicit and explicit solution methods. The function ‘ode15s’ in combination with a bespoke function determining the fixed Jacobian per solution iteration solves the transient

Table 4.1 *The nonlinear solution methods of a FE matrix equation.*

	Mixed quadratic and cubic		Cubic		Armijo-Goldstein	
	Fixed Jacobian	Finite difference Jacobian	Fixed Jacobian	Finite difference Jacobian	Fixed Jacobian	Finite difference Jacobian
Newton-Raphson	Solution	No solution	No solution	No solution	Solution	Solution
Levenberg-Marquandt	No solution	No solution	No solution	No solution	N/A	N/A

equation (4.22) using numerical differentiation formulae[24]. This function is superior to the explicit and implicit schemes in that it can solve problems that have a greater degree of stiffness and, through the use of a variable time step increment, do so more efficiently. A stiff problem is one that changes on a time scale that is very short compared to the time interval over which the change in the solution is of interest. This decreased the time of convergence to the solution and allowed more complex problems to be solved. However all the steady state problems that have been analysed, except some of those presented as validation models in chapter 5, possess too high a degree of stiffness to be solved for the transient case on a desktop personal computer and so are not dealt with in this work except for the purposes of model validation.

4.5.2 The computational limitations of the finite element model

The main factors that govern the cost of computation for a solution to a model are the number of nodes within the mesh of the model and the degree of nonlinearity imposed on the system of governing equations. A fundamental requirement of any solution to a model is that the spatial resolution is sufficient to analyse the behaviour of current flow on the scales of interest. Mesh design can minimise the number of nodes in a mesh suitable for this requirement but at some point places a lower limit on the number of nodes used in the solution. Consequently, the physical parameters used in the model ultimately determine computational costs of a solution. Whereas in principal the range of values and functionality is only limited by the proviso that such values and functions do not become singular (i.e. remain finite), the computation times involved in their solution may become prohibitive and thereby place limitations on the range of physical parameters a model can practically solve. The value of α and n control the severity of the functional nonlinearity of a solution interdependently and therefore the ease of convergence of the solution to within a defined accuracy. This interdependence is complex so the practical availability of a solution for a particular set of α and n was determined by trial and error.

4.5.3 Computational efficiency and matrix properties

Computational efficiency must always be considered where an iterative solution method is employed. Various matrix properties can effect the speed of solution of a matrix equation. Specifically, four matrix properties were considered and optimised for maximum computational efficiency, both in the program code and Matlab proprietary functions. These are discussed below.

Matrix sparsity

FE methods require operations on matrices that contain only a small proportion of non-zero elements; these matrices are called sparse matrices. Computation time is reduced if only the non-zero elements and their indices are stored, as this both eliminates operations on zero elements and reduces the amount of memory storage used.

Matrix factorisation

Solution of the matrix equation

$$\mathbf{Ax} = \mathbf{B}$$

where **A** and **B** are given sparse matrices, is the most computationally expensive operation involved in the FE process. Direct as opposed to iterative methods to solve this equation are faster, and involve factorisation of the matrix. The factorisation splits the original matrix equation into a set of further equations each involving one of the factors. Matrix factorisation schemes, that produce a matrix product involving a triangular matrix, have advantages in that forward or back substitution depending on whether an upper or lower triangular matrix is formed respectively can be used to solve the equation. These methods are in of themselves relatively fast and the symmetry of triangular matrices can be employed to reduce further computational storage and operations costs.

Matrix reordering

Reordering schemes help make the matrix factors expanded from a matrix sparser. Methods generally achieve this by reducing the bandwidth of the matrix, or producing a fractal like structure with large blocks of zeros.

Matrix symmetry

In a symmetric matrix, the elements above and below the leading diagonal are mirror images of each other, consequently half of the full matrix is implicitly known. A symmetric matrix therefore requires less storage and floating point operations per matrix operation. Matrix equations involving symmetric matrices also have more efficient solution methods and reordering schemes. However, with the exception of the mass matrix of the transient solution, the nonlinear matrix systems solved in this thesis did not contain symmetric matrices and therefore lacked the computational efficiency of the symmetric matrix.

4.6 Postprocessing

The mathematical representation of the solution of a model is a matrix of solution values that are associated with a matrix of solution point co-ordinates. The solutions presented contain between 10,000 and 120,000 solution points and as such are impossible to interpret without transposition to a graphical representation. Different solution properties such as J and E must be calculated for the visualisation of different physical characteristics. The mathematical manipulation and visualisation of the FE solution is a process known as postprocessing. Solutions have been processed and plotted through the use of specifically tailored functions and high level Matlab graphing routines. As discussed previously the FE model produces the magnetic field solution, H, of a problem. Other physical quantities can be obtained from this solution by the application of the laws of electromagnetism. Principal amongst these quantities are J, E, ρ and differences in the electrical potential, ϕ, throughout the model geometry. The current dependence of ρ is introduced by equation (4.3), and used to generate current density plots. For the limitations placed on H and J as described in section 4.3.1

$$\mathbf{J} = \frac{\delta H_z}{\delta y}\mathbf{x} - \frac{\delta H_z}{\delta x}\mathbf{y}.$$

From which the local resistivity distribution of nonlinearly resistive components can be readily calculated using equations (4.9a) and (4.9b). Given J and ρ, the constitutive relation (4.1), facilitates the calculation of the electric field distribution within the model, from which the electric potential can be determined using the line integral

$$\phi(\mathbf{r}_B) - \phi(\mathbf{r}_A) = -\int_A^B \mathbf{E} \bullet d\mathbf{l}.$$

One of the disadvantages with using the magnetic field formulation to calculate the current density and electric field distribution within a model is that both these quantities involve the first order derivative of the solution and so require greater mesh refinement to describe accurately J and E over the model geometry.

The three principal graphing techniques used are contour, vector and line plots. Vector plots have been used in combination with contour plots to describe the distribution of J, E, ρ and their x and y components. Such plots provide both intuitive understanding of the physical problem modelled and an insight into important features of the current transfer. However, in light of the hundreds of solutions that are calculated for each model and the high information density of the contour plots of the physical variables and their

components, a systematic evaluation of the behaviour of a model that explores the entire solution and set of variables is unwieldy and inefficient; as any characteristic behaviour is implicitly expressed throughout the set. Line plots of the solution variables along a single dimension of the models and surface integrals have been used to describe more concisely aspects and dependencies of the current transfer behaviour. An extensive set of data processing and graphics routines has been written and adapted for each model. As these routines perform complex operations on gigabytes of solution data the length of postprocessing computation time must be considered when determining the number of model solutions to calculate and the interpolation density of postprocessed output.

4.7 Summary

The physical model and mathematical techniques employed in the coding of the computer implementation of the model have been researched and described. Different approaches to the solution of the physical model have been researched and discussed. Various solution methods of the nonlinear matrix equation have been examined for optimal efficiency and accuracy. The issues involved in developing and executing the data processing and visualisation programs used in this work have been presented. The high accuracy of the computer model described in this chapter is demonstrated in the following chapter where solutions of the model are verified against analytical and intuitive models.

4.8 References

1 E. H. Brandt, Physical Review B-Condensed Matter **52,** 15442-15457 (1995).

2 J. Paasi and M. Lahtinen, Ieee Transactions On Applied Superconductivity **7,** 322-325 (1997).

3 T. Schuster, H. Kuhn, E. H. Brandt, and S. Klaumunzer, Physical Review B-Condensed Matter **56,** 3413-3424 (1997).

4 A. Gurevich, International Journal Of Modern Physics B **9,** 1045-1065 (1995).

5 J. Rhyner, Physica C **212,** 292-300 (1993).

6 J. K. Sykulski, R. L. Stoll, A. E. Mahdi, and C. P. Please, Ieee Transactions On Magnetics **33,** 1568-1571 (1997).

7 T. Schuster, H. Kuhn, E. H. Brandt, M. V. Indenbom, M. Klaser, G. Mullervogt, H. U. Habermeier, H. Kronmuller, and A. Forkl, Physical Review B-Condensed Matter **52,** 10375-10389 (1995).

8 Z. Koziol and R. A. Dunlap, Journal Of Applied Physics **79,** 4679-4681 (1996).

9 E. H. Brandt, Physical Review B-Condensed Matter **54,** 4246-4264 (1996).

10 C. J. Vanderbeek, G. J. Nieuwenhuys, P. H. Kes, H. G. Schnack, and R. Griessen, Physica C **197,** 320-336 (1992).

11 A. E. Curzon, F. Hamed, and S. Gygax, Physica C **292,** 189-196 (1997).

12 J. Gilchrist and T. Dombre, Physical Review B-Condensed Matter **49,** 1466-1469 (1994).

13 A. E. Mahdi, R. L. Stoll, J. K. Sykulski, C. Beduz, T. Hughes, Y. Yang, M. R. Harris, and R. J. Arnold, Physica C **235,** 2419-2420 (1994).

14 L. Prigozhin, Ieee Transactions On Applied Superconductivity **7,** 3866-3873 (1997).

15 E. Zeldov, J. R. Clem, M. McElfresh, and M. Darwin, Physical Review B-Condensed Matter **49,** 9802-9822 (1994).

16 C. V. Pao, *Nonlinear Elliptic and Parabolic Equations* (Plenum, New York, 1992).

17 A. E. Taylor and W. R. Mann, *Advanced calculus*, 3rd ed. (John Wiley & sons, inc, 1983).

18 R. E. White, *An introduction to the finite element method with applications to nonlinear problems* (John Wiley & sons, 1985).

19 B. G. Galerkin, *Rods and Plates* (Fed. Sci. Tech. Info., Springfield, 1915).

20 P. C. Hammer, Math. Tables Aids Comp **10,** 130-7 (1956).

21 O. C. Zienkiewicz, *The Finite element method*, Vol. 1, 4th ed. (McGraw-Hill, London, 1989-1991).

22 G. Dhatt and G. Touzot, *The finite element method displayed* (Wiley, Chichester, 1984).

23 D. N. Dyck, D. A. Lowther, and S. McFee, Ieee Transactions On Magnetics **28,** 1767-1770 (1992).

24 L. F. Shampine and M. W. Reichelt, Siam Journal On Scientific Computing **18,** 1-22 (1997).

CHAPTER 5

Validation of solution techniques

5.1 Introduction

The solutions of any numerical model must be tested, if possible, against known solutions of the system modelled in order to verify that it is correctly described. This process is one of validation[1] and employs intuitive and analytical solutions for the purposes of testing[2]. Only after validation can a numerical model be reliably used to approximate the solutions of a system that are not self-evident, or beyond the scope of analytical solution techniques. This chapter presents such a comparison of numerical solutions of FE models against exact analytical solutions and the solutions of problems that can be arrived at intuitively.

During development various checks of the computer program were carried out. Although most solutions presented are for the nonlinear regime, the program was tested to see whether it could produce the correct solution to a linear model as a limiting case. The series summation approximation of the exact analytical linear anisotropic solution of the Laplace equation in a rectangular geometry with various applied boundary conditions was compared to a FE approximation, and found to be in good agreement. The computed solutions have routinely been checked for self-consistency of the inferred physical values such as J, E and the local resistivity value, as well as for appropriate mapping behaviour of the solution at lines of symmetry within the geometry of a model. For example, note the symmetry of figures 5.4, 5.6 and 5.7. Fulfilment of the conditions that E and J must satisfy at boundaries with applied Neumann and Dirichlet conditions have also been checked. Compliance with the maximum-minimum principle has been verified for all the models computed. The theorems of this principle require that the maximum and minimum values of the solution of the steady state equation used in this analysis (an equation with solution variable H), as described by an harmonic elliptical equation, must occur on the closed continuous boundary of the region over which the problem is defined[3]. The results of this chapter show that the numerical methods used provide solutions which are consistent with the known solution of several models. When methods are used to solve more complex problems with unknown solutions it is good practice to compare solutions

with several error tolerances and initial guesses as a further validity check. This has been performed for all the models presented in this thesis.

The models detailed in section 5.2 demonstrate, principally through the use of intuitive models, that the programming methods employed correctly deal with the nonlinearity of the EJ characteristic and anisotropy of the critical current density in the steady state; the main physical aspects explored in the major work of this thesis. The effects of these parameters within the models are also investigated and are presented in section 5.3. The transient response is covered in the latter half of the chapter to illustrate the computer programs ability to approximate, exact analytical solutions satisfactorily; a further indication of the validity of the steady state models.

5.2 The slab and constricted slab models: An intuitive model comparison

The constricted slab geometry is described in this section and used to validate the solution technique for models in the steady state. The FE models described in this thesis treat the superconducting components of composite structures as nonlinear electrically conductive media; i.e. locally, the resistance of the superconducting region is determined by a power law current dependence (see section 4.3). This makes current transfer in many situations difficult to grasp intuitively. Understanding how geometry will influence the current distribution is complicated by the implicit dependence of the local resistivity upon the local current density; i.e. a high local current density will induce a high local resistivity value, which in turn favours a low local current density. The addition of a critical current anisotropy factor further complicates the matter, since these dependencies are different for perpendicular directions within the geometry.

5.2.1 The slab model

Any set of geometry and boundary conditions that induces a non-uniform current distribution (for example current crowding at the corner of an L-shaped current lead) introduces a local resistivity contribution to the current transfer. The converse however is not true. A current dependent local resistivity distribution cannot be supported by a uniform current distribution since a single valued current density automatically implies a single valued resistivity across the entire geometry. Given a nonlinear media, only one

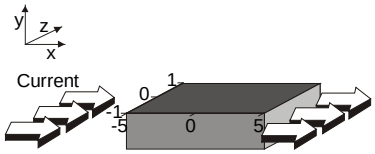

Figure 5.1
Schematic of slab geometry, arrows show the applied current direction. Dimensions are in millimetres.

geometry subject to an applied constant current condition has uniform current flow. This is the rectangular or square slab with applied current at opposing ends (see figure 5.1).

A 2D FE model of the geometry of figure 5.1 in plan view was calculated to test that the current distribution was uniform. Indeed the current density was single valued, $J = 2\times10^{7}$ A·m^{-2}, throughout the geometry. The electric field was also single valued, $E = 3.2\times10^{-3}$ V·m^{-1}, and appropriate for a superconducting region with an n-value of 5 and electric field and current density criteria of 1×10^{-4} V·m^{-1} and 1×10^{7} A·m^{-2} respectively.

5.2.2 The constricted slab model

To demonstrate the solution techniques employed accurately calculate the steady state current flow in a superconductor, as approximated by the model, a numerical model that possesses an intuitive solution was developed for comparison. This was composed of two abutting slab geometries, one half the width of the other; the interface region between the slabs having a step-like structure which forms a constriction (see figure 5.2). The model incorporated a nonlinear resistivity and the same current condition as the slab model of section 5.2.1 was applied at the ends of the constricted slab geometry, as shown in figure 5.2. At locations away from the region of constriction, where edge effects can be neglected, the geometry simplifies locally to the slab geometry and the current distribution is uniform. Within the one model there are two regions with uniform current distribution, one with half the area and therefore twice the current density. Therefore, the two regions have different electric field values. In the nonlinear case, these are not simply different by a factor of two but by a factor of 2^{n}, where n is the exponent of the power law describing the EJ characteristic. The E and J values along the midline of the model geometry (see figure 5.2) were determined from a FE approximation of this model (see figure 5.3). The FE model had an n-value of 5 and an applied current, $I_{app} = J_c^m A$, within the region of current injection. The physical dimensions are described in figure 5.2; the figure indicates that the x-axis co-ordinate of the constriction is 0. Figure 5.3 shows that E changes by a factor 2^{5} in good agreement with the

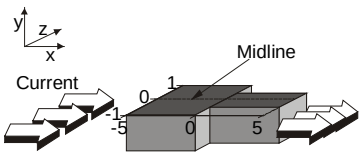

Figure 5.2
Schematic of constricted slab geometry, arrows show the applied current direction. Dimensions are in millimetres.

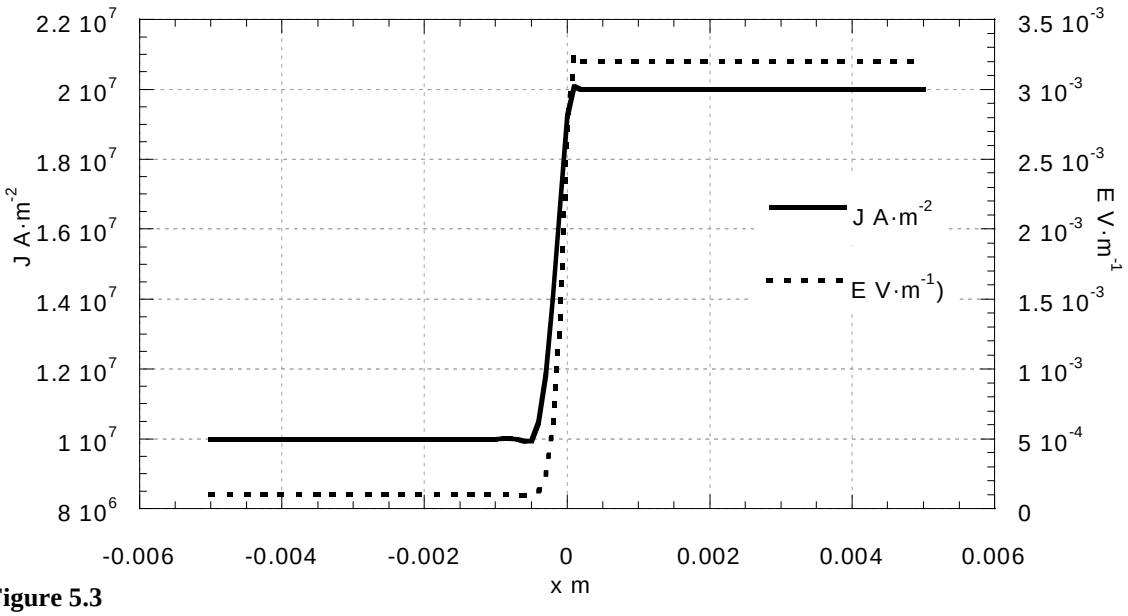

Figure 5.3
Current density and electric field values along midline of isotropic constricted slab model, with n =5.

intuitive model. Further note that E and J are correctly related by the $n = 5$ power law EJ characteristic.

The behaviour of the constricted slab geometry has also been examined in the anisotropic regime. In the models studied the direction of the x-axis has been defined as the easy path for current flow. To verify that the nonlinear anisotropy conditions are correctly described, a model of two constricted slab geometries, side by side, with the same dimensions, identical anisotropic resistivity functions and applied current conditions was constructed. One of the geometries was rotated through an angle of 90° and therefore had regions of uniform current flow which were subject to different components of the anisotropic resistivity function. For a power law resistivity function with n-value 5 and anisotropy factor 10, the electric field value was found to be 1×10^{-4} V·m^{-1} and 10 V·m^{-1} along the broad section and 3.2×10^{-3} V·m^{-1} and 320 V·m^{-1} along the narrow section of the horizontal and vertical geometries respectively. This is in agreement with values calculated using equations (4.9a) and (4.9b).

5.3 Current flow in the constricted slab model

The behaviour of current flow in the constricted slab model is examined in this section. The isotropic and anisotropic regimes are investigated and discussed with reference to macroscopic inhomogeneity in bulk HTS. The approximation of structures composed of nonlinear media using Ohmic conductors is also studied.

5.3.1 The isotropic constricted slab model

The behaviour of the constricted slab geometry has been examined in the isotropic regime. Figure 5.4 presents contour plots of the current density magnitude in the constricted slab geometry and shows that current crowding occurs at the inner corners of the constriction. Examination of the current density magnitude along the midline of the solution for $n = 1-10$ ($n = 1$ is equivalent to the Ohmic resistance ρ_0) (see figure 5.5) indicates that current transfers over a smaller longitudinal region in the nonlinear regime ($n \neq 1$). This is an artefact of the of the current density distribution, current density contour lines are convex in the isotropic linear regime, becoming increasingly concave in the nonlinear regime. In the nonlinear regime, current crowding at the corners of the constriction leads to high local resistivity values compared to the linear regime. In order to minimise the local resistivity value, current transfers through the constriction more evenly across the width of the geometry (note that for positions greater than 1.28×10^{-4} m, $J\,(n=1) < J\,(n>1)$).

Figure 5.5 indicates that the length over which the current density change along the midline becomes smaller. However, for $n > 2$ this is inconclusive. Solutions were calculated employing three different meshes and some variation of the midline current

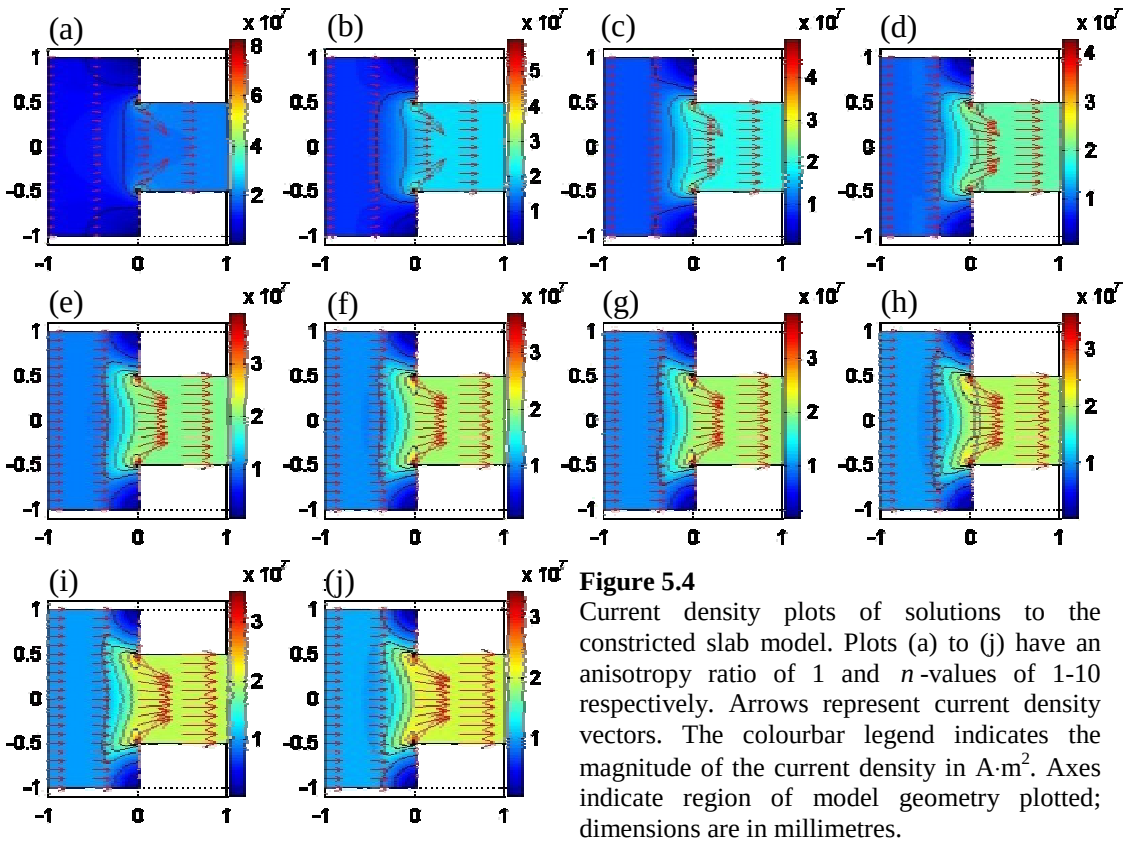

Figure 5.4
Current density plots of solutions to the constricted slab model. Plots (a) to (j) have an anisotropy ratio of 1 and n-values of 1-10 respectively. Arrows represent current density vectors. The colourbar legend indicates the magnitude of the current density in A·m^2. Axes indicate region of model geometry plotted; dimensions are in millimetres.

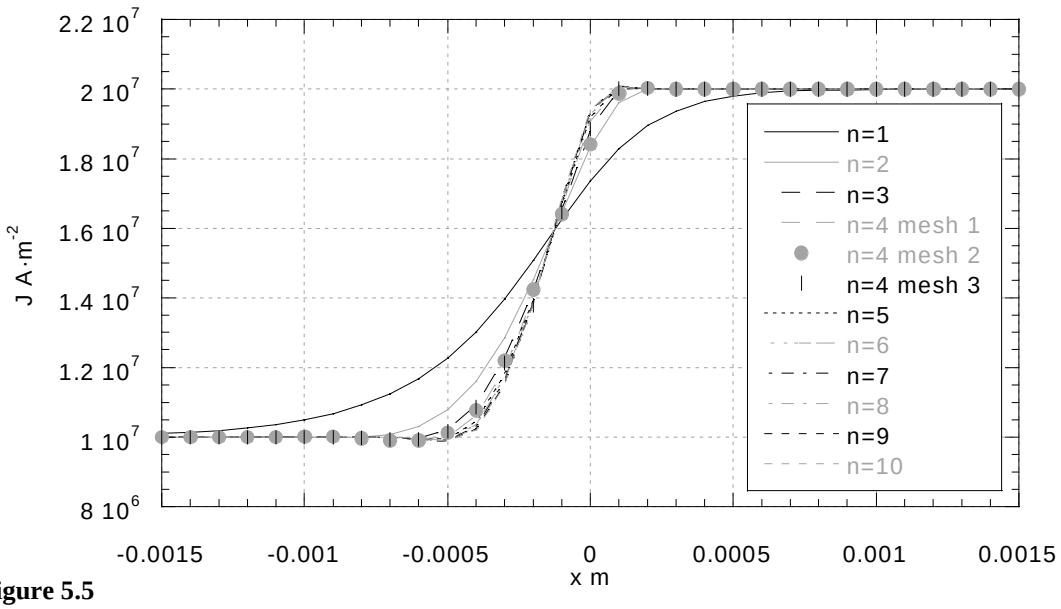

Figure 5.5
Current density values along midline of isotropic constricted slab model, with n =5.

density value was observed (see figure 5.5). The J values for the three different meshes had a maximum percentage standard deviation from the mean of 1.8 %. Error in such line plots is introduced by interpolation from local nodes to specified points along the line. However, the effect of meshing upon the final solution cannot be discounted as a possible further cause of the observed error. It must be noted however that this effect occurs over a length of 8×10^{-4} m. An order of magnitude larger than the side dimensions of the mesh triangles in this region. It is interesting to note that the curves pass through a locus at a position of 1.28×10^{-4} m. As stated above, the principal aim of this model is model validation, which ignores edge effects at the constriction. The physical extent of this effect is small compared to the entire geometry and as such the nature of the current density distribution near the constriction can only be considered as a second order effect.

5.3.2 The anisotropic constricted slab model

The behaviour of current flow in the constricted slab geometry in the anisotropic regime has been explored. All the solutions in the range of n-values $1-8$ and anisotropy values 5, 10, 15, 20 have been calculated; the applied current condition described in section 5.2.1 was used. Contour plots of current density magnitude in the constricted slab geometry (see figures 5.6 and 5.7) show the effects of increasing anisotropy ratio and n-value respectively. Again, current crowding occurs at the inner corners of the constriction, with the maximal value of J at the corner decreasing with increasing n-value and anisotropy ratio.

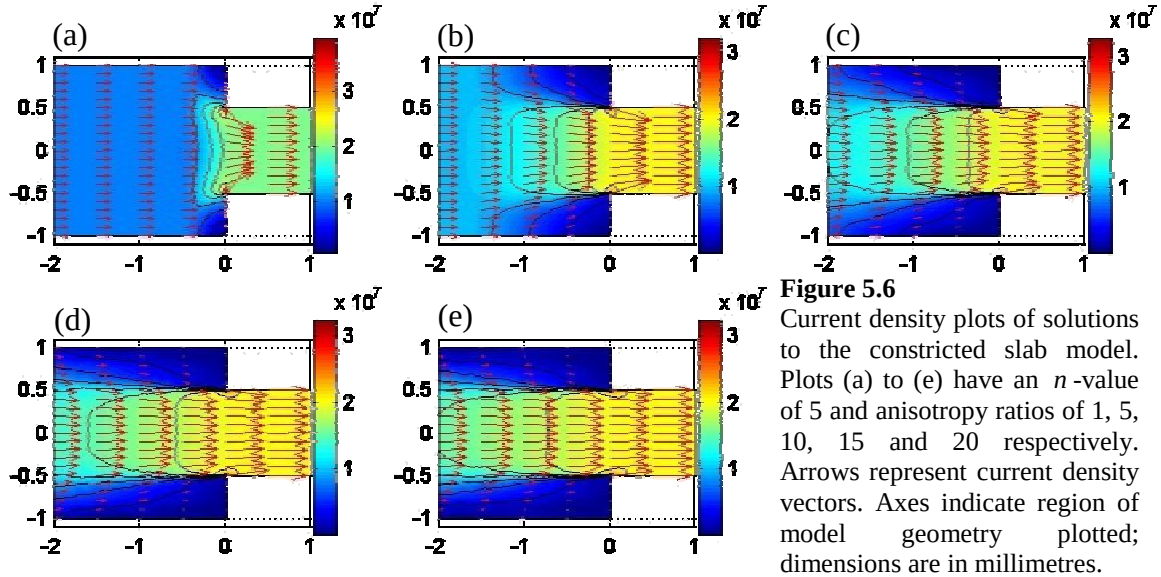

Figure 5.6
Current density plots of solutions to the constricted slab model. Plots (a) to (e) have an n-value of 5 and anisotropy ratios of 1, 5, 10, 15 and 20 respectively. Arrows represent current density vectors. Axes indicate region of model geometry plotted; dimensions are in millimetres.

5.3.3 Discussion of the current flow in nonlinear conductive media

The electric field distribution in a nonlinear electrically conductive medium will always adjust so as to minimise power loss, subject to the independent constraints of the external source; i.e. minimisation cannot be accomplished by the trivial zero current condition. This results in a redistribution of current density. However, in nonlinear media this redistribution must also minimise power loss with respect to the current dependent resistivity of the media. For a nonlinear media with power law EJ characteristic, increasing local current density leads to a direct increase in local power loss and an increase in local resistivity value, which adds a further nonlinear increase in local power loss.

It is suggested that this current dependent nonlinear local resistivity minimises current crowding and the formation of high current density regions in favour of a more even distribution of current, which in accordance with current conservation, is over a larger region. That is, a larger region with larger mean value of local resistivity is favoured instead of a smaller high current density region with exponentially increasing local resistivity value. In both linear and nonlinear regimes, the region over which the current density distribution is non-uniform is larger in the anisotropic case than the isotropic case. This can be explained with reference to equations (4.9a) and (4.9b). In the isotropic case the prefactors of equations (4.9a) and (4.9b) are identical for all powers of n, whereas in the anisotropic regime the nonlinear resistivity prefactor is higher for components of J_y, exponentially increasing with n. Therefore regions with $J > J_c$ possess larger resistivities

in the anisotropic regime than the isotropic regime. As discussed previously, anisotropy introduces a proportionally larger dependence on the components of the local current density and therefore an increased spreading of current across the width of a components current path. This is exhibited by the larger longitudinal extent of the region of non-uniform current (compare figure 5.6, plots b-h and figure 5.7, plots b-h). Examination of the value of the current density magnitude along the midline reveals that the region of non-uniform current flow increases in size with increasing anisotropy (see figure 5.8, compare the nonlinear solutions of plots a and b) consistent with the spreading of current away from the corners of the constriction where most current crowding occurs.

5.3.4 A linear approximation of the nonlinear constricted slab model

A linear simplification of the nonlinear model was constructed by replacing the local nonlinear resistivity function with single resistivity values, for each of the adjoining slabs of the constricted geometry. The resistivity of each slab was determined from the EJ characteristic of the nonlinear model, approximated using the macroscopic average current density. The macroscopic average, $J^m = I_{app} / A$, was derived from the applied current value and the cross sectional area, A, of the model perpendicular to the direction of current flow. Comparison of J along the midline for the linear and nonlinear regimes and linear approximation (see figure 5.8) reveals that the linear approximation agrees well with the nonlinear model near the constriction in both the isotropic and anisotropic cases. The linear, and linear approximation agree well further from the constriction, neither agreeing with the nonlinear model. In the isotropic case the current density distributions (compare figure 5.4, plot a and figure 5.4, plots b-j) suggest that this disagreement is due to the increasingly convex curvature of the current density distribution about the midline in nonlinear models.

5.3.5 Discussion necking and cracks in bulk HTS

Current transport in bulk superconductors is determined principally by pinning and the microstructure of the superconductor. Defects in the microstructure, such as cracks, high-angle grain boundaries, variations in stoichiometry and large aggregations of second phase particles, can hinder the current transport. Necking of the superconductor, cracks

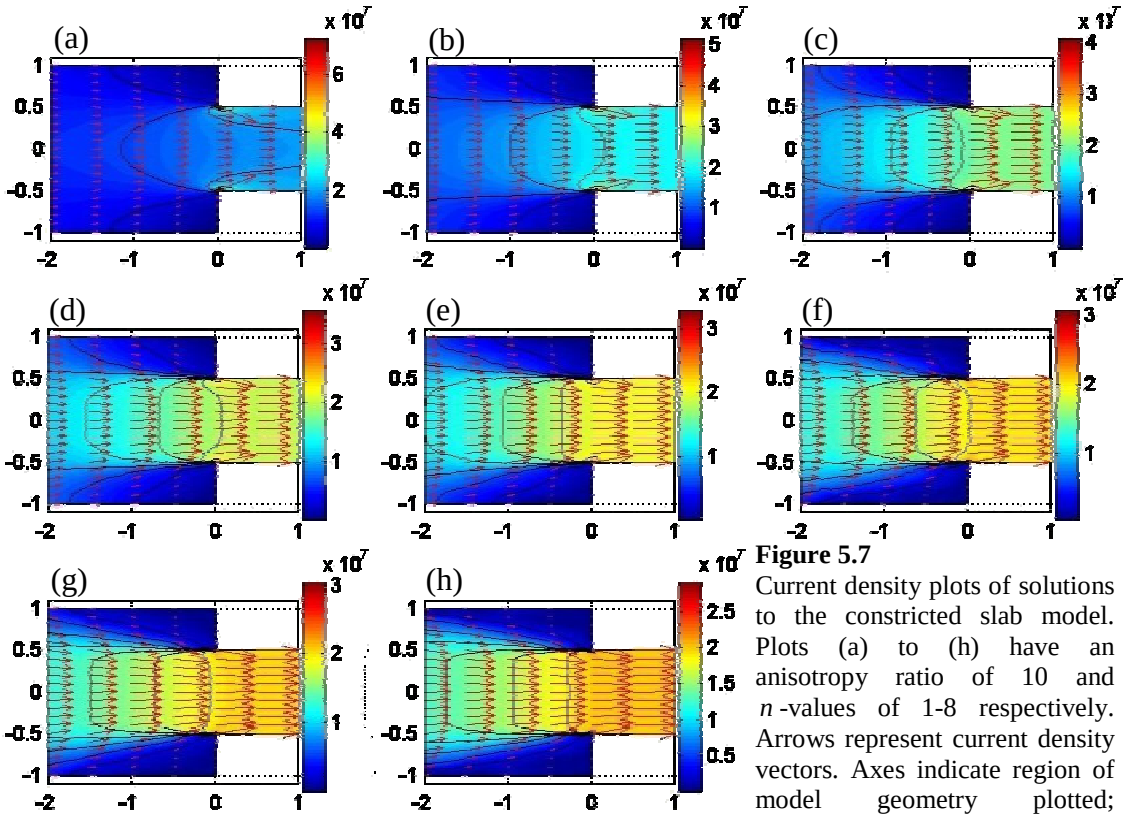

Figure 5.7
Current density plots of solutions to the constricted slab model. Plots (a) to (h) have an anisotropy ratio of 10 and n-values of 1-8 respectively. Arrows represent current density vectors. Axes indicate region of model geometry plotted; dimensions are in millimetres.

and isolated regions of non-superconducting material all affect macroscopic current flow in a similar way, in that they cause an abrupt narrowing of the cross section available for current transport in the superconductor. As such, they will be the focus of the discussion in this section with reference to the constricted slab model.

Formation of these defects can occur for a number of reasons. During processing the intrinsic brittleness of the superconductor powder and any mismatch in the mechanical properties between any supporting material, in the case of dip coated conductors, or sheathing, in the case of PIT conductors, often causes necking or cracking of the conductor. Short binder burn off stages in the processing of binder systems, such as CRT, may also result in cracking or inclusions formed by trapped gas bubbles, which also form in short duration partial melt stages[4]. Poorly conducting or non-conducting regions may be present in the microstructure due to the incongruent decomposition of the partial melt into second phase precipitates. The mechanical deformation techniques employed in the production of PIT tapes can introduce cracks, either parallel or perpendicular to the tape width, dependent upon whether rolling or pressing of tapes is performed. It is suggested that the generally lower J_c of rolled tapes is due to cracks perpendicular to current flow blocking the supercurrent[6].

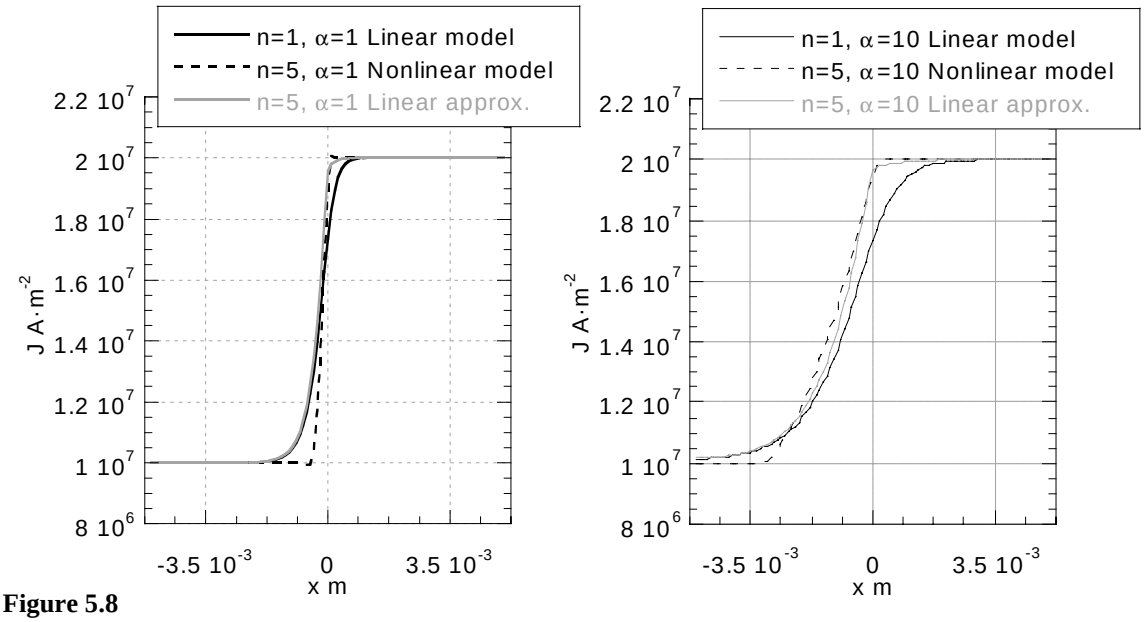

Figure 5.8
Current density values along midline of constricted slab model, for α =1 in nonlinear regime with n =1,5 and linear approximation with n =5 (a) and for α =10 in nonlinear regime with n =1,5 and linear approximation with n =5.

In addition to optimising the above parameters other methods have been used to eliminate defects, or reduce their influence on current flow. These include the addition of silver powder to increase homogeneity of the partial melt[4] or to form thin ribbons in PIT tapes[5] and thereby improve the deformability and texturing of the superconductor. Various methods have been employed to characterise the effect of superconductor inhomogeneity on the transport and magnetic properties of superconductors. These include local hall probe magnetometry[7,8], magneto-optical imaging[9] and resistive four probe measurements[10].

A qualitative understanding of the influence of a constriction in the superconducting volume of a conductor can be derived from the constricted slab geometry model, if one assumes that defects such as necking, cracks and inclusions can be approximated as a step-like narrowing of the immediate superconductor cross section. For qualitative analysis the physical scale of the model is unimportant. However it must be mentioned that in superconductor-metal composites (e.g. PIT and dip-coated conductors) the normal metal can shunt current past low J_c regions unlike the constricted slab model. The nonlinear model results indicate that the influence of a narrowing in the cross section available for current flow has a long-range effect on the current distribution outside the constriction compared to that of linear numerical and perhaps conceptual models. This indicates that uniform current flow is more readily perturbed in nonlinear media. The effect is most pronounced when the EJ characteristic is highly nonlinear, as is the case

for large α and n-value. Current does not crowd as closely and current fills the volume of the superconductor more evenly around and especially through the region of constriction, mitigating regions of high current density.

The constricted slab model solutions also provide insight into the commonly used experimental technique of necking in four point resistive measurements, where a region of a superconducting sample is polished to a fraction of its original cross section. It is assumed that this narrowed section allows for more uniform current flow and therefore the determination of the macroscopic current density in this region is a better approximation of the current density in the material. The results of the model imply that this is a better approximation in a superconductor than in normal metal conductors as current distributes more evenly in the constricted region of the nonlinear model.

5.4 The linear slab model in the transient regime: An analytical comparison

For the purposes of validation of the program in the transient regime, the numerical solution was compared against the analytical solution of a linear problem. To this end, the solutions of a 1D flux diffusion equation

$$\frac{\delta^2 u}{\delta x^2} = \frac{1}{g}\frac{\delta u}{\delta t} \qquad \begin{aligned} u(0,t) &= u_0 \quad t \geq 0 \\ u(w,t) &= 0 \quad t \geq 0 \\ u(x,0) &= 0 \quad 0 \leq x \leq w \end{aligned} \qquad (14.1)$$

where $w = 1\times10^{-3}$ m, $u_0 = 10\times10^{3}$ A·m^{-1} and $g = 1\times10^{-11}/\mu_0$ Ω·m^2·H^{-1}, were examined. This partial differential equation and set of boundary conditions has the following exact analytical solution[11]

$$u(x,t) = \sum_{r=1}^{\infty} B_r e^{-r^2\pi^2 gt/w^2} \sin\left(\frac{r\pi x}{w}\right) \quad \text{where } B_r = \frac{2u_0}{r\pi}. \qquad (14.2)$$

Approximate solutions of this analytical expression were calculated for $r = 1,\ldots,400$. A transient FE solution to equation (9.1) with the prescribed parameters was calculated as the solution along a line in a 2D slab geometry model. Dirichlet boundary conditions were applied along the long edges of the slab and homogeneous Neumann conditions along the other two sides, as schematically shown in figure 5.9. The starting solution for the FE transient analysis was zero throughout the xy plane of the geometry, in accordance with the third boundary condition of equation (9.2). As figure 5.10 indicates the solution is

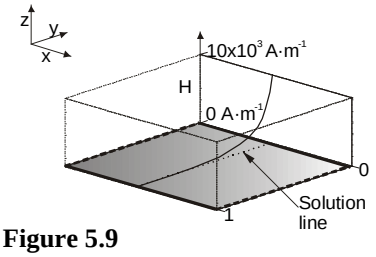

Figure 5.9
Schematic of the geometry of the flux diffusion model and applied boundary conditions. Solid bold lines indicate Dirichlet boundary conditions and homogeneous Neumann boundary conditions are indicated by dashed bold lines. External field magnitude represented by z-axis. Dimensions are in millimetres.

close to the steady state solution after the time interval 0.025 s. Little disparity was found between the FE solution and the approximation of the analytical expression throughout the 0-0.025 s time interval. It was also found that the numerical solutions decrease exponentially to base e with time t, in agreement with the analytical form[11]. The approximation of the analytical solution was found not to differ in the 15th decimal place by comparison of solutions employing $r = 1,\ldots,300$, $r = 1,\ldots,400$ and $r = 1,\ldots,600$. Indicating that the maximum percentage field difference of 6 % between the numerical solutions, plotted in figure 5.10, and the approximated analytical solutions is predominantly an error in the numerical solution (see subplot of figure 5.10). This is probably an interpolation error of the type discussed in section 5.3.1.

5.5 The nonlinear slab model in the transient regime: An analytical comparison

Experimental evidence for a nonlogarithmic time dependence of magnetisation relaxation in HTS suggests that some superconductors possess a nonlinear dependence of the pinning potential on current. Approximate and exact analytical solutions of the magnetisation

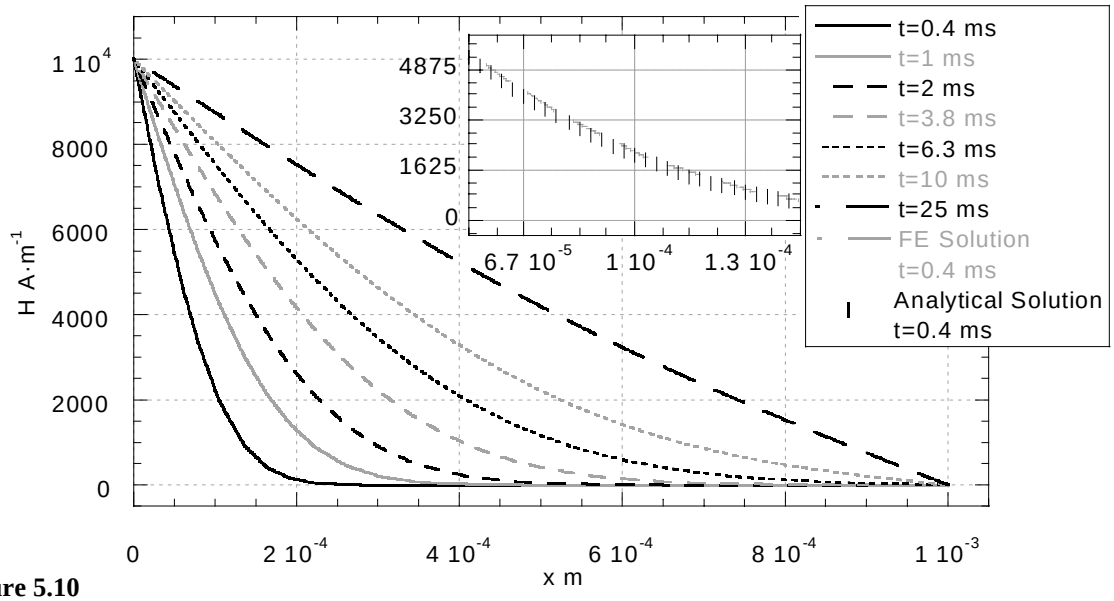

Figure 5.10
Profiles of flux penetration into slab geometry with linear diffusivity term, calculated using FE model. Subplot shows difference between FE and analytical solutions.

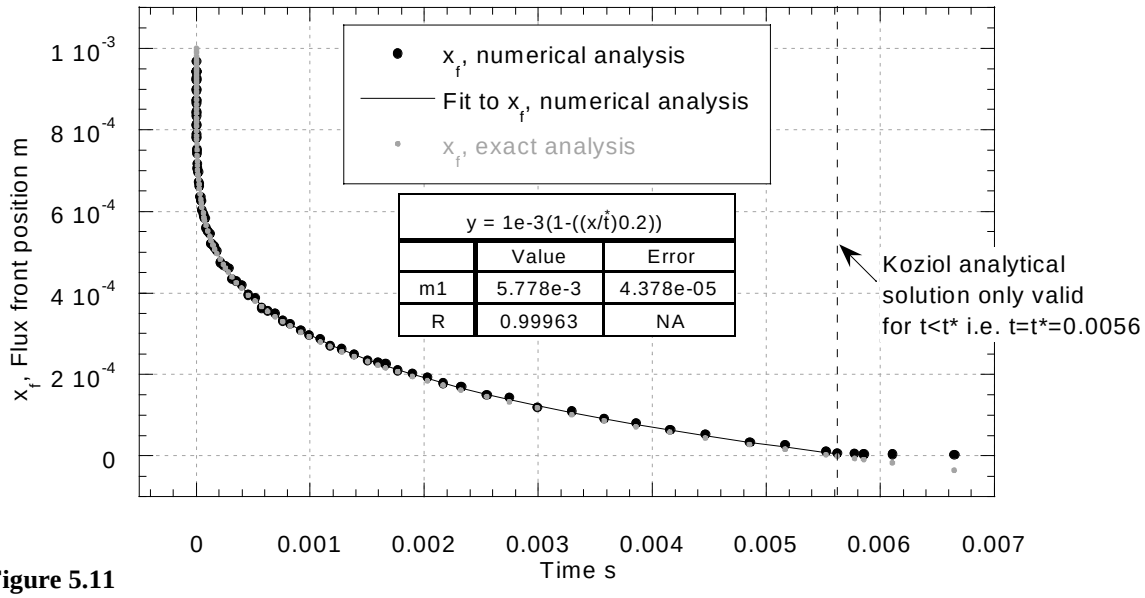

Figure 5.11
Comparison of the exact solution and the FE numerical solution.

relaxation involving a flux pinning potential that depends logarithmically on current have been formulated from models of nonlinear diffusion[12,13], and some agreement with experiment found[14].

For the further validation of the solution technique in the nonlinear regime, an exact solution of a nonlinear diffusion process with a power law electrodynamic characteristic[13] was compared to a FE solution with identical physical parameters. The time evolution of the position of the flux front, x_f, is given by the exact relation

$$x_f = w\left(1-\left(t/t^*\right)\right)^{1/k+2} \tag{5.3}$$

where $$t^* = \tau_0 \frac{k}{2(k+1)} \frac{1}{(k+2)} \left[\frac{\Gamma\left(1/k+1\right)\Gamma\left(3/2\right)}{\Gamma\left(1/k+3/2\right)} \frac{\beta_0}{H_0} \right]^k \left(\frac{w}{x_0} \right)^{k+2} . \tag{5.4}$$

and

$x_0 = c/(4\pi\sigma_0)$, $\tau_0 = 1/(4\pi\sigma_0)$, $\beta_0 = E_0$, $k = n-1$ and w is the sample width. The geometry and placement of the boundary conditions is identical to that of the model of section 5.4.

The time evolution of the position of the flux front across a lead of width 1×10^{-3} m is compared for isotropic resistivity deduced from an EJ curve with $n = 4$, $\sigma_0 = 1\times10^{11}$ $\Omega^{-1}\cdot m^{-1}$ and $E_0 = 1\times10^{-4}$ $V\cdot m^{-1}$. Using these parameters the exact calculated value of t^*

using equation (5.4) is 5.612×10^{-3} s. I gratefully acknowledge the assistance A. M. Campbell in deriving a dimensionally correct value of t^* from equation (5.4)

The numerically calculated flux profile is a set of points along a line interpolated from the values of the solution at the nodes of the mesh. The position of the flux front is taken to be at the interpolated point that has the closest value to 25 $A{\cdot}m^{-1}$ (0.25 % of that of the boundary value). Figure 5.11 plots a comparison of the numerically calculated flux front evolution and the exact solution of equation (5.3). The solutions are almost exactly the same and both follow the same functional dependence of equation (5.4). The exact solution is only valid for $t < t^*$ ($t^* = 5.612\times10^{-3}$ s), and as figure 5.11 shows the fit is poor beyond $t = 5.612\times10^{-3}$ s, where the analytical solution is invalid, demonstrating further agreement between the predictions of the exact and numerical solutions. Note that the numerical model provides a solution outside of the valid range of the exact solution. A single parameter Levenberg-Marquardt regressive curve fit of the numerically derived value of $x_f(t)$ over the valid time range $t = 0 - 5.612\times10^{-3}$ s is also shown in figure 5.11. The functional form of equation 5.4 was used for the fit and calculates $t^* = 5.778\times10^{-3}$ s, which compares favourably to the exact calculated value.

Whereas numerical calculations of nonlinear flux diffusion in slab geometries exist in the literature[15,16] this is the first solution employing the Galerkin FE method. This is also further confirmation of the steady state solution, as the transient solution at a single time point is the solution of the steady state equation with a source term, (see section 4.2); the source term being represented by the value of the time derivative at that time point.

5.6 The constricted slab model: A comparison of the transient and steady state

The solution of a transient model approaches the steady state solution with increasing time. Therefore, after a sufficiently long time interval the transient solution should be similar to the steady state solution for the same system. For further validation of the methods employed to generate solutions in the nonlinear regime, comparison of the steady state solution (which has been verified against intuitive models) and the analytically verified transient solution has been made. The model compared is the constricted slab model with $n = 5$ in both the isotropic case ($\alpha = 1$) and anisotropic case ($\alpha = 5$).

The transient solution at a time $t = 0.1$ s was found to be sufficiently close to the steady state solution for comparison. The same mesh of 180 nodes was used for all the solutions enabling direct comparison of the solution values at the nodes. The maximum percentage difference between the values at the nodes for the steady state and transient ($t = 0.1$ s) solutions was 0.03 % and 0.02 % (see table 5.1), for the isotropic and anisotropic cases respectively. This indicates good consistency between the steady state and transient numerical models. As table 5.1 shows the anisotropic transient solution requires more time steps. This is because the anisotropic solution contains higher resistivity components, which introduce faster flux fronts into the solution; in order to describe accurately the flux fronts, smaller time steps are needed. However because of the presence of flux fronts along both the x and y axes directions, lower resistivity components are also present so the solution does not near the steady state any more rapidly. Whereas 180 nodes are adequate for the purpose of validation, this number of nodes does not provide sufficient spatial resolution for comparison to real systems. Unfortunately, transient models employing fine meshes take a prohibitive amount of time to compute on desktop personal computers and so are not dealt with any further in this work.

Table 5.1 *Comparison of transient and steady state solutions.*

	Maximum percentage difference (%) at nodes	N^o of time steps in transient solution	N^o of nodes in transient and steady state comparison	N^o of nodes in steady state solution
Isotropic ($\alpha = 1$)	0.03	11587	180	2687
Anisotropic ($\alpha = 5$)	0.02	42933	180	2739

5.7 Summary

The validity of the FE technique and computer implementation has been verified by the comparison of results with intuitive and analytical models in the steady state and transient regimes for both isotropic and anisotropic models. For further consistency, agreement between the steady state and a transient model in the long time limit for the isotropic and anisotropic cases has also been demonstrated. It has been shown that current flow in nonlinear media limits current crowding and that this results in a spreading of current over a greater region of the conductor than in linear media. Analogy has been drawn between the constricted slab geometry and macroscopic defects that form permanent barriers to current flow in superconductors. This suggests that such defects have a long-range effect

on the current distribution outside the constriction, which increases with increasing n-value and anisotropy ratio.

5.8 References

1 D. N. P. Murthy, N. W. Page, and E. Y. Rodin, *Mathematical modelling: a tool for problem solving in engineering, physical, biological and social sciences*, Vol. 20 (Pergamon, Oxford, 1990).

2 B. A. Finlayson, *The method of weighted residuals and variational principles*, Vol. 87 (Academic Press, 1972).

3 M. H. Protter and H. Weinberger, *Maximum Principles in Differential Equations* (Prentice-Hall, Englewood Cliffs, NJ, 1967).

4 D. R. Watson, MPhil Thesis, Cambridge, 1996.

5 R. Zhou, W. L. Hults, J. F. Bingert, J. Y. Coulter, E. J. Peterson, and J. L. Smith, Physica C **249,** 166-170 (1995).

6 Q. Li, K. Brodersen, H. A. Hjuler, and T. Freltoft, Physica C **217,** 360-366 (1993).

7 P. Kottman, M. Polak, J. Pitel, S. Buchta, L. Danielik, F. Hanic, and G. Plesch, Superconductor Science & Technology **7,** 67-71 (1994).

8 M. Lahtinen, J. Paasi, J. Sarkaniemi, Z. H. Han, and T. Freltoft, Physica C (1995).

9 D. Larbalestier, X. Y. Cai, H. Edelman, M. B. Field, Y. Feng, J. Parrell, A. Pashitski, and A. Polyanskii, Jom-Journal Of the Minerals Metals & Materials Society **46,** 20-22 (1994).

10 J. R. Cave, D. W. A. Willen, R. Nadi, D. Cameron, and W. Zhu, Ieee Transactions On Applied Superconductivity **5,** 1294-1297 (1995).

11 G. Stephenson, *Mathematical methods for science students*, 2nd ed. (Longman, Singapore, 1992).

12 V. M. Vinokur, M. V. Feigelman, and V. B. Geshkenbein, Physical Review Letters **67,** 915-918 (1991).

13 Z. Koziol and P. F. Dechatel, Ieee Transactions On Magnetics **30,** 1169-1171 (1994).

14 Z. Koziol, P. F. Dechatel, J. J. M. Franse, Z. Tarnawski, and A. A. Menovsky, Physica C **212,** 133-141 (1993).

15 C. J. Vanderbeek, G. J. Nieuwenhuys, P. H. Kes, H. G. Schnack, and R. Griessen, Physica C **197,** 320-336 (1992).

16 Z. Koziol and R. A. Dunlap, Journal Of Applied Physics **79,** 4679-4681 (1996).

CHAPTER 6

Current transfer on the macroscopic scale: Current contacts

6.1 Introduction

Many applications of bulk HTSs in power engineering systems require high quality current contacts between normal metal and HTS components for ready integration into power systems based on normal metal conductors. Such contacts must have a low and uniform effective contact resistivity to avoid increased local power dissipation and thereby localised thermal quenching at regions of high current transfer or high resistivity. A large contact resistance also results in increased cooling power costs. Research on current contacts to bulk HTS materials has predominantly focused on experimental techniques to reduce the contact interface resistance with values for the yttrium based and bismuth based superconducting systems over the range presented in figure 6.1.

The butt, lap and *in-situ* current contact (see figure 6.2) are the principal geometries used commercially and for research. Whereas the butt contact provides ideal current transfer the structure has low mechanical strength and requires additional mechanical support. The lap contact typically allows for a larger contact interface region and therefore greater mechanical strength, and along with *in-situ* current contacts, provides a mechanism for current sharing between the contact and HTS component. This minimises power loss, particularly at high currents. The contact interface resistivity and mechanical strength of both butt and lap current contacts degrade with thermal cycling[1]. The *in-situ* current contact typically has lower contact resistivity and eliminates the separate steps involved in contact preparation but requires different processing during HTS manufacture.

This chapter describes modelling of current transport in the contact region of *in-situ* current contacts to isotropic and anisotropic HTSs. The numerical solutions of the model compare favourably to the results of experimental studies of the voltage distribution along *in-situ* current contacts to Bi-2212 CRT. The *in-situ* current contact and the general

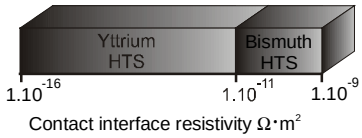

Figure 6.1
Range of current contact interface resistivity values for the yttrium based and bismuth superconducting systems.

current transfer behaviour of *in-situ* currents contact are described in section 6.2. The properties of current contacts are usually investigated at applied currents, I_{app}, lower than the critical current of the superconductor, I_c, and do not analyse the current distribution within the contact[2,3]. These models are described in section 6.3. Power engineering applications, such as fault current limiters often demand maximum operating currents significantly larger than the critical current of the superconducting component. Under these conditions, the superconductor enters a resistive flux flow state which changes the current transfer behaviour of the current contact[4,5]. The nonlinear and anisotropic behaviour of the superconducting component of current contacts operating below and above I_c has been modelled extensively using two different approaches, the results of which are discussed in sections 6.4 and 6.5.

6.2 Current transfer in current contacts

There are two principal contributions to the effective electrical surface resistivity of a current contact, one from the interface resistance and the other from the bulk resistivity of the device material. Current injection across the butt contact to an homogeneous nonlinear material is uniform across the entire contact area and as such the bulk resistivity term and current transport behaviour can be described on both local and global scales solely by the EJ characteristic of the bulk material. In geometries where the direction of current injection is not perpendicular to the contact-device material interface, there is bending of the current path away from the injection direction. This results in current passing across the contact area non-uniformly, becoming increasingly unevenly distributed, as the resistivities of the contacted materials become more dissimilar. Current crowding at the interface nearest the injection point becomes more congested in the extreme case of a superconducting device material contacted to a normal metal.

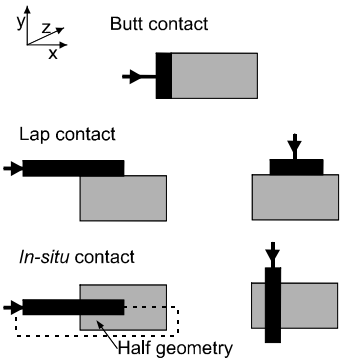

Figure 6.2
Schematic of the butt, lap and *in-situ* current contact geometries relative to the x, y, z co-ordinate frame shown.

The contact interface resistance and the bulk resistivity of the device material both contribute to the effective contact resistivity of a current contact. The usually negligible bulk

resistivity term of the HTS becomes significant on a local scale across the current contact for $J \geq J_c$, introducing a spatially complex current dependent bulk resistivity contribution to the effective contact resistivity. Due to the nonlinear nature of the EJ characteristic, current transfer in contacts to nonlinearly conducting devices is difficult to analyse both analytically and numerically. Further complications arise due to the macroscopic current anisotropy of many bulk HTSs because the principle critical current transfer component across the contact interface, $J_{c,y}$, can be upwards of a factor of 10 less than $J_{c,x}$; such that local current density values below that of the macroscopic average can engender a flux flow condition.

6.3 1D transmission line model of current transfer across a current contact

In 1971, two basic models for contacts to planar devices were developed in the field of semiconductor physics and remain, under various guises in the field of superconductivity, the two principle theoretical descriptions to date. The two models represent two extremes of behaviour, the Kennedy-Murley model[6] solves the electrical conduction equations over the 2D geometry of a semiconductor current contact with zero contact resistance and the Murrmann-Widmann model[7] (TL model) solves a 1D line contact with nonzero contact resistance but zero semiconductor device material thickness. This section describes the TL model. Section 6.4 describes a model that solves the electrical conduction equations of a 2D current contact with nonzero contact resistance and improves upon existing models by calculating current flow in contacts to anisotropic nonlinear media using FD techniques.

Employing the approach of Berger[2] the TL model can be derived for the case of a current contact to a superconducting device. Compare the cross section of the contact and the transmission line section in d.c. operation as illustrated in figure 6.3. The roles of the contact and device material in the Berger derivation have been swapped for the purposes of the lap contact geometry employed in this derivation. The TL contact comparison indicates that the resistivity of the contact metal, ρ_{cm} (ρ_{Ag} and ρ_{Au} for silver and gold contacts respectively), corresponds to the series resistance per unit length of the

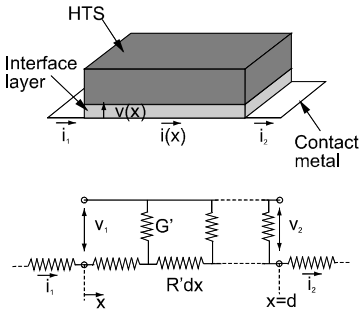

Figure 6.3
Schematic of metal-HTS contact and transmission line circuit diagram.

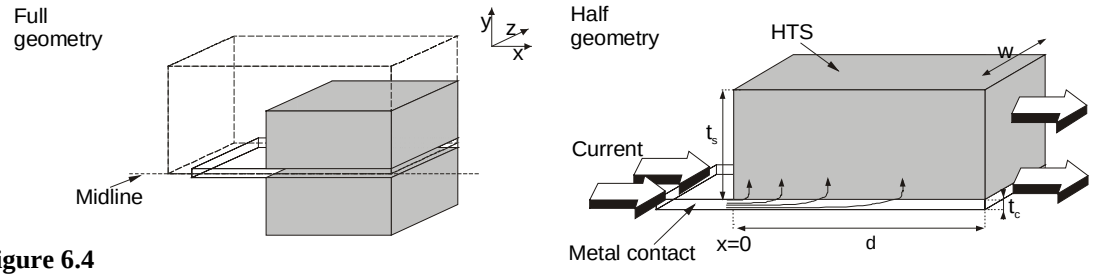

Figure 6.4
Schematic describing *in-situ* contact geometry, indicating half geometry modelled and point of initial interface contact x =0.

transmission line, R', and the interface resistivity, ρ_i, is the counterpart of the parallel shunt line conductance per unit length G'. For unit width, w, and thickness, t, R' and G'equate with ρ_{cm} and ρ_i

$$R' = \frac{\rho_{cm}}{wt} \tag{20.1}$$

and

$$G' = \frac{w}{\rho_i}. \tag{20.2}$$

The line equations, equations (20.3) and (20.4), describe the current and voltage distribution along the contact of figure 6.3

$$v(x) = v_1 \cosh \alpha_c x - i_1 Z \sinh \alpha_c x \tag{20.3}$$

$$i(x) = i_1 \cosh \alpha_c x - v_1 / Z \sinh \alpha_c x \tag{20.4}$$

with characteristic d.c. impedance

$$Z = \left(\frac{R'}{G'} \right)^{\frac{1}{2}} = \frac{1}{w} \left(\frac{\rho_{cm} \rho_i}{t} \right)^{\frac{1}{2}} \tag{20.5}$$

and propagation constant

$$\alpha_c = (R'G')^{\frac{1}{2}} = \left(\frac{\rho_{cm}}{t \rho_i} \right)^{\frac{1}{2}}. \tag{20.6}$$

In the case of the terminal contact, $i_1 \neq 0$ and $i_2 = 0$ (see figure 6.3). Given the condition $i_2 = 0$, combining equations (9.1) and (9.2), the application of a hyperbolic trigonometric identity gives

$$v(x) = i_1 Z \frac{\cosh\left[\alpha d (1 - x/d)\right]}{\sinh \alpha_c d} \tag{20.7}$$

where d is the contact length at which point $i_2 = 0$. This derivation treats the current contact within a 1D limit, in that it assumes that equipotential lines extend across the contact width perpendicular to the device edge, and that the contact metal has zero

thickness. This terminal contact model equivalently describes current transfer behaviour in the lateral half geometry of the *in-situ* contact (see figure 6.4) if the current transfer in the *in-situ* contact is assumed negligible at $x = d$. A characteristic current transfer length, l_t, can be defined as the reciprocal of the propagation constant, α_c. The contact resistance R_c (units of Ω) is simply related to the total voltage drop ΔV along the contact by $R_c = \Delta V / i_1$. Substitution of $x = d$ in equation (6.7) gives ΔV and hence

$$R_c = Z \operatorname{cosech}(d/l_t). \tag{6.8}$$

The power dissipation, $P = V_0 i_1$, can be expressed as

$$P = i_1^2 Z \operatorname{cosech}(d/l_t). \tag{6.9}$$

In the limit $d << l_t$, $\operatorname{cosech}(d/l_t) \approx (d/l_t)^{-1}$ and therefore, $R_c = 1/(G'd)$ and $P \approx i_1^2/(G'd)$[8]. Thus, relatively short contacts suffer from power dissipation that increases as $1/d$. In the limit $d >> l_t$, $\operatorname{cosech}(d/l_t) \approx 1$ and therefore, $R_c \approx (R'/G')^{1/2}$ which is the characteristic d.c. impedance (equation (6.5)) and $P \approx i_1^2 (R'/G')^{1/2}$[8]. Thus, increasing the contact length neither decreases the resistance nor the power dissipation.

Due to the symmetrical half geometry of the *in-situ* current contact, the effective thickness of the metal contact lead is $t/2$ and width $2w$ compared to a lap geometry contact. In the limit $d >> l_t$ the contact resistance can therefore be written as

$$R_c = \frac{1}{2w}\left(\frac{2\rho_i \rho_{cm}}{t}\right)^{1/2}. \tag{6.10}$$

This model can only be applied in the low applied current regime for which the bulk resistivity of the superconducting component is negligible. A 1D nonlinear model, based upon the TL model, has been developed and replaced the contact interface resistivity, ρ_i, term of equation (6.6) with a contact resistivity that has constant and current dependent resistivity components $\rho_{ni} = \rho_i + \rho(J(x))$ (results not presented).

6.4 2D finite difference model of current transfer across a current contact

The 1D TL model only deals with 1D current flow in current contacts to isotropic Ohmic materials with zero contact metal thickness. For further examination of the 2D current flow in contacts to superconductors a model employing an anisotropic nonlinear conductive device media has been developed. The Kennedy-Murley model investigates

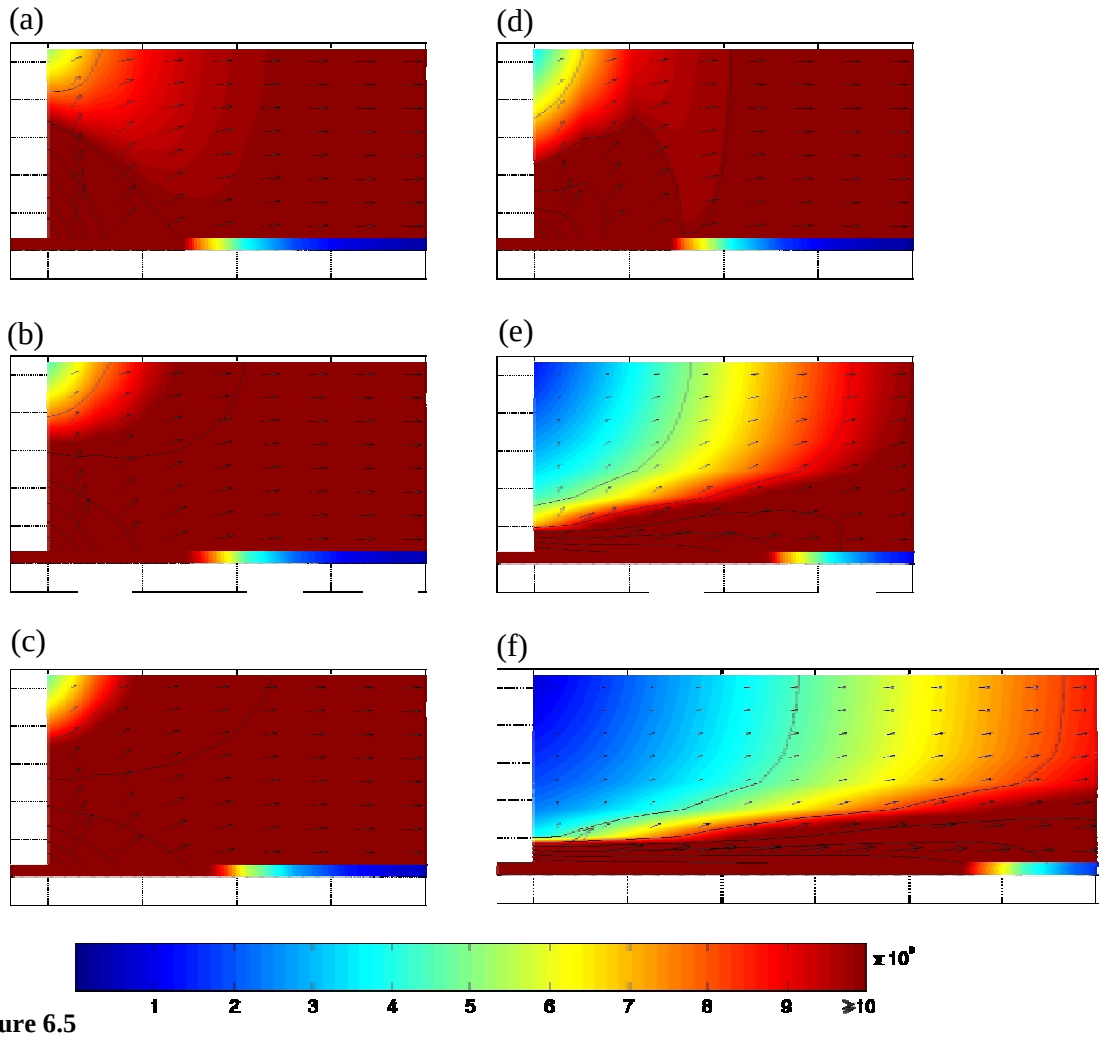

Figure 6.5
Current density distributions (a)-(f) of the Au-HTS *in-situ* contact with applied current equal to the critical current of the device. The current density distributions are derived from FD model solutions. The superconducting region in plots (a)-(c) has an n-value of 1 and anisotropy ratios of 1, 5 and 10 respectively. The superconducting region in plots (d)-(f) has an n-value of 9 and anisotropy ratios of 1, 5 and 10 respectively. The region $x = -0.2 \times 10^{-3}$ to $x = 2 \times 10^{-3}$ m is shown in plots (a)-(e) and the region $x = -0.2 \times 10^{-3}$ to $x = 3 \times 10^{-3}$ m is shown in plot (f). Arrows indicate current density vectors.

the electrical properties of contacts to semiconductor devices using a 2D FD method. In a similar manner to that used by Kennedy and Murley a 2D model using control volumes[9] has been developed to investigate the electrical properties of Au-HTS current contacts[10]. This model replaces the semiconductor EJ characteristic with the power law characteristic described in section 4.3.1. The model also accounts for critical current anisotropy and incorporates a contact interface resistivity boundary condition between the gold and superconducting components.

The numerical solution to the 2D FD model solves a number of electrostatic state variables in the 2D geometry of the *in-situ* contact[4], the geometry of which is shown schematically in figure 6.4. The symmetry of the lateral midline of the contact geometry is used to halve the region over which the solution is calculated. The electrical conduction problem is represented mathematically by the uniformly elliptic harmonic nonlinear Laplace equation and the current continuity equation. The solution of these simultaneous equations is approximated at a number of discrete points (≈ 250) arranged in a rectangular grid over the contact geometry using the FD control volume method. This involves discretising the solution region into a rectangular grid of solution points (nodes), where the local electric potential, resistivity and the x and y axis components of the current density vector are calculated using a set of balance equations. Electrical potential boundary conditions at both ends of the contact induce a current flow in the composite Au-HTS structure subject, in the anisotropic case, to different nonlinear resistivities in the x and y axis directions. Other FD models used solutions of the voltage distribution over the entire contact to fix boundary conditions for models of smaller regions of interest (results not presented). The nonlinearity is a current dependent resistivity of the same functional form as equations (4.9a) and (4.9b). The resulting sets of nonlinear equations are solved by least squares optimisation employing the Levenburg-Marquardt search direction method. A linear solution obtained by direct matrix solution is used as the starting guess for the nonlinear optimisation. The dimensions of the 2D contact and physical parameters describing the material properties of the contact components are detailed in list 6.1. Figure 6.5 compares the current density distribution in the linear and nonlinear models of the *in-situ* current contact for anisotropy ratios of 1, 5 and 10. Figure 6.6 shows plots of the current density

List 6.1 *Physical parameters of the 2D FD model of the in-situ current contact.*

Contact metal resistivity @ 77 K (Au)	1.52×10^{-8} Ω·m
Thickness of contact metal (Full geometry)	62.5×10^{-6} m
Superconducting component n-value range	9
Thickness of superconducting component (Full geometry)	2×10^{-3} m
$J_{c,x}$ of superconducting component using 1×10^{-4} V·m^{-1} criterion	10×10^{6} A·m^{-2}
Critical current of device, I_c	100 A
Critical current anisotropies of superconducting component	1, 5, 10, 20, 30
Notional width of current contact	5×10^{-3} m
Contact interface length	6×10^{-3} m
Contact interface resistance	2.5×10^{-11} Ω·m^2

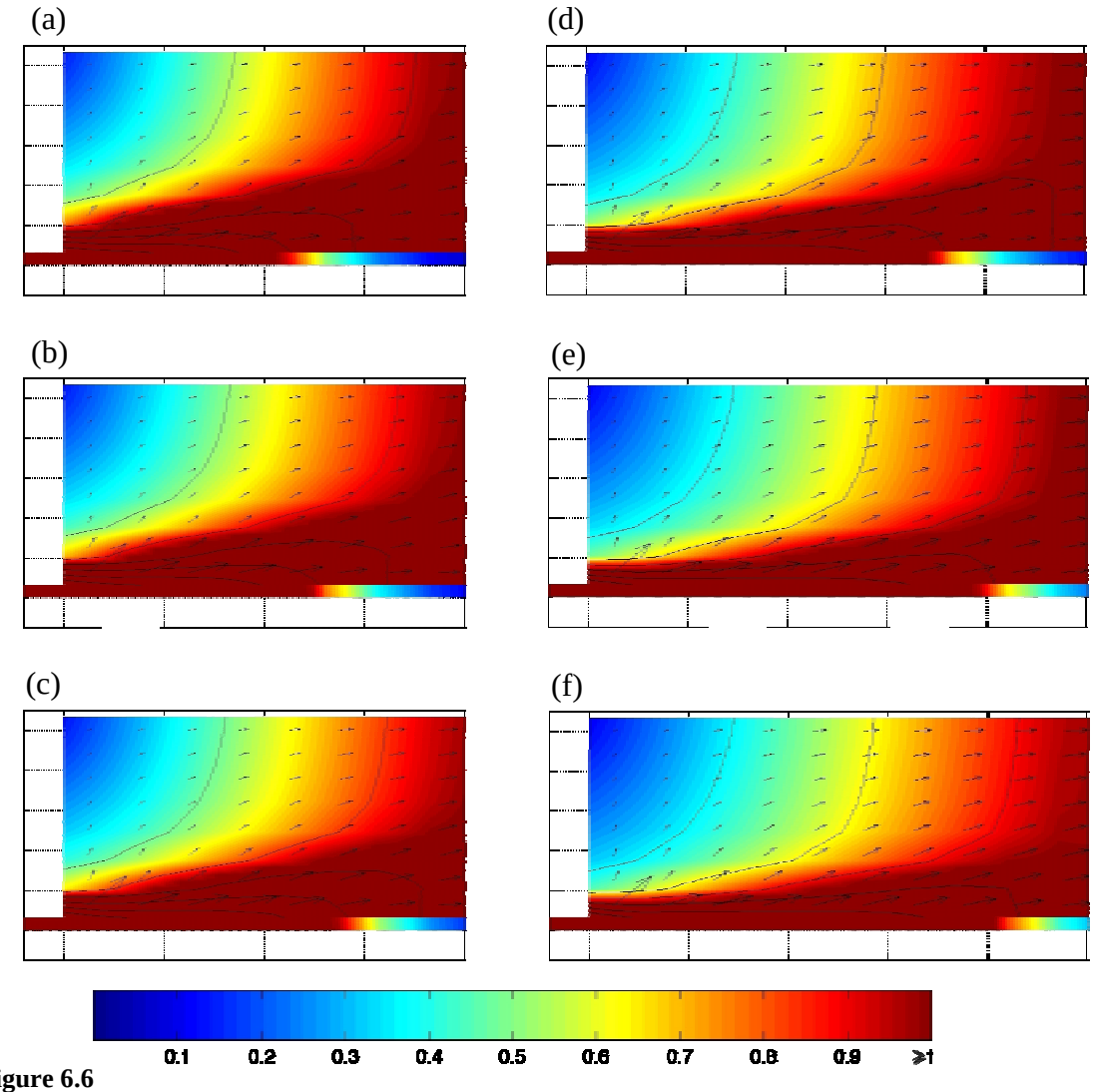

Figure 6.6
Current density distributions (a)-(f) of the Au-HTS *in-situ* contact normalised with respect to the macroscopic current density, $I_{app}/(t_s w)$, for applied currents of $0.9I_{app}$, $1I_{app}$, $1.1I_{app}$, $1.4I_{app}$, $1.5I_{app}$ and $1.6I_{app}$ respectively. The current density distributions are derived from FD model solutions. The superconducting region has an n-value of 9 and anisotropy ratio of 5. The region $x = -0.2\times10^{-3}$ to $x = 2\times10^{-3}$ m is shown in plots (a)-(c) and the region $x = -0.2\times10^{-3}$ to $x = 2.5\times10^{-3}$ m is shown in plots (d)-(f). Arrows indicate current density vectors.

distribution normalised with respect to the macroscopic current density, $I_{app}/(t_s w)$, for different applied current conditions. Normalisation of the current density distribution allows easier examination of the evolution of the distribution with increasing current density and still allows for current density values, below $I_{app}/(t_s w)$ of a particular solution, to be determined, given the value of J_c (see list 6.1). Normalised current density distributions derived from solutions with $n = 1$ possess the same single valued resistivity term for each component and so are identical for every value of I_{app}.

From the point of initial contact between the normal metal and the HTS, $x = 0$, a $2\times10^{-3} - 3\times10^{-3}$ m length of current contact is shown in figures 6.5 and 6.6. The current density distributions described by the plots of figures 6.5 and 6.6 possess good qualitative agreement with FE models of Au-HTS and Ag-HTS *in-situ* current contacts. This qualitative agreement between the two modelling methods based upon different mathematical representations of the underlying physical system further demonstrates the consistency of the modelling approaches employed. The current transfer behaviour of the *in-situ* current contact as described by the physical model of current transport in nonlinear conductive media is described in the next section.

6.5 2D finite element model of current transfer in the current contact region

As mentioned in section 4.2 a FD model of a physical problem cannot be readily adapted to different geometries and structures, and such techniques should only be applied to specific problems. The FD models of the *in-situ* current contact possess, at most, 250 solution points and take 1-4 hours to solve. This section presents the results of a FE model of the *in-situ* current contact that has been developed in order to overcome the inflexibility, lack of spatial resolution in the computed solution, inefficiency and relative inaccuracy of the FD model.

At low applied currents the current transfer across the contact interface is exactly described by the linear TL model (the TL regime). As the applied current value increases the bulk resistivity of the superconductor becomes increasingly significant and the current transfer behaviour deviates from that of the linear TL model (the non-TL regime). For the *in-situ* contacts modelled and experimentally measured, the TL regime typically occurs for $I_{app} < I_c$ and the non-TL regime for applied currents greater than the critical current of the contacted device, $I_{app} \geq I_c$. The applied current that differentiates the TL and non-TL regime is an approximate value. Anisotropy of the bulk superconducting material introduces two critical current density values. In regions of current flow involving both x and y-axis current density components, the value of the applied current below which the TL regime occurs is not simply the critical current value of the bulk superconducting component, which assumes uniform current flow in the x-axis direction, but a value below I_c.

List 6.2 *Physical parameters of the 2D FE model of silver and gold in-situ and lap current contacts.*

Contact metal resistivity @ 77 K (Ag)	0.29×10^{-8} Ω·m
Contact metal resistivity @ 77 K (Au)	1.52×10^{-8} Ω·m
Thickness of contact metal (Full geometry)	62.5×10^{-6} m
Superconducting component n-value range	1-6
Thickness of superconducting component (Full geometry)	1.5×10^{-3} m
$J_{c,x}$ of superconducting component using 1×10^{-4} V·m^{-1} criterion	10×10^{6} A·m^{-2}
Critical current of device, I_c	15×10^{3} A
Critical current anisotropies of superconducting component	1, 3, 5, 10
Notional width of current contact	1 m
Contact interface length	4×10^{-3} m
Contact interface resistance	2.5×10^{-11} Ω·m^2

In the following sections the characteristic current transport behaviour of these two regimes is discussed and compared to experimental measurements of current transfer characteristics in *in-situ* current contacts to HTSs. In addition, the current transfer of lap current contacts has been modelled and is discussed. Gold and silver *in-situ* current contacts and gold lap contacts have been modelled. In a similar manner to that of the FD model, the symmetry of the lateral midline of the current contact is used to halve the size of the solution space. Contact dimensions and other physical parameters describing the material properties of the contact components are detailed in list 6.2.

6.5.1 The *in-situ* current contact in the linear regime

For small applied currents, $I_{app} < I_c$, the transmission line model can be used to describe the voltage distribution along the contact midline, $V(x)$, and agrees well with the experimental determination of the voltage drop along an *in-situ* contact (see figure 6.7). Electrical measurements along a sample were performed by measuring the voltage drop across a series of voltage contacts placed on the *in-situ* contact metal insert.

For small applied currents, the distribution $V(x)$, as calculated by the linear ($n=1$) and nonlinear FE models ($n=5,\ 6$), agrees exactly with the analytical expression (equation (6.7)) describing the voltage drop along the contact midline and therefore agrees with the experimentally determined voltage distribution along the contact midline. An accurate solution cannot be obtained using the numerical models presented in this thesis for contact lengths d greater than 4×10^{-3} m. This is smaller than the typical contact length of Bi-2212 CRT *in-situ* current contacts and so a direct comparison of FE model solutions and the experimental data is not possible. Direct comparison is also not possible due to the different n-value of the EJ characteristic of the experimental sample and FE model. In

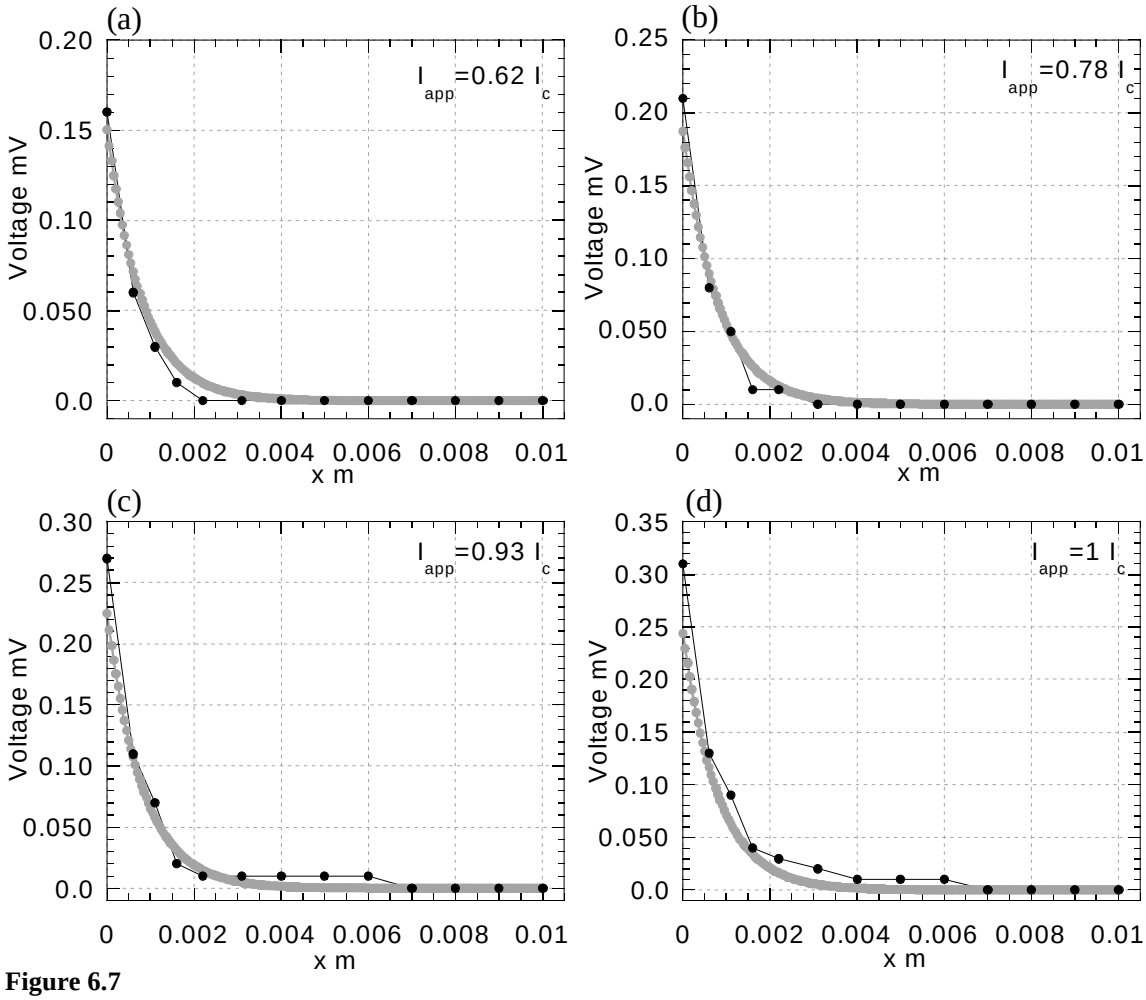

Figure 6.7
Plots of the voltage distribution along the Ag contact metal insert midline for various applied current values. Grey closed circles indicate TL model calculated values of the voltage along the contact midline, using the same contact parameters as those determined by experiment. Black closed circles indicate the experimentally determined voltage along the contact midline of the Ag-HTS *in-situ* current contact. Experimental data courtesy of A. Kuršumovic.

the low current regime the FE model calculated distribution $V(x)$ is independent of α; this is however not the case in the non-TL regime and is discussed in the next section. In this regime the bulk resistivity of the superconductor over the region of initial current transfer even on a local scale is small, 1.2×10^{-14} Ω·m near the point of largest transfer ($I_{app} = 0.25I_c$, $n = 6$, $\alpha = 1$, Ag-HTS contact), and so does not contribute to the current transfer characteristic along the metal contact. The nonlinear FD model calculation of $V(x)$ agrees closely with the analytical expression in the low current regime.

The total voltage difference along the contact midline between $x = 0$ and $x = d$, ΔV, is a useful characteristic parameter for comparison of the *in-situ* contact current transfer behaviour. The experimental value of ΔV was measured as the voltage drop between voltage contacts placed at $x = 0$ and at a point on the bulk superconductor far removed

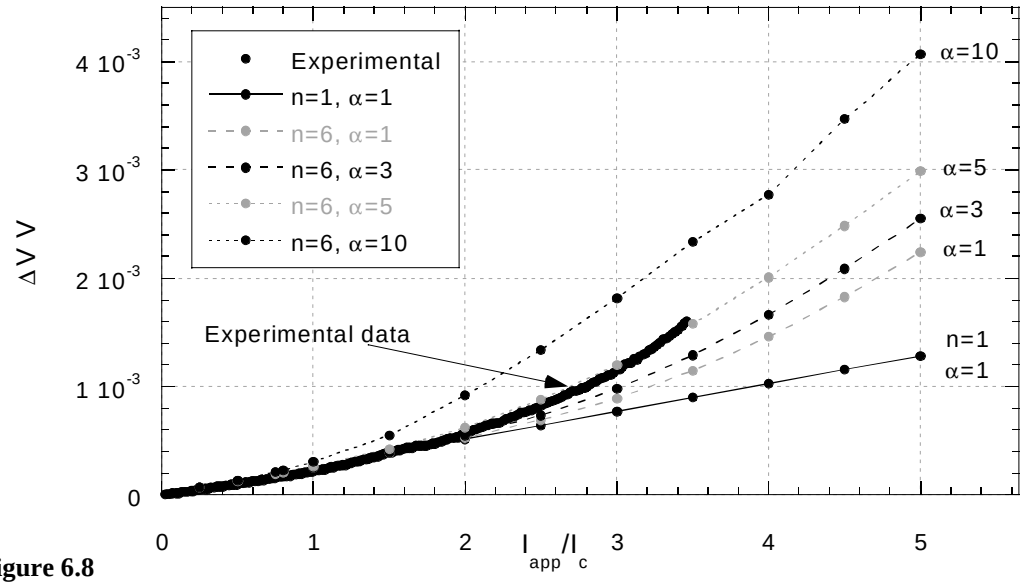

Figure 6.8
Plot of ΔV across the Ag *in-situ* metal contact insert as a function of the applied current normalised with respect to the critical current. Experimental and FE model derived values are presented. The FE model data presents solutions with n-values of 1 and 6 for anisotropy factors of 1, 3, 5 and 10. Experimental data (black closed circles, no line) courtesy of A. Kuršumovic.

from the contact region. The value of ΔV, as derived from the FE solution, was calculated from the electric field distribution using the expression

$$\Delta V = \int_0^d \mathbf{E} \bullet \mathbf{dl} .$$

Plots of ΔV as a function of applied current, normalised with respect to the critical current value, calculated from solutions with $n > 1$, indicate that $\Delta V\left(I_{app}\right)$ has a the linear dependence for values below approximately I_c (see figure 6.8). For solutions with $n = 1$, $\Delta V\left(I_{app}\right)$ has a linear dependence for all values of I_{app} and is the same for α=1, 3, 5, 10. In the TL regime, the FE model and experimental values of $\Delta V\left(I_{app}\right)$ agree exactly (see figure 6.8). The contact resistance is given by the gradient of the linear region of the $\Delta V\left(I_{app}\right)$ curve. Both numerically and experimentally derived values of the gradient agree exactly with the calculated value of 3.7×10^{-6} Ω given by the TL model using equation (6.10). This further demonstrates that the nonlinear FE model correctly reproduces both the experimental and TL model results in the TL regime. For $I_{app} > I_c$, $\Delta V\left(I_{app}\right)$ deviates from linear behaviour (except the $\Delta V\left(I_{app}\right)$ curve derived from the FE solution with $n = 1$) for applied current greater than approximately I_c (see figure 6.8). This is discussed in the following section.

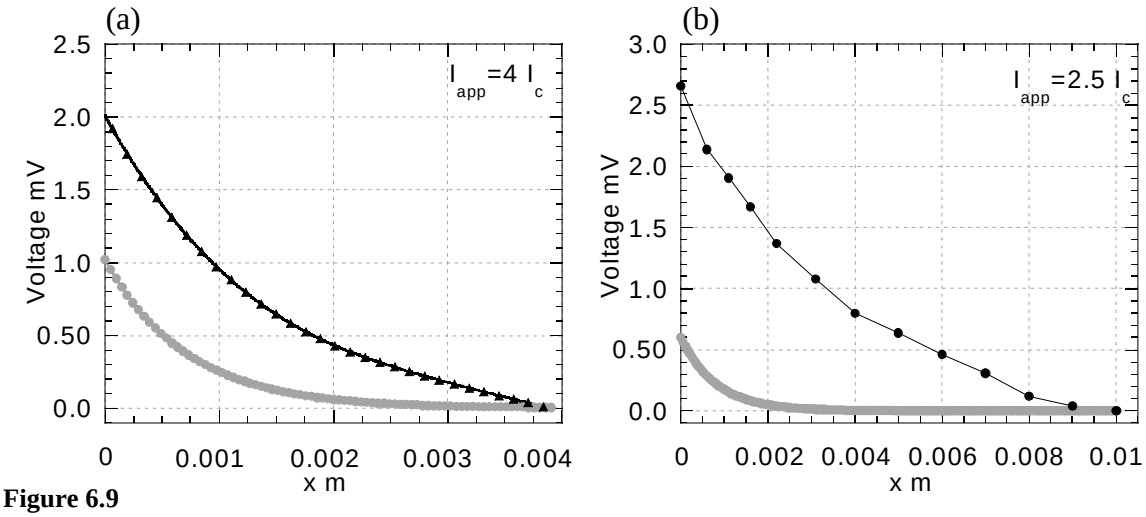

Figure 6.9
Comparison of the voltage distribution along the Ag contact midline, determined from a FE model solution (plot a) and experimentally (plot b), with TL model approximations. Grey closed circles indicate TL model calculated values of the voltage along the contact midline. Black closed circles indicate the experimentally determined voltage along the contact midline of the Ag-HTS *in-situ* current contact. Black closed triangles indicate the FE model calculated values of the voltage distribution along the contact midline for a solution with $n = 6$ and $\alpha = 5$. The experimental data is provided courtesy of A. Kuršumovic.

6.5.2 The *in-situ* current contact in the nonlinear regime

For applied currents, $I_{app} > I_c$, the TL model no longer agrees well with the experimental determination of the voltage distribution along the contact midline, $V(x)$, (see figure 6.9, plot b). The distribution $V(x)$ deviates from the distribution computed by the TL model with increasing applied current. This is most pronounced near $x = 0$, at which point the experimental voltage is greater in value than that calculated by the TL model, (see figures 6.8 and figure 6.9, plot b). At this point, the local resistivity value in the superconducting component is maximum. The current density component J_y across the interface is maximal and J_x is zero. The increasing contribution to the contact resistivity of the bulk component in the experimental sample with increasing applied current leads to an increase at $x = 0$, in the required voltage to accommodate the same constant current condition as applied in the TL model.

Comparison of plots a and b of figure 6.9 indicates that the deviation from $V(x)$ as calculated by the TL model is similar in form for both the FE model and experiment. A larger applied current value is required to generate similar behaviour to that of the experimental $V(x)$ curve due to the lower n-value associated with the FE model EJ characteristic of the superconducting component. The experimental and FE model $V(x)$ curves do not exhibit the characteristic exponential functionality of the TL model,

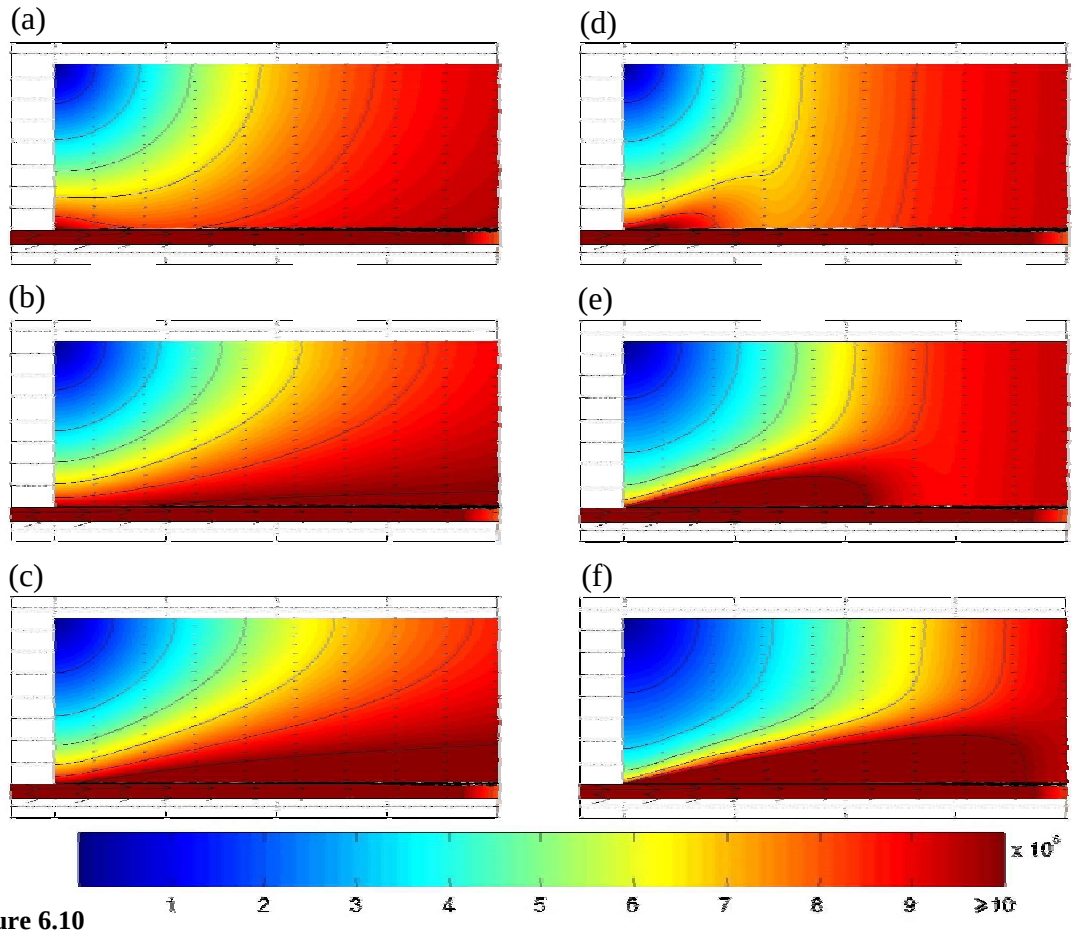

Figure 6.10
Current density distributions (a)-(f) of the Ag-HTS *in-situ* contact with applied current equal to the critical current of the device. The current density distributions are derived from FE model solutions. The superconducting region in plots (a)-(c) has an n-value of 1 and anisotropy ratios of 1, 3 and 5 respectively. The superconducting region in plots (d)-(f) has an n-value of 6 and anisotropy ratios of 1, 3 and 5 respectively. The region $x = -0.2 \times 10^{-3}$ to $x = 2 \times 10^{-3}$ m is shown. Arrows indicate current density vectors.

indicating that the additional current dependent bulk resistivity is not single valued but a complex spatial distribution. This is confirmed by the evolution of the current density distribution with increasing current, (see figure 6.11). On application of increasing applied current values, the length over which most current is transferred to the superconducting component does not increase linearly at high applied currents as prescribed by equation (6.7), but increases nonlinearly at an increased rate. At very high currents, current transfer is more evenly distributed along the whole contact[8].

The current distribution in the HTS component is different for linear models and nonlinear models in the entire current range $I_{app} = 0.25 I_c - 5 I_c$ and for anisotropy ratios 1, 3 and 5 (see figure 6.10, compare plots a-c and d-f). The 'hump-like' high current density region at the contact interface is typical of *in-situ* contact models with nonlinear HTS component (see figures 6.5 and 6.10). Within the superconducting component, the current density

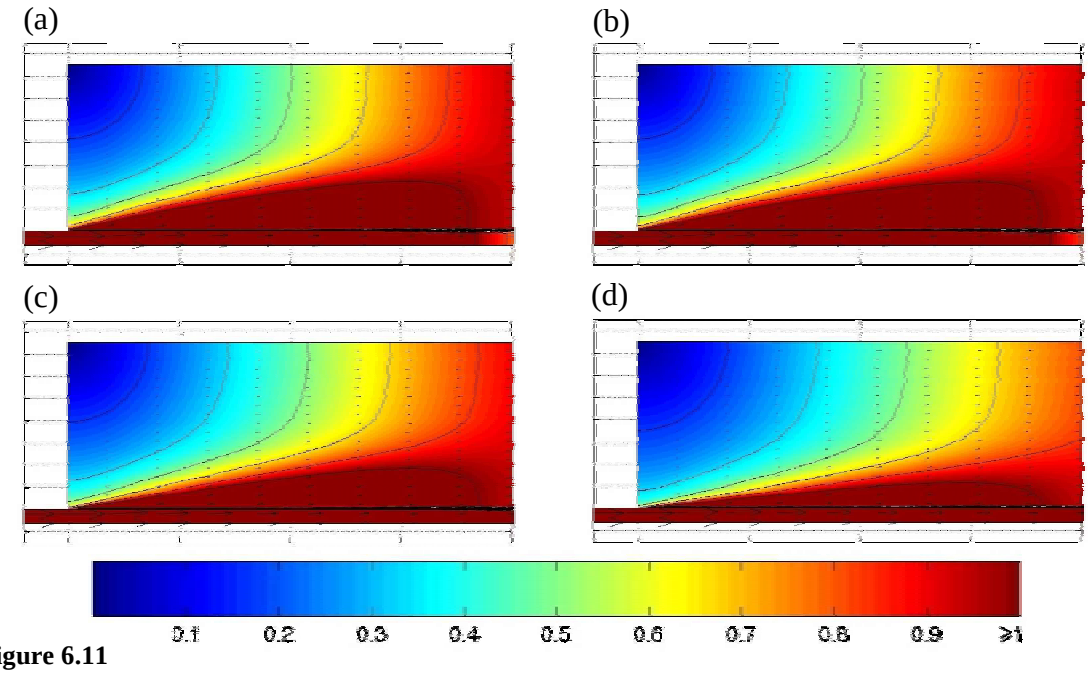

Figure 6.11
Current density distributions of the Ag-HTS *in-situ* contact normalised with respect to the macroscopic current density, $I_{app}/(t_s w)$, for applied currents of $0.5I_{app}$, $1I_{app}$, $2I_{app}$ and $3I_{app}$ (plots a-d respectively). The current density distributions are derived from FE model solutions. The superconducting region has an n-value of 6 and anisotropy ratio of 5. The region $x = -2\times10^{-3}$ to $x = 2\times10^{-3}$ m is shown. Arrows indicate current density vectors.

reaches a maximum value in this region away from the point of initial current transfer in the TL regime. The maximum starts near $x = 0$ for low applied current values and moves along the interface for increasing current and increasing anisotropy value. Maximum power dissipation will occur coincident to this location in the form of Joule heating and is therefore likely to be the site from which thermal quenching of the superconductor propagates in the event of inadequate local cooling power. This maximum is principally due to a local maximum in the current density component J_x. Under the influence of an applied electric potential along the x-axis the current transferred near $x = 0$ flows predominantly near and parallel to the contact interface. The local absolute magnitude of the current density becomes maximal near (but not at) the contact interface as additional current transfers across the interface further along the contact. The mitigation of the current density component, J_y, at x=0 allows the component, J_x, to dominate the resolved J at a point further down the contact. It is important to note that in the low applied current regime, the nonlinear model does not approximate the linear model; the current density distributions remain different.

Current transfer and thereby current sharing between metal contact and the HTS is mediated by J_y across the contact interface. Increasing mitigation of J_y with increasing

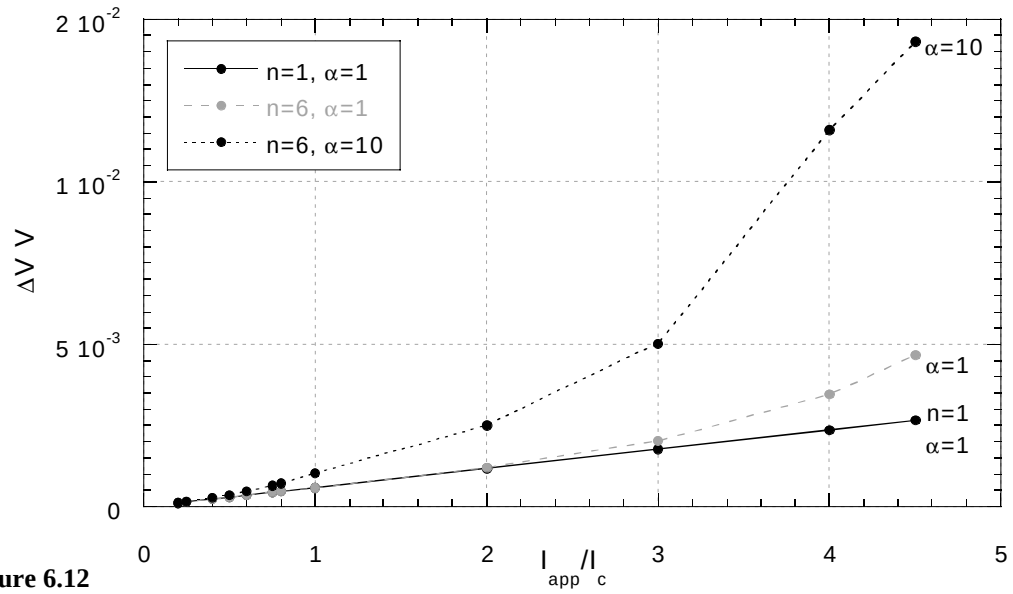

Figure 6.12
Plot of ΔV across the Au *in-situ* metal contact insert as a function of the applied current normalised with respect to the critical current. FE model derived values are presented. The FE model data presents solutions with n -values of 1 and 6 for anisotropy factors of 1 and 10.

current anisotropy, leads to greater current sharing and a larger region of high current transfer between the normal and superconducting contact components, as plots a-c and d-f of figure 6.10 indicate. Whereas the anisotropy ratio has an effect upon the current density distribution of the HTS component for solutions with $n = 1$, a factor of 5 increase in the y-axis components of the HTS resistivity is not sufficient to change the contact transfer characteristic $V(x)$. All solutions with $n = 1$ only exhibit TL model behaviour.

Examination of the normalised current density shows a gradual change in the distribution with increasing applied current (see figure 6.11). As the applied current increases, the local resistivity value increases over the superconducting region and becomes an increasing hindrance to current flow. This also leads to greater current sharing between the metal contact and HTS bulk material with a more gradual transfer across the contact interface along the length; as indicated by the current density vectors. This is also manifest in the deviation from the analytical, approximately exponential, behaviour of $V(x)$.

For increasing applied current, the current dependent nonlinear local resistivity minimises current crowding and the formation of high current density regions in favour of a more even distribution, which in accordance with current conservation is over a larger region. The spreading of this current density leads to an increasingly smaller region of high normalised current density as plots a-d of figure 6.11 show. Both gold *in-situ* and lap current contacts have been modelled. The geometry of the lap contact was identical to that of the *in-situ* contact except for a boundary condition at $x = d$ which prevented current

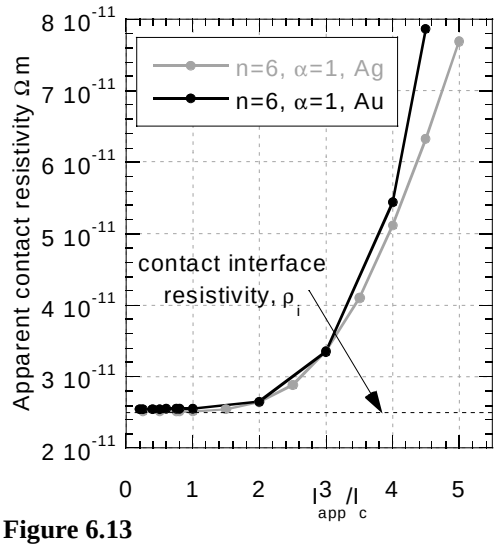

Figure 6.13
Comparison of the contact resistivity of the Ag (black closed circles) and Au (grey closed circles) *in-situ* metal contact insert as a function of the applied current normalised with respect to the critical current. FE model derived values are presented. The FE model data presents solutions with n =6 and α =1.

transfer across the end of the contact metal insert. For solution values with n =1, 5, 6 and α =1, 3, 5 there is no significant difference between the current density distributions for the two geometries. Current density values in the metal contact near $x = d$ were both exceedingly small, which corroborates the assumption of section 6.3. The current transfer behaviour described in this chapter can also therefore be used to describe current transfer behaviour in the current contact lap geometry.

Comparison of $\Delta V\left(I_{app}\right)$ for the FE model of the Ag contact and experiment shows good agreement (see figure 6.8). The nonlinear FE model and the experimental data possess the same quadratic functional dependence as the experimental data over the entire current regime. Whereas the FE model shows similar behaviour to the experimental data, exact agreement is not expected due the experimental sample's higher values of n and d of 8 and 8×10^{-3} m respectively. The FD model solutions exhibit similar behaviour over the applied current regime $I_{app} = 1I_c - 1.6I_c$ examined. The quadratic functional dependence of $\Delta V\left(I_{app}\right)$ can be attributed to the current dependence of the bulk resistivity component of the contact resistance, which increases with increasing applied current.

The distribution $\Delta V\left(I_{app}\right)$ of the FE model of the Au contact has a larger R_c value as indicated by the steeper slope of the linear section of $\Delta V\left(I_{app}\right)$ and has a value the same as that calculated using equation (6.10). The balance of current sharing between the HTS component and contact metal shunt is different for gold and silver contacts. The greater resistivity of gold leads to a smaller proportion of current per unit length in the gold contact. By implication a greater proportion of current flows in the HTS component. This is evident in the deviation from the TL model (n =1, $\alpha = 1$) at lower values of I_{app}/I_c for the gold contact than the silver contact ($0.2I_{app}/I_c$) and for increasing values of α. The curvature of $\Delta V\left(I_{app}\right)$ is also greater in the case of the gold contact than the silver contact,

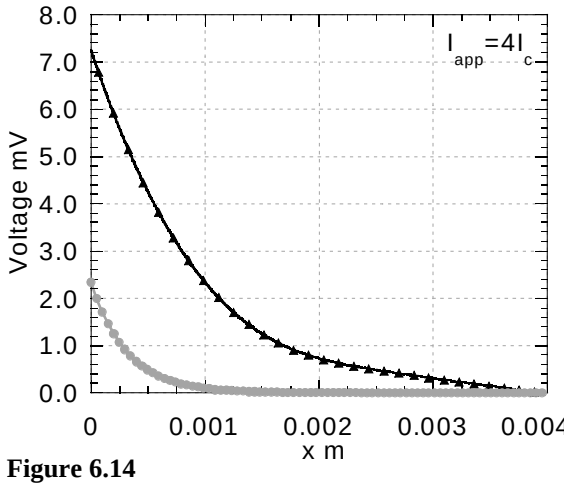

Figure 6.14
Comparison of the voltage distribution along the Au contact midline, determined using a FE model, with the voltage distribution calculated using a TL model approximation. Grey closed circles indicate TL model calculated values of the voltage along the contact midline. Black closed triangles indicate the FE model calculated values of the voltage distribution along the contact midline for a solution with $n = 6$ and $\alpha = 5$.

irrespective of the steeper slope of the linear section. This is more clearly shown by comparison of the contact resistivities of the silver and gold contacts (see figure 6.13). The contact resistivity of a contact to a nonlinear device is a spatially complex quantity. Assuming the contact length is much greater then the length over which most current transfers from the contact to the device, an approximation using equation (6.10) can be calculated and is presented in figure 6.13; direct comparison of the curvature of the plots is independent of this approximation. Figure 6.13 also more clearly shows the constant contact resistivity component of the contact resistivity. Deviation of $\Delta V\left(I_{app}\right)$, calculated for the nonlinear case, from the TL model occurs at a smaller value of I_{app}. This indicates that a greater contact metal resistivity and/or anisotropy value (better texturing) leads to an increase in the significance of nonlinear effects at a smaller applied current. Examination of the voltage distribution along the contact at the same applied current (compare figure 6.9 plot a and figure 6.14) shows higher values of the voltage at $x = 0$ (as expected for a more resistive contact material) and a more rapid decay of $V(x)$ over the contact length; a result of greater current transfer per unit length from the contact to the HTS component.

6.6 Summary

A model, which accounts for the current transfer behaviour of current contacts to HTSs at current in excess of the critical current has been presented and corroborated by numerical modelling. Comparison of the total voltage drop across the contact as a function of applied current for both the FE model and experiment shows good agreement. The nonlinear FE model reproduces exactly the analytical behaviour of the TL model and experimental data in the low applied current regime; and exhibits the same functional dependence as the experimental data over the entire current regime for both $\Delta V\left(I_{app}\right)$ and $V(x)$. The

behaviour of current transfer in current contacts to HTSs has been described and can be considered to possess different behaviour in two different regimes. At applied currents in excess of the critical current of a contacted device, the contact interface resistance and current transfer length increase nonlinearly. This presents a further factor to consider in the development of current contacts for high power HTS applications. The resistivity of the metal contact material has also been shown to have a more complex influence on the current transfer behaviour of contacts to nonlinear devices than contacts to devices with linear EJ characteristics. Current transfer has been shown to be practicably identical in the *in-situ* and lap contact geometries of the dimension modelled in this chapter. A high current density region at the contact interface to nonlinear media forms at a point near but not coincident with $x = 0$, unlike contacts to ohmic conductors. This maximum moves along the interface for increasing current and increasing anisotropy value.

6.7 References

1 D. R. Watson, M. Chen, D. M. Glowacka, N. Adamopoulos, B. Soylu, B. A. Glowacki, and J. E. Evetts, Ieee Transactions On Applied Superconductivity **5,** 801-804 (1995).

2 H. H. Berger, Solid-State Electronics **15,** 145-158 (1972).

3 M. N. Wilson, *Superconducting Magnets* (Clarendon Press, Oxford, 1983).

4 D. R. Watson and J. E. Evetts, Superconductor Science & Technology **9,** 327-332 (1996).

5 A. Kursumovic, J. E. Evetts, D. R. Watson, B. A. Glowacki, S. P. Ashworth, and A. M. Campbell, Institute Of Physics Conference Series**,** 1623-1626 (1997).

6 D. P. Kennedy and P. C. Murley, IBM J. Res. Develop. **12,** 242-250 (1968).

7 H. Murrman and D. Widmann, IEEE Transactions on Electron Devices **16,** 1022-1024 (1969).

8 A. Kursumovic, R. P. Baranowski, and J. E. Evetts, Accepted for publication in the Journal of Applied Physics (1999).

9 D. R. Croft and J. A. R. Stone, *Heat Transfer Calculations using Finite Difference Equations* (PAVIC Publications, Sheffield, 1977).

10 R. P. Baranowski, D. R. Watson, and J. E. Evetts, Institute of Physics Conference Series**,** 1619-1622 (1997).

CHAPTER 7

Current transfer on the microscopic scale: Microstructural current transfer models

7.1 Introduction

As discussed in section 2.4, it is now well established that macroscopic current transfer within the electrically connected volume of polycrystalline high-T_c superconductors is determined principally by the type and/or properties of the boundaries between the superconducting grains. The brick-wall and railway-switch models propose that c-axis twist grain boundaries and c-axis tilt grain boundaries are the dominant intergranular connexions that control the macroscopic current transfer in textured bulk polycrystalline Bi-2212 and Bi-2223 PIT superconducting tapes. This chapter presents modelling of current transfer between c-axis, low-angle c-axis and edge-on c-axis tilt oriented grain interfaces and produces quantitative and qualitative results from these mainly qualitative microstructural descriptions. The first part of this chapter examines current transfer behaviour in a weak link free brick-wall model. The later part presents the results of a model of current transfer in strongly connected low-angle c-axis and edge-on c-axis tilt grain boundaries, which form the suggested current transfer mechanism of the railway-switch model.

7.2 Current transfer models in polycrystalline HTSs

Bulk superconductor optimisation has moved from an heuristic assay of preparation parameters to a more focused strategy based upon understanding the current transfer mechanism within the microstructure of polycrystalline HTSs and relating this to aspects of the preparation techniques.

Table 7.4 *Colony and 'grain' size of several polycrystalline HTS compounds.*

Reference	HTS	Microstructural unit	Length (ab-plane) m	Thickness (c-axis) m
Grindatto, Bulaevskii[1]	Bi-2223	Colony	$10-20\times10^{-6}$	1×10^{-6}
Pashitski[2]	$TlBa_2Ca_2Cu_3O_x$	Colony	$1-2\times10^{-3}$	$5-30\times10^{-6}$
Adamopoulos[3]	Bi-2212 (CRT)	'Grain'	50×10^{-6}	1×10^{-6}
Pardo[4]	$Gd_1Ba_2Cu_3O_7$	'Grain'	80×10^{-6}	-

As discussed in section 2.5.1 the colony is the basic current transport element of the brick-wall and railway-switch models and both models examine current transfer at different types of boundaries between such colonies. Individual grains in the colonies are separated by twist grain boundaries and therefore colony boundaries consist of grain boundaries of different types. However, these models principally discuss current transfer at colony boundaries that only consist of a single type of grain boundary connexion. The numerical models presented in this chapter similarly only examine pure types of boundary and therefore the terms grain and colony boundary only differentiate the scale of current transfer discussed. Table 7.1 indicates that there is a range of typical colony and grain sizes (where the term 'grain' is referenced as an ambiguous microstructural unit), for HTS materials with suspected brick-wall or railway-switch model current behaviour. Whereas the aspect ratio of the modelled systems is of import, the absolute sizes of the grains/colonies should be immaterial in assessing the qualitative behaviour of current transfer in brick-wall and railway-switch models. The current elements of the models presented in this chapter most closely comply with the size of colonies in the brick-wall and railway-switch models i.e. in Bi-2223 PIT tapes. Bulk transfer of current through the geometry of the brick-wall and railway-switch models is assumed. Recent studies suggest this may not be appropriate for all field and temperature regimes (see section 2.5.1). This section discusses the brick-wall and railway-switch models, the two principal microstructural models of current in bulk polycrystalline HTS.

7.2.1 The brick-wall model

The brick-wall microstructure, as discussed in section 2.4, restricts intergrain current flow between c-axis twist grain boundaries. Dimos *et al*[5] have shown that there is a strong reduction of the critical current density across tilted and twisted ab-plane thin film Y-123 bicrystal grain boundaries and that the presence of a weak magnetic field further limits the grain boundary critical current. The brick-wall model assumes zero current transfer at twisted and tilted ab-plane grain boundaries in bismuth polycrystalline HTS systems, and

as such, represent the main obstacles to current, especially in the presence of a magnetic field. The brick-wall model further assumes that the macroscopic current in polycrystalline HTSs is determined by the Jospephson critical current at c-axis twist boundary weak links. Therefore, the critical current of a single c-axis twist boundary determines the macroscopic critical current as well as its magnetic field and temperature dependencies. A generalised brick-wall model has been developed that takes into account a distribution of grain sizes and weak link coupling strengths, and includes ab-plane Jospehson coupled weak links[1].

The results of various studies of silver clad bismuth polycrystalline HTS tapes do not match the assumptions and predictions of the brick-wall model. These studies indicate that any weak links that may exist within the microstructure reduce the active cross-sectional area of a tape but do not limit the critical current in the strongly connected fraction of the conductor. Microstructural studies have demonstrated that c-axis twist colony/grain boundaries occur infrequently in the superconducting core of Bi-2223 tapes and typically contain amorphous layers at the boundary which are likely to be insulating[6-8]. This indicates that the brick-wall microstructure is unrealistic and that c-axis current transfer is unlikely. The measured value of J_c / J_c^{norm} in Bi-2223 tapes is several orders of magnitude smaller than that characteristic of Bi-2212 crystals and the resistivity normal to the plane is metallic in contrast to the semiconducting temperature dependence of Bi-2212 crystals[9]. If the physical properties of Bi-2212 are similar to those of the Bi-2223 material, this suggests that macroscopic current transfer in the c-axis direction is not via single crystal c-axis conduction in contradiction with the brick-wall model. Investigations of the c-axis critical current transport of single crystal Bi-2212, Y-123, $(Bi_{1-x}, Pb_x)_2Sr_2CaCu_2O_8$ and $Tl_2Sr_2CaCu_3O_{10}$ show that these materials behave like stacks of superconductor-insulator-superconductor Josephson junctions[10]. Hensel *et al*[11] assume that a lower limit for $J_{c,c}$ of a single crystal is simply $J_{c,c} = J_c^m / \gamma$, where γ is the aspect ratio of a single grain (typically $\gamma = 20$). Given that the J_c of bulk Bi-2223 tapes typically has a value 650×10^6 A·m^{-2} at 4.2 K and zero field, $J_{c,c}$ is still higher than typical single crystal values (see table 2.1) and also higher than the zero-field Josephson critical current density across a c-axis twist grain boundary[12]. This implies that single crystal Josephson weak links do not determine the macroscopic current transport.

Examination of the temperature and magnetic field dependence of J_c further suggests that macroscopic current transport involves little or no c-axis conduction. The scaling of the in plane J_c and J_c^{norm} as a function of the direction of an applied magnetic field (see section 3.4.2) is very similar and indicates that the dissipation of the components of the critical current results from the same physical origin, namely the dissipation of the in plane component of the current[13]. This is corroborated by the similar magnetic field dependence of the normal and in plane resistivities[9]. The temperature dependence of $J_{c,c}$ for single crystals and J_c for tapes should be very similar if current transfer is controlled by c-axis twist grain boundaries. This is not observed experimentally[14], adding further doubt on the ability of the brick-wall model to describe realistically current transfer in Bi-2223 tapes or bulk polycrystalline Bi-2212.

7.2.2 The railway-switch model

The railway-switch model relies on current transport inside the ab-planes of interconnecting colonies and the assumption that low-angle c-axis tilt boundaries constitute strong connexions. Section 7.2.1 details some of the evidence that suggests current transport in polycrystalline HTSs is determined predominantly by ab-planar current transport. There are principally two structurally identified boundary types joining the colonies at the edges; low-angle c-axis (LAC) grain boundaries and edge-on c-axis (EOC) tilt grain boundaries. The LAC boundary (see figure 7.1) consists of one colony edge meeting the broad face of another colony at a low angle. EOC boundaries (see figure 7.1) are formed by conjoining the edges of two neighbouring colonies whose c-axes lie in the same plane but are tilted with respect to each other. Detailed microstructural investigations of Bi-2223 PIT tapes reveal that tilt boundaries, in contrast to c-axis twist boundaries, are common[15]. Goyal *et al*[16] have shown that over 40 % of boundaries are low-angle; i.e. have misorientation angles of less than 15°.

LAC and EOC boundaries are not the dominant current transfer limiting mechanism of the railway-switch model. The railway-switch model contends that LAC and EOC boundaries are strong connexions in the sense that they do not represent weak links, in apparent contradiction to the thin film transport current studies of Dimos *et al*[5]. Current distribution in the direction normal to the tape plane occurs along the ab-plane of misoriented grains and colonies. However, the railway-switch model contends that this mechanism alone is insufficient to explain the high J_c^{norm} values observed in Bi-2233 PIT tapes. It is suggested

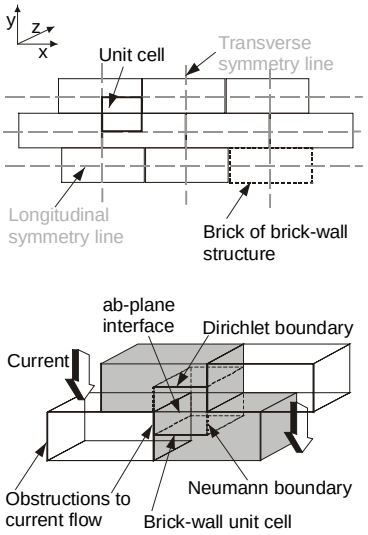

Figure 7.1
Schematic representation of the brick-wall microstructure and the brick-wall unit cell geometry.

that current is mediated by a 3D current flow path that connects 2D layers of EOC boundaries. This 3D path is formed by LAC boundaries, which are considered an essential component of the railway-switch model.

Irrespective of the precise current flow path, the percolative nature of the macroscopic current has been ascribed to sample inhomogeneity. Magnetic measurements of the EJ characteristic and current length scales combined with transport measurements of a Bi-2223 polycrystalline sample indicate that at high magnetic fields the distribution of current fragments into macroscopic islands connected by narrow bridges of current[17]. This field and temperature dependent fragmentation is attributed to a weak link network in which current flows through a series of grain boundaries, which provide links of varying coupling strength. Increasing field moderates the weak link behaviour and some different dissipation mechanism becomes dominant. It is suggested that this mechanism is related to the low-angle grain boundaries of the railway-switch model[18].

7.3 Finite element model of current flow in the brick-wall model microstructure

This section examines current transfer behaviour in a weak link free brick-wall model as a limiting case of the more complex railway-switch model. The bricks of the microstructure have been treated as nonlinear anisotropic electrically conductive media and current flow calculated using a FE model. The following section describes the geometry of the model. The calculated results presenting current flow in this structure are discussed in the latter sections.

Although the brick-wall model is no longer considered a dominant mechanism for macroscopic current transfer in high quality tapes, it is a simpler and more readily analysed system than the railway-switch model, and there is some evidence that it may play a minor role[1]. The brick-wall model may, however, describe more realistically current transfer in tapes with less textured inhomogeneous microstructures[8]. Such poor quality tapes contain many barriers to current flow along the plane of the tape, which may induce current flow along c-axis direction. The numerical model results of section 5.3.2

suggest that such current transfer would occur via uniform current transport in the c-axis direction between current barriers. The $J_c(H)$ characteristics of $Gd_1Ba_2Cu_3O_7$ have been found to agree well with the behaviour of the brick-wall model[4] and suggest that current transfer in this material may be described well by the brick-wall model.

The models presented in this chapter assume strong brick boundary connexions. There is evidence from Bi-2212 bicrystal measurements that high angle twist grain boundaries do not demonstrate weak link behaviour[19], however even if this is not representative of c-axis twist boundaries in bulk HTSs the current transfer model presented is only intended as a simplification. Indeed the specification of a field dependent grain boundary condition, although possible, would introduce greater complexity into an already numerous set of interdependent parameters.

Certain practical applications require large or relatively complex HTS ceramic structures, e.g. large HTS cylinders. Some of the limitations imposed on component manufacture by ceramic processing techniques can be overcome by joining individual components to form a composite structure. The geometry of the model described in section 7.3 is identical to that of the joint section of an idealised joint between two superconducting leads. The results and discussion of current transfer in the brick-wall microstructure therefore also describe the behaviour of current flow in superconducting joints.

7.3.1 Finite element model of the brick-wall unit cell

A single unit cell of the brick-wall microstructure has been modelled (see figure 7.2). No weak link behaviour is assumed at the interface between the two brick quarter sections that constitute the unit cell. A single brick of the brick-wall model has symmetry lines along its longitudinal and transverse axes. Deep within a sample, where external edges can be assumed to have negligible effect, the basic repeating unit cell of the brick-wall microstructure is a single quadrant, as delineated by the symmetry lines, of a single brick (see figure 7.2). Mirror inversion and translation of the current flow pattern in this cell recreates the macroscopic current flow pattern of the brick-wall microstructure. The identical current flow patterns either side of the longitudinal symmetry line give rise to a constant field condition along the symmetry line and is a boundary condition of the model. Similarly, the transverse symmetry line possesses a constant field condition along the symmetry line. For the case of current injection or egress from the unit cell, the transverse symmetry line engenders an electric field condition which is normal to the symmetry line

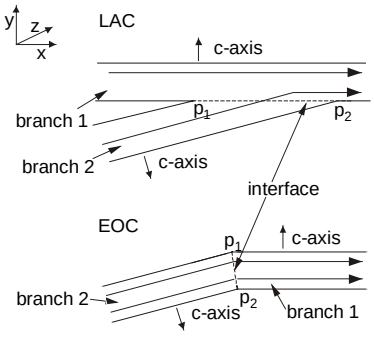

Figure 7.2
Schematic representation of the low-angle c-axis (indicated as LAC) and the edge-on c-axis (indicated as EOC) grain/colony boundary geometries.

in order to maintain a symmetric current distribution immediately either side. These Dirichlet and Neumann boundary conditions are shown schematically in figure 7.2.

A number of solutions (~ 600) have been calculated using different aspect ratio, γ, n-value, and anisotropy ratio. The applied current has a value equal to the critical current as derived from the critical current density value, defined as $J_c = 5\times10^6$ A·m^{-2}, and the brick cross sectional area in the yz-plane (see figure 7.2). The thickness of the bricks is 1×10^{-6} m and was kept constant. Changing the longitudinal x-axis dimension of the bricks changed the aspect ratio. The bricks in the model are of approximately the same size as Bi-2223 colonies. To keep the spatial resolution of the mesh similar in models of different physical size, the mesh for models of different aspect ratio was refined to varying degrees. The models contain between 10×10^3 and 35×10^3 solution points.

7.3.2 Current flow in the brick-wall microstructure

As an aid to the conceptualisation of current flow in the brick-wall model, the current density distribution in small sections of brick-wall microstructures composing of bricks with aspect ratios of 10 and 20 has been constructed using the current density distribution of individual unit cells (see foldout figure 7.3). Comparison of the brick-wall microstructure with aspect ratio of 20 in the linear ($n=1$) and nonlinear case ($n>1$), shows a more even distribution of current density in the region of the current constriction (ab-plane grain boundaries, shown schematically as black vertical lines in figure 7.3) for $n\neq1$ as discussed in section 5.3.3. Within a single brick with $n>1$ the current distribution is more uniform across the cross section at a single point along the brick than the $n=1$ case. The cross section available for current transfer at the aligned ab-plane grain boundaries is half that of the macroscopic cross section available for current transfer elsewhere in the brick-wall microstructure. In the region midway between the aligned ab-plane grain boundaries, the current density value is maximum and approaches the macroscopic average value midway between the constriction and an ab-plane boundary. At the ab-plane boundary (bottom and top of the unit cell), the current density value reduces to zero. The ab-plane obstacle to current flow forces current to flow from brick to

brick across the c-axis boundary, the reduction in the current density value and current value over the half brick length is indicative of this y-axis component of current transfer between bricks.

In the linear case the only constraints on the current density distribution are those imposed by the geometry and anisotropy, whereas the nonlinearly conducting brick-wall microstructure has the further current density value minimisation requirement imposed by the EJ characteristic of the conductor. This results in the bulk of current transferring over much more of the ab-plane interface between bricks in the nonlinear structure in order to minimise local high current density values. Current transfer in the linear structure does not have this further constraint and therefore equilibrates over a much smaller volume.

7.3.3 The current distribution in the brick-wall unit cell

The behaviour of current flow in the brick-wall unit cell is characteristic of the entire brick-wall microstructure and is used to study the γ, n and α dependencies of current flow. Figure 7.4 shows plots of the normalised current density distribution in the brick-wall unit cell for n-values of 1, 4, 6, 8 and $\alpha = 1$ (figure 7.4, plots a-d) and 20 (figure 7.4, plots e-h). Comparison of current distributions in figure 7.4, plots a and e, with the rest of the plots again shows the more uniform distribution of current at the region of constriction. This is most clearly shown by the current density vectors extending beyond the brick geometry near the point of current egress. Further comparison of current flow shows different qualitative behaviour. The brick-wall unit cell with $n = 1$ only contains lines of constant current density value with positive or negative curvature whereas lines of constant current density value in plots with $n > 1$ comprise a mixture of the two and zero curvature (concave up, concave down and straight line).

Increasing n-value, increases the power dissipation at regions of high current density and decreases the maximum current density value within the geometry as shown in table 7.2. The maximum value of J decreases more gradually with increasing n. With increasing n, the system approximates the Bean critical state model with increasing accuracy and the highest current density value gradually approaches the critical value. Note most current density vectors in the n=1 plots are smaller because current density vectors are normalised with respect to the maximum current density value, this is higher in the linear case because current crowding is more readily achieved.

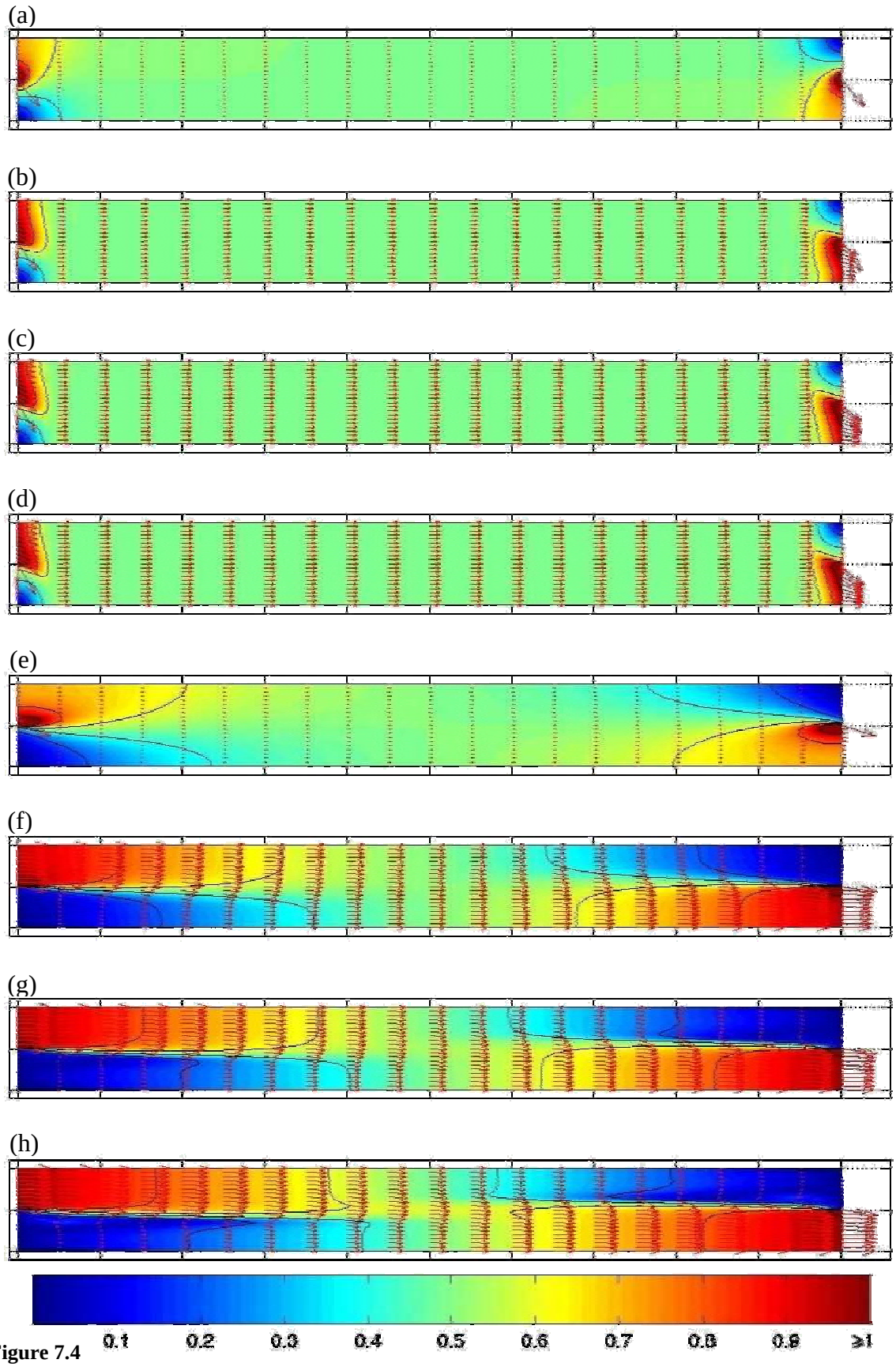

Figure 7.4
Current density distributions of the brick-wall unit cell normalised with respect to the macroscopic current density, ($I_{app} \times$ unit cell cross sectional area) and an aspect ratio of 20. I_{app} is equal to the critical current of the brick-wall unit cell. Plots (a)-(d) present isotropic solutions with n-values of 1, 4, 6, 8 respectively. Plots (e)-(h) present anisotropic solutions with α =20 and n-values of 1, 4, 6, 8 respectively. The colourbar legend indicates the magnitude of the current density in $A \cdot m^{-2}$. Arrows indicate current density vectors.

Table 7.2 *Maximum current density values in brick-wall unit cell geometry for various n and α.*

	Maximum J A·m^{-2}, $n=1$	Maximum J A·m^{-2}, $n=4$	Maximum J A·m^{-2}, $n=6$	Maximum J A·m^{-2}, $n=8$
$\alpha=1$	1.7544×10^{8}	3.3609×10^{7}	2.4170×10^{7}	2.1058×10^{7}
$\alpha=20$	1.6343×10^{8}	1.9726×10^{7}	1.5271×10^{7}	1.4049×10^{7}

The brick-wall unit cells with $n=4$, 6, 8 and $\alpha=1$ have very similar current density distributions. For $\alpha=20$ and $n=4$, 6, 8 the power dissipation dependence is more sensitive to the local value of J_y. Current preferentially transfers in the x-axis direction and distributes itself in the y-axis direction more uniformly across the ab-plane interface between bricks (midline of the brick-wall unit cell, as illustrated in figure 7.2). Figure 7.4 shows the redistribution of current for increasing anisotropy value in the linear and nonlinear cases. The increasing preference for current transfer in the x-axis direction with increasing α is most clearly shown by the gradual alignment with the x-axis of the current density vectors near the point of current egress (see figure 7.4, plots e-h).

The current distribution in the brick-wall unit cell with $n=8$ and $\alpha=20$ for various aspect ratios is presented in figure 7.5. For increasing aspect ratio, the region of uniform current flow in the middle of the brick-wall unit cell extends over a greater proportion of the unit cell length. The central sections of the current distribution show uniform current flow with current density value equal to the macroscopic critical current density value of 5×10^{6} A·m^{-2} and are not shown in order to maximise the plot size (see figure 7.5, plots c and d). Increments along the x-axis are spaced in 1×10^{-6} m intervals. Comparison of the relative size of the current density vectors across the cross section of the unit cell geometry, indicates that current flow becomes uniform across the cross section over a shorter distance as the value of γ increases.

Figure 7.6 is a plot of the current density value along the brick to brick interface. The zero current density value at the boundary has been omitted from the plots for clarity. The region over which the current density value plateaus at 5×10^{6} A·m^{-2} has uniform current flow along the x-axis with zero y-axis current density component. The non-plateau regions are where y-axis current transfer mediates the current transfer to the next brick. The current density value along the brick to brick interface does not have a plateau region for approximately $\alpha \geq \gamma$. This finding is consistent for all anisotropy and aspect ratios calculated in this study. A simple model of current transfer in the brick-wall unit cell based on global current flows, provides some insight into this finding. To facilitate total

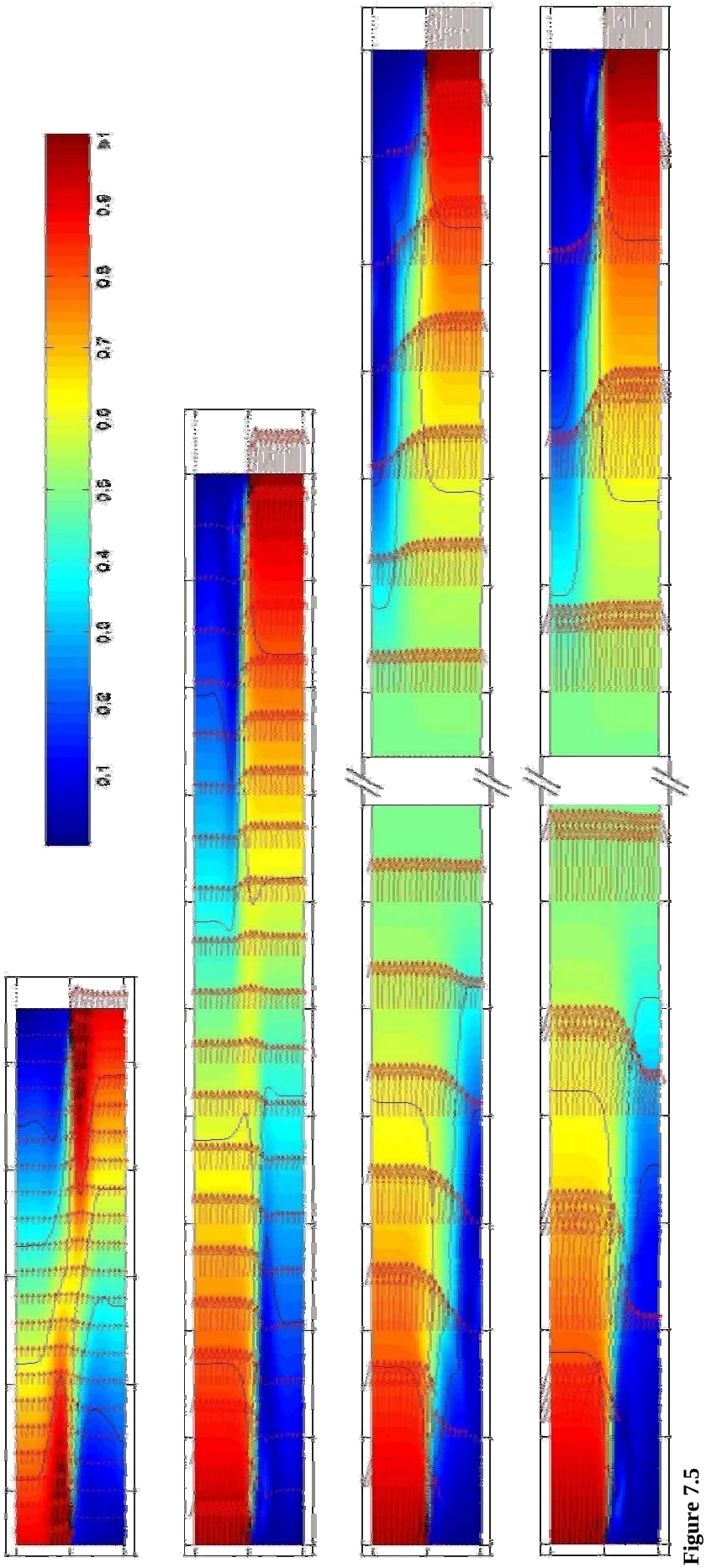

Figure 7.5
Current density distributions of the brick-wall unit cell normalised with respect to the macroscopic current density, (I_{app}/unit cell cross sectional area). All the plots presented are of solutions with n=8 and an anisotropy ratio of 20. Plots (a)-(d) have aspect ratios of 10, 20, 40, 80 respectively. Broken lines indicate regions of uniform current flow which have been removed for purposes of presentation. The colourbar legend indicates the magnitude of the normalised current density. Arrows indicate current density vectors.

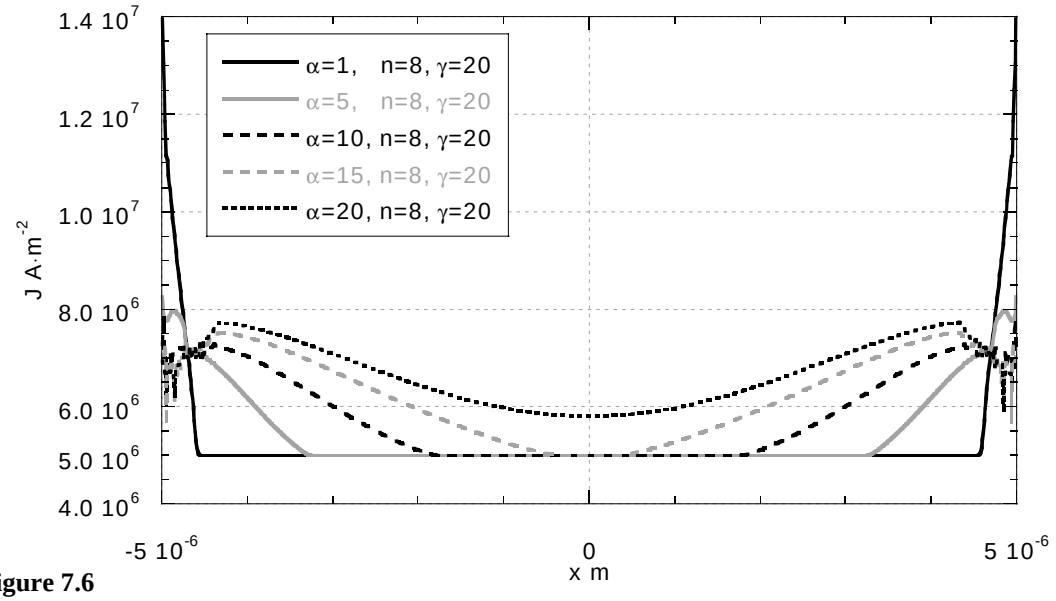

Figure 7.6
Plot of current density magnitude along the ab-plane interface of the brick-wall unit cell (see figure 7.1) for solutions with n =8, γ =20 and several aspect ratios, α =1, 5, 10, 15, 20.

current egress all current must pass from the upper half of the brick-wall geometry to the lower half. Consider the total cross sections for the current flow in the x and y directions, although $J_{c,y}$ is a factor α larger than $J_{c,x}$, the total cross section available for current transfer in the y-axis direction is a factor γ larger than that in the x-axis direction. For the applied current condition $I_{app} = I_c$ as described in section 7.3.1, brick-wall unit cell solutions with $\alpha \geq \gamma$ possess the condition $J_y \geq J_{c,y}$ at least at one point across the interface since a uniform current flow condition cannot support the condition $J_y < J_{c,y}$. Given this condition, current flow in the y-axis direction utilises the entire xz-plane cross sectional area in order to minimise the significant ρ_y component of the local resistivity which becomes comparable and increasingly larger than ρ_x for $J_y \geq J_{c,y}$; thereby minimising an exponential increase in power loss. For increasing n-value the current density line plots along the brick to brick interface are virtually identical and show that the current density value equilibrates to the macroscopic current density value over a short distance, $0.47\times10^{-6} - 0.64\times10^{-6}$ m, from the point of current injection.

The path across the brick-wall unit cell, along which the current density value has maximal value, has been calculated and is illustrated in figure 7.7. Path discontinuities are due to interpolation errors. Regions of uniform current flow possess current density values that only differ by the error associated with the solution and postprocessing approximations. Therefore the path of maximum current density cannot be defined in such

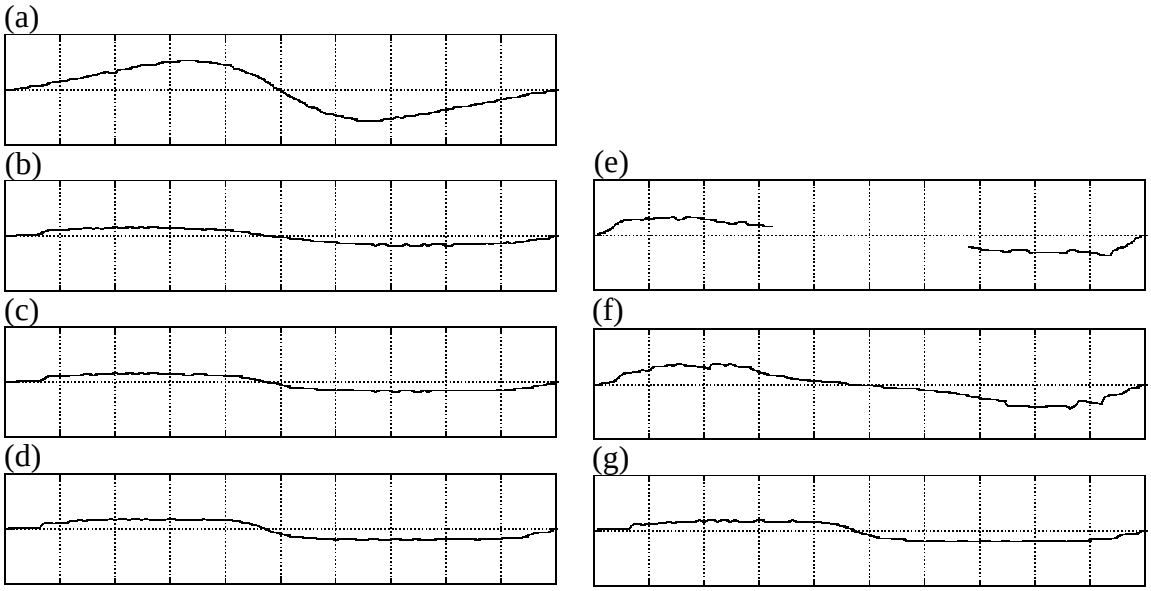

Figure 7.7
Plots indicating the path of maximum current density across a brick-wall unit cell possessing an aspect ratio of 10. Plots (a)-(d) are calculated from solutions with α =20 and n =1, 4, 6, 8 respectively. Plots (e)-(g) are calculated from solutions with n =8 and α =5, 10, 20 respectively. Increments along the x-axis are spaced in 0.5×10^{-6} m intervals

regions and is omitted in figure 7.7. Increasing n-value and anisotropy factor seem to shift the point of maximal current transfer across the ab-plane brick interface from the midpoint closer to the point of current injection. Consistent with the picture of increasing anisotropy constraining current flow in the y-axis direction, especially for $n>1$, the current path wends about the ab-plane brick interface on a smaller pitch (as viewed in 2D projection).

7.4 Finite element model of current flow in the railway-switch model microstructure

Current transfer in LAC and EOC grain/colony boundary structures of Bi-2223 tapes has been modelled. The colonies of the microstructure have been treated as nonlinear anisotropic electrically conductive media and current flow calculated using a FE model. The following section describes the geometry of the models and how the resistivity of grains with crystallographic orientation that is not coincident with the global co-ordinate system of the geometry is dealt with. Solutions of the current flow in these structures are presented and discussed in the latter sections.

7.4.1 Finite element model of the railway-switch LAC and EOC boundaries

A c-axis tilt boundary consists of two colonies/grains with crystallographic orientations that are not coincident with one another such the c-axes of each colony/grain point in directions at an angle, ϕ_{gc}, to each other. Any physical properties that depend upon relative direction to crystal axes, such as conductivity, can no longer be defined with respect to one set of axes. For representation within a FE model, these material properties must be transformed such that they can be defined in a single frame of reference. The geometries of the current transport models presented are schematically identical to those presented in figure 7.1. As mentioned in section 4.3.1 equations (4.9a), (4.9b) and (4.10) are defined in a local co-ordinate frame with axes x' and y'. Within the individual grain the local resistivity is determined by equations (4.9a) and (4.9b), with local current preferentially flowing along the ab-planar direction. The c-axis of individual grains lies parallel to y', and the x'-axis lies in the ab-plane. If one grain is oriented such that $x' \| x$ and $y' \| y$, then the local co-ordinate axes of the other grain are at an angle ϕ_{gc} to the global co-ordinate system (see figure 7.8). The FE model only has a single global frame in which the components of the resistivity terms of each part of a composite structure are defined. An equivalent resistivity matrix in the global frame must therefore be calculated from the local resistivity term. An orthotropic material with local resistivity matrix

$$\begin{bmatrix} \rho_{x'x'} & 0 \\ 0 & \rho_{y'y'} \end{bmatrix}$$

can be transformed to an equivalent global resistivity matrix

$$\begin{bmatrix} \rho_{xx} & \rho_{xy} \\ \rho_{yx} & \rho_{yy} \end{bmatrix}$$

with the application of the following cosine matrices

$$\begin{bmatrix} \rho_{xx} & \rho_{xy} \\ \rho_{yx} & \rho_{yy} \end{bmatrix} = \begin{bmatrix} \cos\phi_{gc} & -\sin\phi_{gc} \\ \sin\phi_{gc} & \cos\phi_{gc} \end{bmatrix} \begin{bmatrix} \rho_{x'x'} & 0 \\ 0 & \rho_{y'y'} \end{bmatrix} \begin{bmatrix} \cos\phi_{gc} & \sin\phi_{gc} \\ -\sin\phi_{gc} & \cos\phi_{gc} \end{bmatrix}$$

which leads, for a tilted colony/grain, to the following new global frame resistivity components of the magnetic flux diffusion equation (4.4)

$$\rho_{xx} = \rho_{x'x'} \cos^2 \phi_{gc} + \rho_{y'y'} \sin^2 \phi_{gc}$$

$$\rho_{xy} = \rho_{yx} = \left(\rho_{x'x'} - \rho_{y'y'}\right) \cos\phi_{gc} \sin\phi_{gc}$$

$$\rho_{yy} = \rho_{x'x'} \sin^2 \phi_{gc} + \rho_{y'y'} \cos^2 \phi_{gc}.$$

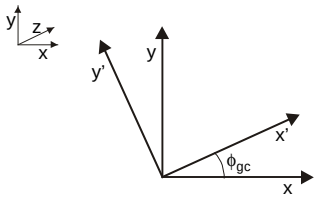

Figure 7.8
Diagram indicating the rotation of the local axes x' and y' with respect to the global axis frame (x and y axes) by an angle ϕ_{gc}.

A number of solutions (~1300) have been calculated using different tilt angle, n-value, applied current condition and anisotropy ratio. The dimension of the LAC colony coincident with the global axes (branch 1) was 2×10^{-6} m by 30×10^{-6} m and the rotated colony (branch 2) approximately of dimension 2×10^{-6} m by 24×10^{-6} m, depending upon the angle of rotation. Both branches of the EOC geometry have lengths of 30×10^{-6} m and widths of 2×10^{-6} m. The colonies in the model are of approximately the same size as Bi-2223 colonies. The models have between 80×10^{3} and 120×10^{3} solution points. The value of the applied current injected into branch 1 and branch 2 of the LAC and EOC solutions presented, is the same. In the case of solutions to the LAC boundary model this leads to a current value, at the position of current egress, double that of either branch 1 or 2. The value of the applied current is presented in this chapter as a fraction of the critical current of branch 1.

In order to examine the relative ease of current flow in the different geometries of the LAC and EOC boundary models, an expression for the power consumption of the entire current flow distribution has been numerically calculated. The rate of Joule heating within a volume V subject to an electric field E and passing current density J is given by the expression

$$\int_V \mathbf{J}\bullet\mathbf{E}dV\ .$$

For unit width and uniform current flow across the plane formed by the z-axis and y-axis the above expression can be written in the form

$$\int_S \mathbf{J}\bullet\mathbf{E}dS \qquad (7.1)$$

where S is the area of volume V in the xy-plane. The total areas of different geometries are different and therefore lead to different values of the power consumption. For the purposes of comparison, the power consumption values given in this chapter are normalised with respect to the total area, S, over which they are calculated; this normalised value is referred to in this text as P_{gc}. The integral of the scalar product over S was calculated numerically using an adaptive recursive Newton-Cotes formula.

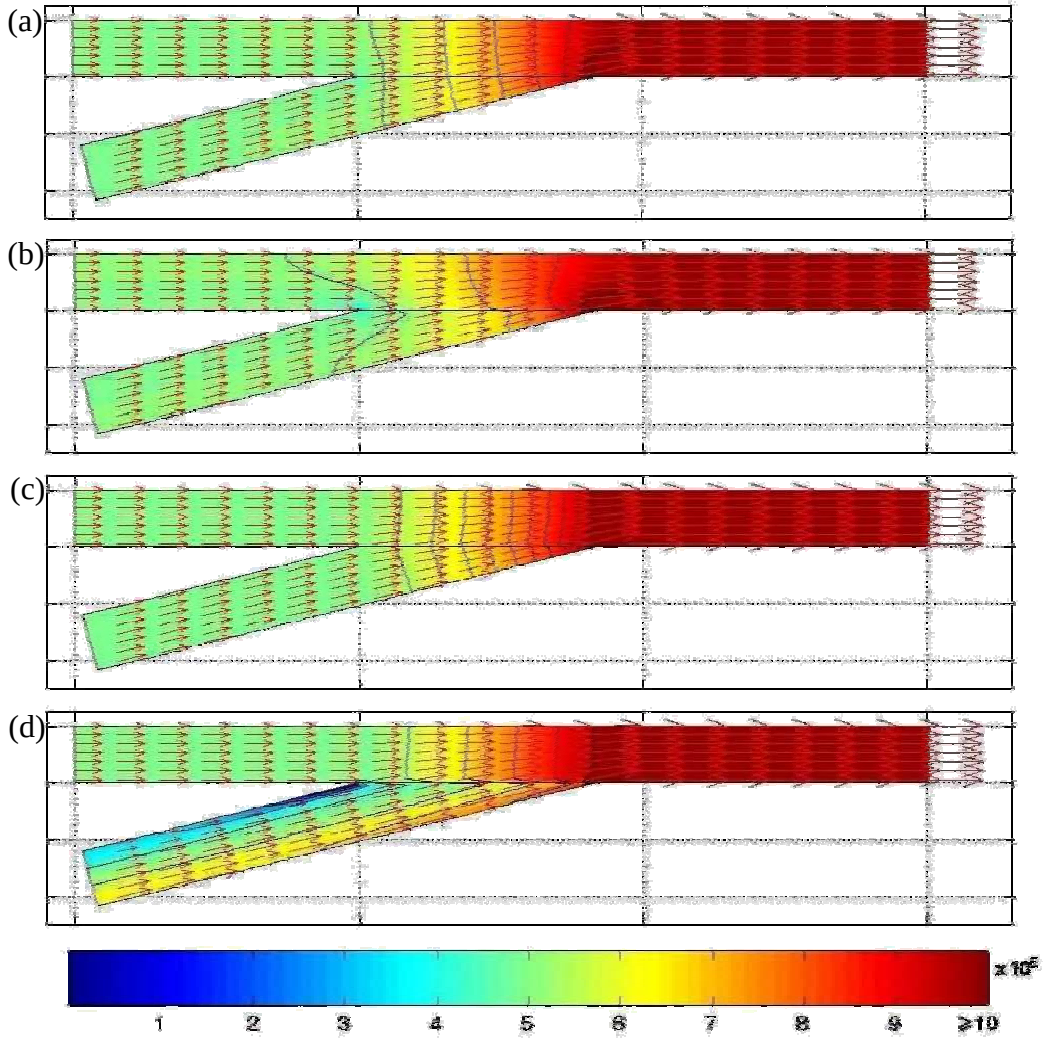

Figure 7.9
Current density distributions of the LAC boundary model. All the plots presented are of solutions with ϕ_{gc} =14 and $I_{app} = 1I_c$. Plots (a) and (b) are of solutions with n =1 and anisotropy ratios of 1 and 5 respectively. Plots (c) and (d) are of solutions with n =8 and anisotropy ratios of 1 and 5 respectively. The colourbar legend indicates the magnitude of the current density in A·m^{-2}. Arrows indicate current density vectors.

7.4.2 Current transfer in LAC boundaries

The geometry of the LAC boundary influences the current distribution in two principal ways. Firstly, the magnitude of the current density increases, from left to right of the LAC geometry, in the region of the connexion of branches 1 and 2, as the available cross section decreases. Secondly, across the interface from left to right of the LAC geometry the magnitude of the current density increases, as current flows along the shortest path between the point of current injection in branch 2 and the common point of egress in branch 1. Both of these geometrical influences lead to a local increase in the current density magnitude ('hotspot') in the vicinity of p_2 (see figure 7.1). The shorter path for current flow between the point of current injection and egress, via p_2, leads to a local

decrease in the magnitude of the current density ('coldspot') near p_1; a longer path for current traversal across the LAC geometry.

Figure 7.9 shows a comparison of the current distribution for $I_{app} = 1I_c$, in linear ($n = 1$) and nonlinear ($n = 8$) conductive media and in the isotropic ($\alpha = 1$) and anisotropic regimes ($\alpha = 5$). Current flow in the isotropic media is more uniform in both branches of the LAC boundary geometry, as indicated by the smaller degree of curvature in the contour lines of plots a and b in comparison to plots c and d of figure 7.9. The maximum value of the current density in the linear solution (see figure 7.9, plot b) is 45 % greater than the nonlinear solution (see figure 7.9, plot d) in the isotropic regime, and 98 % greater in the anisotropic regime. This is due to the exponential increase in power dissipation at hotspots in nonlinear models, which leads to more uniform current flow, as discussed in section 5.3.3, and is revealed by the smaller degree of curvature in the current density contour lines of plot a in comparison to plot c of figure 7.9.

In both the linear and nonlinear anisotropic cases the current distribution in branch two is non-uniform with a negative gradient in the magnitude of the current density across the width in a direction approximately normal to the inner bottom boundary of branch 2. This gradient is steeper in the nonlinear anisotropic case with a larger low current density region near p_2 (see figure 7.9, plot d).

As discussed previously, anisotropy introduces a proportionally larger dependence on the components of the local current density and therefore an increased spreading of current across the width, of a components current path, as current transfers in the component direction over a greater distance. This is exhibited by the larger extent of the region of non-uniform current along the axial direction of branch 2 (perpendicular to the local frame current density y'-component); the redistribution of current at the LAC boundary interface is accommodated by a greater non-uniformity of current flow in branch 2.

Figure 7.10 shows a comparison of the current distribution for anisotropic nonlinear ($\alpha = 5$, $n = 8$) solutions of the LAC boundary model with ϕ_{gc}=8, 10, 12, 14, 16, 20. I suggest two principal factors related to the angle ϕ_{gc} could influence the current redistribution with increasing ϕ_{gc} value. The current component across the LAC boundary interface increases with increasing ϕ_{gc}, this could lead to higher resistivity components at p_2 and therefore induce a more uniform distribution across the interface and thereby lead to a lower value of J at the hotspot. However, the interface cross section decreases with

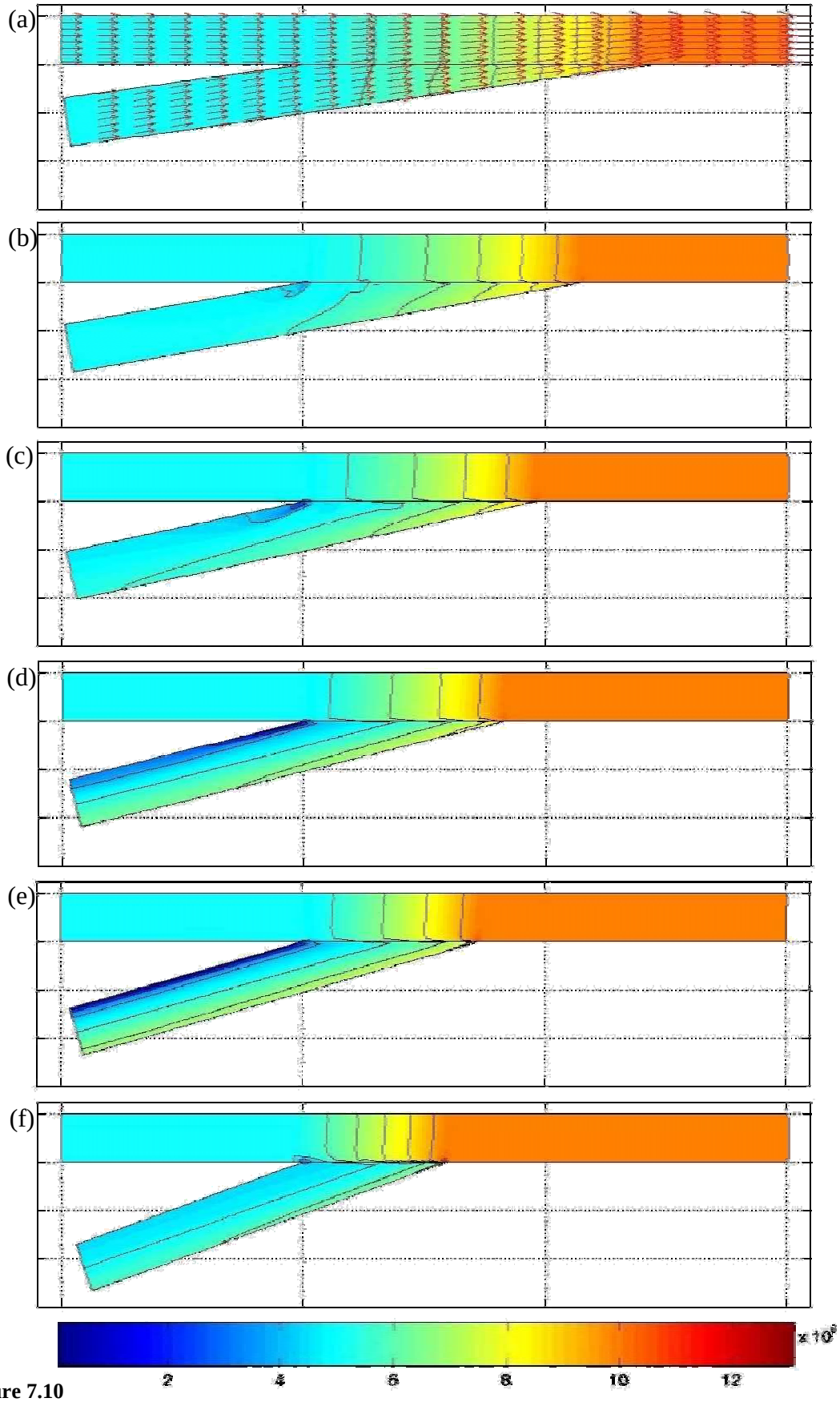

Figure 7.10
Current density distributions of the LAC boundary model. All the plots presented are of solutions with n =8 and $I_{app} = 1I_c$. Plots (a)-(f) are of solutions with α =5 and values of ϕ_{gc} =8, 10, 12, 14, 16, 20 respectively. The colourbar legend indicates the magnitude of the current density in A·m^{-2}. Arrows indicate current density vectors, and have been omitted from plots (b)-(f) for clarity.

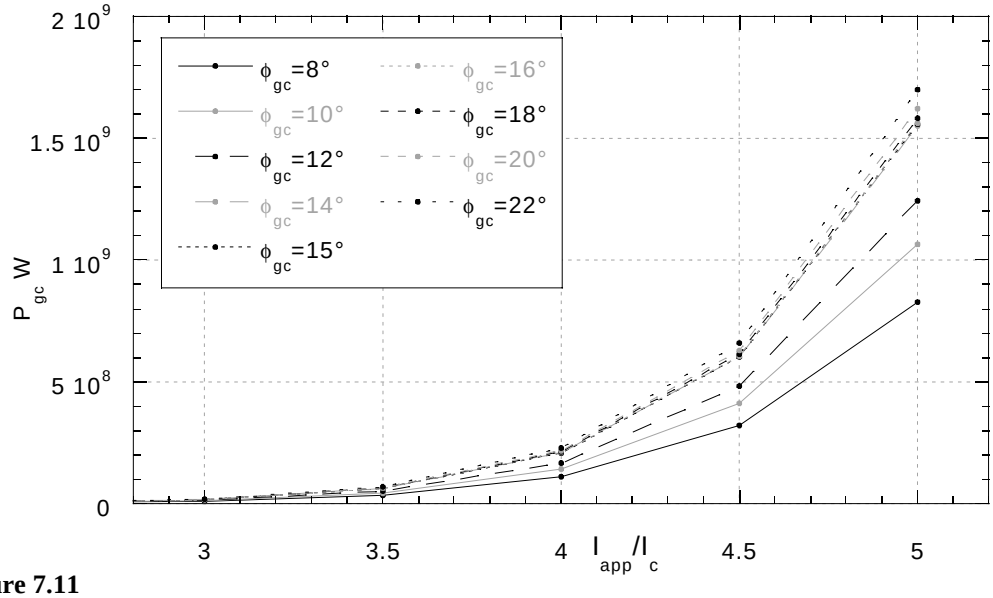

Figure 7.11
Plot of the normalised power dissipation, calculated from LAC boundary geometry solutions with n=8 and α=1 as a function of normalised applied current value, I_{app}/I_c, for grain/colony angles ϕ_{gc}=8, 10, 12, 14, 15, 16, 18, 20, 22.

increasing ϕ_{gc} which leads to a greater current density across the interface which should also engender a higher value of J at the hotspot. It is observed that the maximum value of J for the solutions plotted increases with increasing ϕ_{gc}. Analysis of current density plots for solutions with various applied current conditions, in the range $I_{app} = 0.5-5I_c$, reveals that there is no change in the current density distribution with increasing current for any solution combining the parameters $n = 1,\ 8$ and $\alpha = 1,\ 5$ with ϕ_{gc}=8, 10, 12, 14, 16, 20.

Figure 7.11 presents plots the normalised power dissipation calculated, from LAC boundary geometry solutions with n=8 and α=1 using equation (7.1), as a function of normalised applied current value, $P_{gc}\left(I_{app}/I_c\right)$, for colony/grain angles ϕ_{gc}=8, 10, 12, 14, 15, 16, 18, 20, 22. The curve $P_{gc}\left(I_{app}/I_c\right)$ has a strictly power law functional behaviour with integer exponent, directly related to the n-value by the expression $n+1$. As the angle between branch 1 and branch 2 increases the normalised power dissipation in the LAC boundary model increases and, as figure 7.11 shows, as ϕ_{gc} increases the curves $P_{gc}\left(I_{app}/I_c\right)$ for each angle lie increasingly close to one another, particularly above the 14° angle. This implies that the increase in normalised power dissipation with increasing ϕ_{gc}, plateau's at high values of ϕ_{gc}. The smaller increase of P_{gc} with increasing angle can be seen in the surface plot of figure 7.12 and occurs for all values of the normalised applied

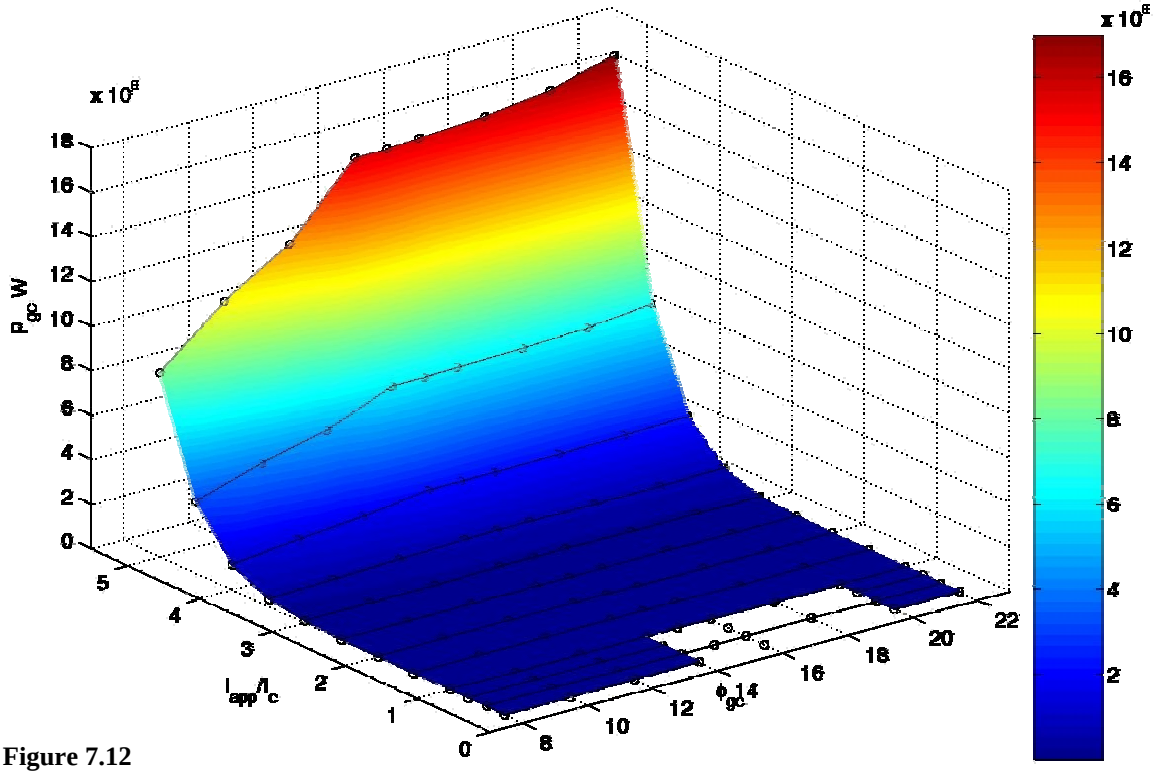

Figure 7.12
Surface plot of the normalised power dissipation, calculated from LAC boundary geometry solutions with n =8 and α =1 as a function of normalised applied current value, I_{app} / I_c, and colony/grain angle ϕ_{gc}. The colourbar legend indicates the magnitude of the normalised power dissipation in W.

current value, I_{app}/I_c. For a constant value of I_{app}/I_c, the curve $P_{gc}(\phi_{gc})$ is an empirical relation which is qualitatively the same for all values of I_{app}/I_c, as demonstrated by the constant value of the ratio $P_{gc}(\phi_{gc})/P_{gc}(\phi_{gc}=8)$ for increasing I_{app}/I_c value. The curve $P_{gc}(\phi_{gc})$ is also qualitatively the same for different n-values (n =1, 6, 8) and all plateau at 14°. The expression $P_{gc}(\phi_{gc})$ cannot be fitted by any common mathematical function, including the function $1/\sin(\phi_{gc})$ which relates the size of the contact cross sectional area to the angle between branch 1 and branch 2[14].

For solutions of the LAC boundary model, for which the superconductor EJ critical exponent is n, the normalised power dissipation can be expressed using the relation

$$P_{gc} \propto h(\phi_{gc})(I_{app}/I_c)^{n+1} \qquad (7.2)$$

where $h(\phi_{gc})$ is an empirical expression and can be deduced from the surface plot of figure 7.12. The relationship between P_{gc} and the anisotropy of the colonies/grains of the LAC boundary model is unclear. Plots of $P_{gc}(I_{app}/I_c)$ for a specified angle and different

anisotropy ratios (α=1, 3, 5) appear coincident and analysis of the coefficients of a power law, derived using Levenberg-Marquardt regressive curve fitting, shows no clear trend. This agrees with the conclusions drawn from measurements of YBCO boundaries grown on $SrTiO_3$ substrates, which suggest that the intrinsic anisotropy of the layered HTS system is not a principal cause of critical current degradation[20]. Only a small range of α has been studied compared to the range found in real HTS systems and this range may be inadequate to detect any dependence of P_{gc} on the parameter α. However, due to the nonlinearity of the EJ curves as measured for directions along the ab-plane and c-axis, an anisotropy value of 5 can make a difference in a local value of ρ_x and ρ_y of several orders of magnitude at values of J in excess of $J_{c,y}$.

The simple power law normalised current dependence of P_{gc} can be related to the general expression for power dissipation $P = EJ = \rho J^2$ by substituting the nonlinear constitutive relation equation (2.8) such that

$$P = \left(\frac{E_c}{J_c^{\,n}} \right) J^{n+1}.$$

The simple current dependence of P_{gc} is a consequence of the absence of any evolution of the current density distribution with increasing current such that the local power dissipation as represented by equation (7.2) also describes the global dissipation of power in the LAC boundary model. The abrupt change to an approximate plateau region of $P_{gc}\left(\phi_{gc}\right)$ at a value of ϕ_{gc} close to 14°, falls within the range of suggested values below which current transfer across grain boundaries is critically limited[2,14,21].

The simple dependence of $P_{gc}\left(I_{app}/I_c\right)$ on the value of n, for both linear and nonlinear regimes, the independence or weak dependence of P_{gc} on α and the same qualitative dependence of $P_{gc}\left(\phi_{gc}\right)$ on the value of n suggests that the dependence of P_{gc} on ϕ_{gc} is geometry dependent. To test this hypothesis, a study of the LAC boundary model with a different geometric dimension to that described previously has been performed. The alternative geometry is identical to that described previously with the exception that branch 2 is half the width (1×10^{-6} m) and longer by a factor of 1.5. Solutions for n=1, 8, α=1 and ϕ_{gc}=8, 10, 12, 14, 16, 20 have been calculated for two applied current conditions, one with equal applied current values in both branches and one with half the

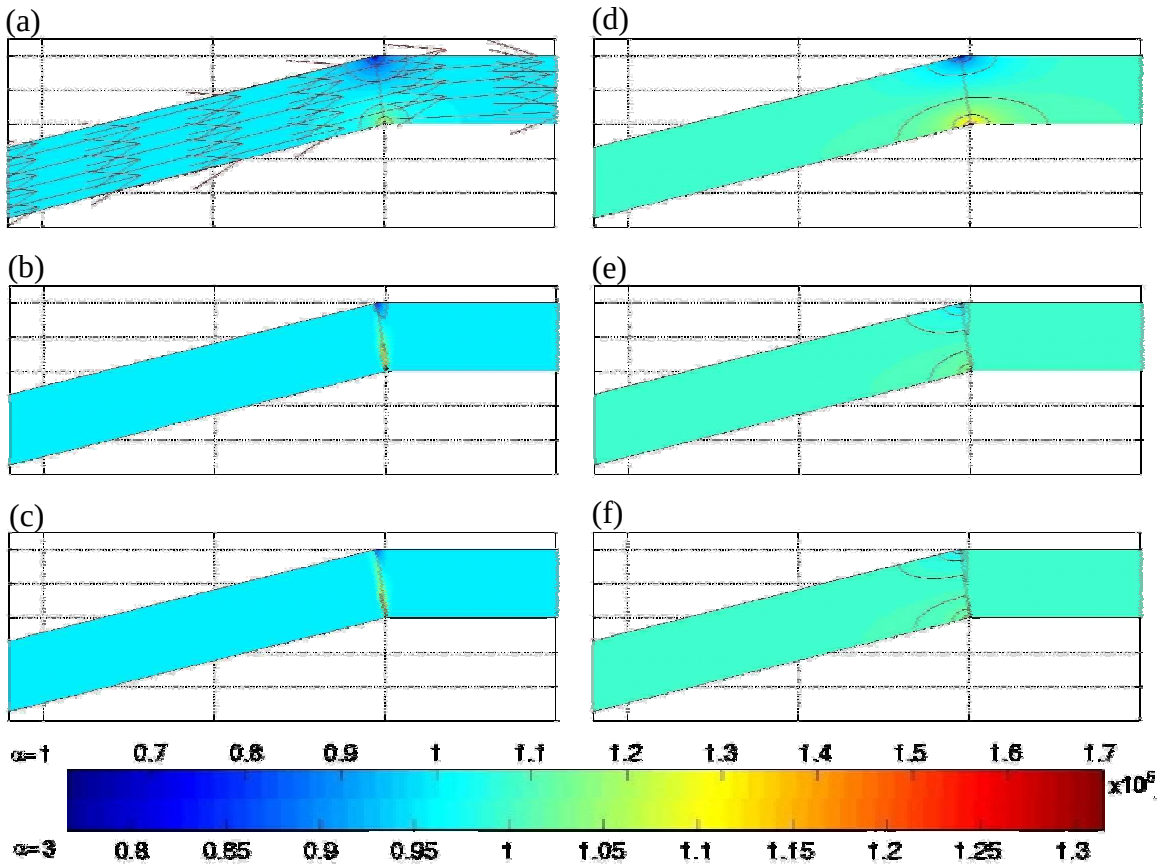

Figure 7.13
Current density distributions of the EOC boundary model. All the plots presented are of solutions with ϕ_{gc}=14 and $I_{app} = 1I_c$. Plots (a)-(c) are of solutions with α=1 and n-values of 1, 6, 8 respectively. Plots (d)-(f) are of solutions with α=3 and n-values of 1, 6, 8 respectively. The top scale of the colourbar legend indicates the magnitude of the current density in A·m^{-2} for plots (a)-(c) and the bottom scale refers to plots (d)-(f). Arrows indicate current density vectors, and have been omitted from plots (b)-(f) for clarity.

applied current value in branch 2. Solutions of the LAC boundary model with equal and unequal applied current conditions reveal a plateau at a critical value of ϕ_{gc}=10°. Any difference in the critical value of ϕ_{gc} for the two applied current conditions is smaller than 2°, the interval in ϕ_{gc} over which the models were calculated. The development of a plateau region is similar to that of the LAC model with the geometry described in section 7.4.1 and suggests that the geometry of the LAC boundary is the principal factor that determines the critical value of ϕ_{gc}.

7.4.3 Current transfer in EOC boundaries

Figure 7.13 shows a comparison of the current distribution in linear ($n = 1$) and nonlinear ($n = 6,\ 8$) conductive media in the isotropic ($\alpha = 1$) and anisotropic regimes ($\alpha = 3$) of the EOC boundary model. All the solutions exhibit a hotspot at the point p_2, which lies on the shortest path between the point of current injection in branch 2, and the point of egress

in branch 1. I suggest that the energy dissipation in the region of the hotspot is favoured by the system over the energy dissipation generated by shunting the same current via a longer path and therefore larger volume of resistive material. The EOC boundary models that employ nonlinearly conductive media have hot and cold spots, which occupy smaller regions than models that employ Ohmic conductive media; a consequence of a higher degree of current spreading across the width of the colony/grain in nonlinear models as indicated by the smaller maximum J value of the nonlinear solutions. The higher values of the components of the local resistivity of anisotropic solutions result in lower values of the maximum current density value for anisotropic solutions compared to isotropic solutions and greater spreading of the current density distribution along the branch axes of the EOC geometry, which increases with increasing n-value. Similar to the current distribution of the LAC boundary model, the current density distribution of the EOC boundary model is also independent of the value of the applied current in the range $I_{app} = 0.5 - 5 I_c$, for any solution combining the parameters $n = 1,\ 6,\ 8$ and $\alpha = 1,\ 3$ with ϕ_{gc}=8, 10, 12, 14, 16, 20.

Figure 7.14 shows a comparison of the current distribution of an anisotropic ($\alpha = 3$) and nonlinear ($n = 8$) solution of the EOC boundary model with $I_{app} = 1 I_c$ for ϕ_{gc}=8, 10, 12, 14, 16, 20. A hotspot occurs near p_2 as current flows preferentially along the shortest current path between the point of injection and the point of egress. The longitudinal extent of spreading of the current density distribution increases with increasing ϕ_{gc}. As discussed in section 7.4.2 the more redistribution necessary at the interface, the greater the non-uniformity of current flow in branch 2. The cross sectional area of the EOC interface boundary increases with increasing ϕ_{gc} as a function of $1/\cos(\phi_{gc}/2)$ and I suggest that the greater cross sectional area available for current transfer in the region of the interface is the cause of the decreasing observed maximum current density value with increasing ϕ_{gc}. Larger values of the component J_y at the interface in branch 2 could also be a contributing factor, as suggested in section 7.4.2.

The current dependence of P_{gc} is the same as the LAC boundary model and has a strictly power law functional behaviour with integer exponent, directly related to the n-value by the expression $n+1$. The normalised power dissipation of the EOC boundary model has no dependence on the parameter ϕ_{gc} in the range ϕ_{gc}=8-20. The coefficients of a power

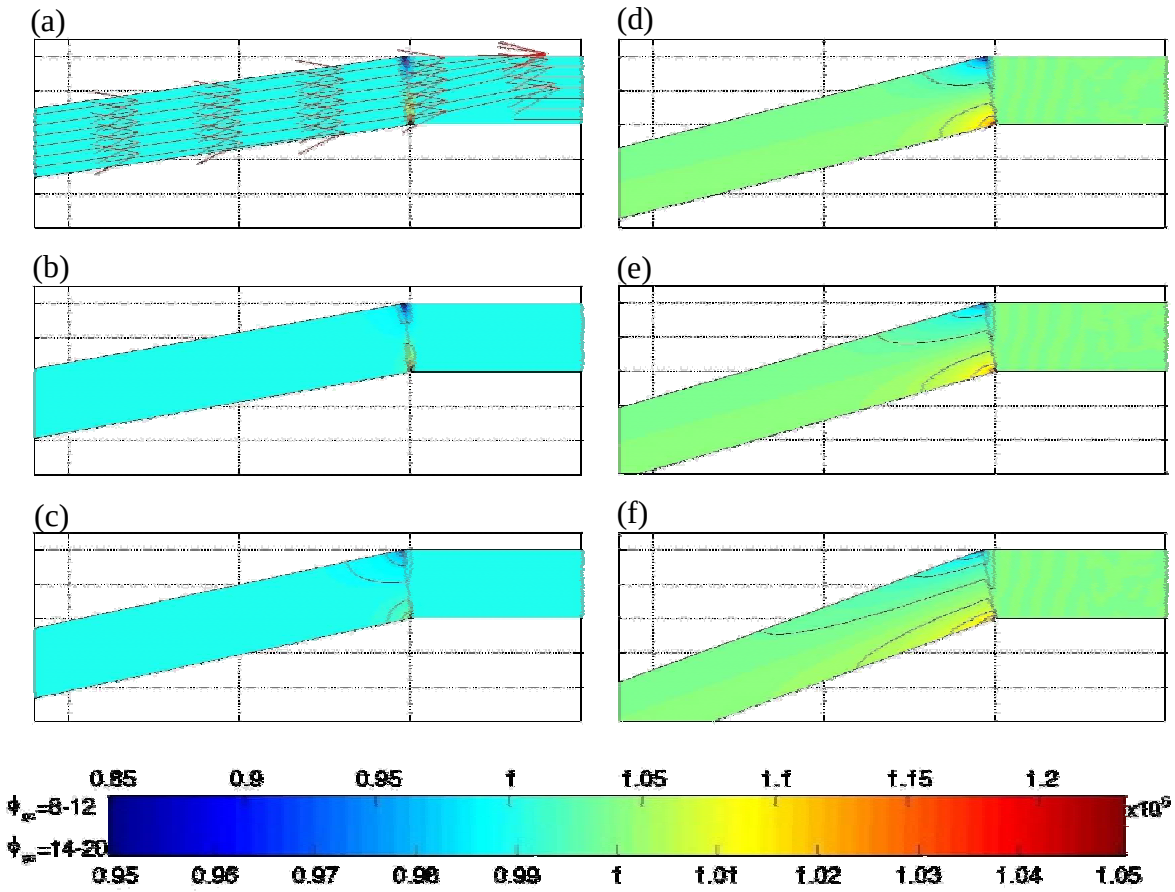

Figure 7.14
Current density distributions of the EOC boundary model. All the plots presented are of solutions with α=3, n=8 and $I_{app} = 1I_c$. Plots (a)-(f) are of solutions with values of ϕ_{gc}=8, 10, 12, 14, 16, 20 respectively. The top scale of the colourbar legend indicates the magnitude of the current density in A·m^2 for plots (a)-(c) and the bottom scale refers to plots (d)-(f). Arrows indicate current density vectors, and have been omitted from plots (b)-(f) for clarity.

law fit, using Levenberg-Marquardt curve regression, to plots of $P_{gc}\left(I_{app}/I_c\right)$ for various values of ϕ_{gc} have a constant value of 1457.1 and are independent of the value of n. A weak dependence of P_{gc} on ϕ_{gc} could be present, but not detectable, since the numerical integration of the solution is accurate only to the third significant figure.

The relationship between P_{gc} and the anisotropy of the colonies/grains of the EOC boundary model is, similar to the LAC boundary model, unclear. Plots of $P_{gc}\left(I_{app}/I_c\right)$ for a specified angle and different anisotropy ratios (α=1, 3) appear coincident and analysis of the coefficients of a power law, derived using Levenberg-Marquardt regressive curve fitting, again shows no clear trend. Assuming any weak dependence of P_{gc} on α is negligible, the normalised power dissipation can be expressed as the function

$$P_{gc} = 1457.1\left(I_{app}/I_c\right)^{n+1}. \qquad (7.3)$$

Again it is found that the local power dissipation, expressed by equation (7.3), also describes the total power dissipation of the LAC boundary model.

The normalised power dissipation is approximately half that of the LAC model for solutions with the same value of ϕ_{gc}, α and I_{app}/I_c, indicating the EOC colony/grain boundary affords easier current transfer. Comparison of the normalised power dissipation in linear and nonlinear solutions of the LAC and EOC models indicates that power dissipation estimates of HTS systems based on approximations using Ohmic conductors may exaggerate the total power dissipation for applied currents below I_c and greatly underestimate the power dissipation above I_c. However, approximations which ignore the complex current density distributions accurately relate the normalised power dissipation and the applied current for a specific value of n.

7.5 Summary

A review of the brick-wall and railway-switch models of current transfer in polycrystalline HTSs has been presented. Models of current transfer between c-axis, low-angle c-axis and edge-on c-axis tilt oriented grain interfaces have been developed and solved to provide quantitative and qualitative descriptions of current flow in polycrystalline HTSs. The current density distribution in small sections of a weak link brick-wall microstructure has been solved and plotted as an aid to the conceptualisation of current flow. Comparison of current flow in Ohmic and nonlinear models of the brick-wall microstructure shows different qualitative behaviour. It has been shown that, with increasing aspect ratio, the region of uniform current flow in the middle of the brick-wall ab-plane interface develops over a shorter distance from the point of current injection and extends over a greater proportion of the unit cell length. Consideration of the path of maximal current transfer in the brick-wall unit cell has revealed that, across the ab-plane brick interface, the path moves from the midpoint of the brick-wall unit cell towards the point of current injection for increasing values of n and α.

It has been suggested that the geometry of the LAC and EOC boundary models is the principal factor that determines the current distribution in these geometries. Power dissipation, and by association the ease of current transfer, in the LAC and EOC boundary models can be expressed by a simple power law directly related to the n-value by the expression $n+1$, indicating that local power dissipation also describes the global power dissipation in the LAC boundary model. Power dissipation in both the LAC and EOC

models has been found to possess a weak dependence or independence on the anisotropy ratio α. Finally, the EOC boundary model has lower power dissipation than the LAC boundary model for the same set of solution parameters.

7.6 References

1 L. N. Bulaevskii, L. L. Daemen, M. P. Maley, and J. Y. Coulter, Physical Review B-Condensed Matter **48,** 13798-13816 (1993).

2 A. E. Pashitski, A. Gurevich, A. A. Polyanskii, D. C. Larbalestier, A. Goyal, E. D. Specht, D. M. Kroeger, J. A. DeLuca, and J. E. Tkaczyk, Science **275,** 367-369 (1997).

3 N. Adamopoulos, PhD Thesis, Cambridge, 1994.

4 F. Pardo, D. Lopez, F. Delacruz, P. Statstny, and F. C. Matacotta, Physica B **194,** 2013-2014 (1994).

5 D. Dimos, P. Chaudhari, and J. Mannhart, Physical Review B-Condensed Matter **41,** 4038-4049 (1990).

6 B. Hensel, G. Grasso, and R. Flukiger, Physical Review B-Condensed Matter **51,** 15456-15473 (1995).

7 O. Eibl, Microscopy Research and Technique **30,** 218-245 (1995).

8 Y. H. Li, J. A. Kilner, M. Dhalle, A. D. Caplin, G. Grasso, and R. Flukiger, Superconductor Science & Technology **8,** 764-768 (1995).

9 M. P. Maley, J. H. Cho, J. Y. Coulter, J. O. Willis, L. N. Bulaevskii, L. R. Motowidlo, and P. Haldar, Ieee Transactions On Applied Superconductivity **5,** 1290-1293 (1995).

10 R. Kleiner and P. Muller, Physical Review B-Condensed Matter **49,** 1327-1341 (1994).

11 B. Hensel, G. Grasso, and R. Flukiger, Journal Of Electronic Materials **24,** 1877-1881 (1995).

12 L. N. Bulaevskii, J. R. Clem, L. I. Glazman, and A. P. Malozemoff, Physical Review B-Condensed Matter **45,** 2545-2548 (1992).

13 J. H. Cho, M. P. Maley, J. O. Willis, J. Y. Coulter, L. N. Bulaevskii, P. Haldar, and L. R. Motowidlo, Applied Physics Letters **64,** 3030-3032 (1994).

14 B. Hensel, J. C. Grivel, A. Jeremie, A. Perin, A. Pollini, and R. Flukiger, Physica C **205,** 329-337 (1993).

15 D. P. Grindatto, B. Hensel, G. Grasso, H. U. Nissen, and R. Flukiger, Physica C **271,** 155-163 (1996).

16 A. Goyal, E. D. Specht, D. M. Kroeger, T. A. Mason, D. J. Dingley, G. N. Riley, and M. W. Rupich, Applied Physics Letters **66,** 2903-2905 (1995).

17 A. D. Caplin, L. F. Cohen, M. N. Cuthbert, M. Dhalle, D. Lacey, G. K. Perkins, and J. V. Thomas, Ieee Transactions On Applied Superconductivity **5,** 1864-1869 (1995).

18 M. Dhalle, M. Cuthbert, M. D. Johnston, J. Everett, R. Flukiger, S. X. Dou, W. Goldacker, T. Beales, A. D. Caplin, Superconductor Science & Technology **10,** 21-31 (1997).

19 Y. M. Zhu, Q. Li, Y. N. Tsay, M. Suenaga, G. D. Gu, and N. Koshizuka, Physical Review B-Condensed Matter **57,** 8601-8608 (1998).

20 M. Prester, Superconductor Science & Technology **11,** 333-357 (1998).

21 D. Dimos, P. Chaudhari, J. Mannhart, F. K. Legoues, Physical Review Letters **61,** 219-222 (1988).

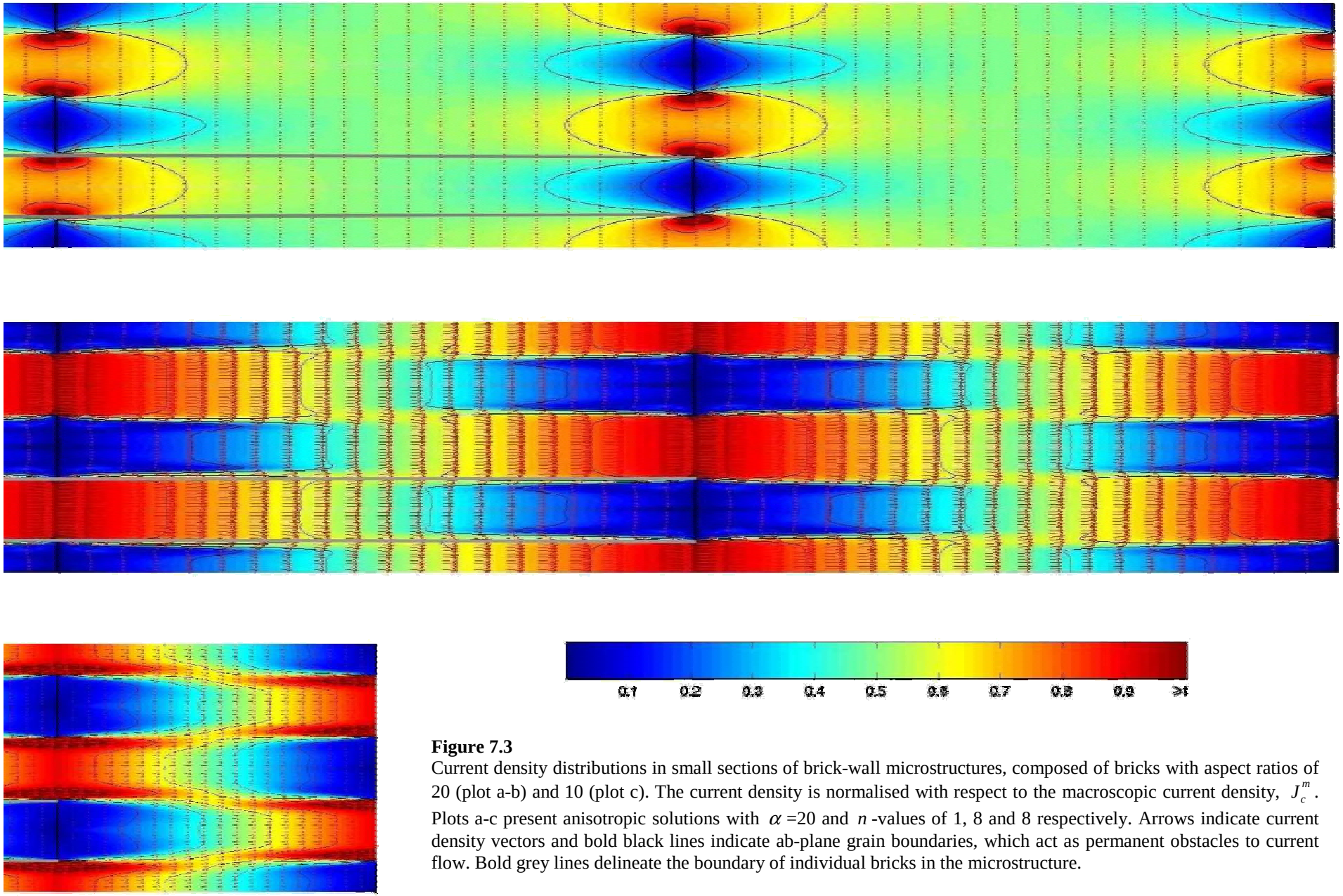

Figure 7.3
Current density distributions in small sections of brick-wall microstructures, composed of bricks with aspect ratios of 20 (plot a-b) and 10 (plot c). The current density is normalised with respect to the macroscopic current density, J_c^m. Plots a-c present anisotropic solutions with α=20 and n-values of 1, 8 and 8 respectively. Arrows indicate current density vectors and bold black lines indicate ab-plane grain boundaries, which act as permanent obstacles to current flow. Bold grey lines delineate the boundary of individual bricks in the microstructure.

CHAPTER 8

Conclusions and future development

8.1 Conclusions

This thesis has presented a study of current flow in high-T_c superconductors by treating the superconducting components of electrically conductive systems as anisotropic nonlinear conductive media. Current transfer in bulk HTSs can be characterised by different mechanisms on various spatial scales. This thesis has examined current transfer from the scale of bulk devices to the scale of macroscopic defects within superconducting devices, and on to the microscopic scale of colony/grain connexions. The conceptual picture of current flow in these superconducting systems is typically based upon descriptions of current flow in Ohmic media, and as such is misleading and inaccurate. It has been shown that current flow in nonlinear media limits current crowding and that this results in a spreading of current over a greater region of the conductor than in linear media. Anisotropy introduces a proportionally larger dependence on the components of the local current density and therefore an increased spreading of current across the width of a components current path.

This work has relied upon the successful development of numerical models of current transfer and has shown by exhaustive intuitive model, analytical model, and experimental comparisons, that the Galerkin FE method can be used to model current transfer in superconducting systems. The range, value and functionality of suitable input parameters for models of the macroscopic behaviour of the Bi-2212 CRT material have been studied. The development of new experimental and mathematical techniques to investigate the self-field effect has allowed confirmation of the FE model assumption that the self-field effect is negligible in the Bi-2212 CRT system.

The behaviour of current flow in current contacts to superconducting components is of considerable technological importance. This macroscopic current transfer problem has been examined and good consistency between various numerical, analytical and experimental results has been demonstrated. It has been found that the bulk resistivity, of the superconducting component of *in-situ* and lap contacted devices, adds a nonlinear

component to the contact resistivity. For currents approximately in excess of the critical current of a device this bulk component becomes significant and results in a nonlinear increase of the contact interface resistance and current transfer length. Modelling also reveals that the region of maximum current density within the superconducting component is at a position removed from the point of initial metal-HTS contact and is likely to be the site from which thermal quenching of the superconductor propagates in the event of inadequate local cooling power. A greater contact metal resistivity and/or anisotropy value (better texturing) has been shown to lead to an increase in the degree of nonlinear effects at smaller applied currents. On the scale of an individual device, the electrically conductive media of a superconductor has been assumed to homogeneous. However, on the local scale of macroscopic inhomogeneities within a bulk superconducting device, defects can have a long-range effect on the current distribution, which increases in range for increasing values of n and anisotropy ratio.

Current transfer on the microscopic scale of colony/grain connexions has been examined in the context of the brick-wall and railway-switch models. Solutions of a model of current flow in the brick-wall microstructure reveal that, with increasing aspect ratio, uniform current flow along the ab-plane interface develops over a shorter distance from the point of current injection and extends over a greater proportion of the interface. This region of uniform current flow tends to zero for values of the critical current anisotropy approximately in excess of the colony/grain aspect ratio; for this condition, c-axis current components transfer across the entire interface. Further, the path of maximal current transfer, across the ab-plane interface, moves from the midpoint of the brick-wall interface region towards the point of current injection for increasing values of n and α. Examination of the principal current transfer elements of the railway-switch model has shown that the global power dissipation within these elements can be described by a simple nonlinear local power dissipation expression, which has either a weak dependence or independence on the critical current anisotropy ratio. Numerical modelling of low-angle c-axis and edge-on c-axis colony/grain connexions demonstrates that the latter provides a path for lower dissipation of current transfer. It is suggested that the principal factor that determines the ease of current transfer within these two colony/grain connexions is the colony/grain connexion geometry.

8.2 Future development

The work presented could be developed in two ways. Firstly, a considerable number of current flow problems could be investigated using the programs developed in this work, some of which are suggested as the basis for further work at the end of this section. Secondly, by further development of the computer programs more complex current flow problems could be examined. Such problems include the effect of a local magnetic field dependence of the critical current, the transient response of current flow problems, and the effect local heating and heat transfer can have on the current transfer properties of a superconducting system.

Thorough research of the often myriad available methods must be instigated when determining the best method to implement a modification to the numerical model and the limitations of the methods employed must be taken into consideration when constructing new problems to solve. The models in this thesis have proven to give very complex behaviour and adding further functionality to the model may produce results from which no clear physical insight or general behaviour can be inferred. For this reason, solutions involving a weakly nonlinear self-field dependence in the nonlinear resistivity term (as discussed in section 4.3.1) were not studied. I suggest that such developments should only be pursued after the current flow of the specific problem is fully understood.

With more computing power, the transient solution of some complex systems could be investigated. The Hitachi SR2201 vector parallel processor at the Cambridge University computing centre can readily execute programs written in either Fortran or C and thereby avoids the necessity of learning the complex message-passing interface language standard that is used on parallel processing machines. Although C code typically executes a factor of 10 slower than Fortran, a Matlab to C compiler is available, that can convert Matlab scripts and functions to C code. This would clearly enable faster and easier implementation of the existing programs on vector parallel processing platforms.

For high applied currents, local heating can become an important factor in superconducting device design. Local heating within a superconductor increases cooling power costs and can lead to localised thermal quenching. The existing programs could be modified to take into account the local heating effect by introducing a power dependent thermal conductivity term in a coupled heat transfer model, the temperature variation of which is a dependent variable of the electrical conductivity term in the current model. A coupled heat and electrical conduction model must be developed, since incorporating a

power dependence in the local resistivity term assumes the superconducting material is adiabatic on a local scale. Electrical conduction and heat conduction are analogous systems and can be described by the same PDE. This has the advantage that the suit of programs used to calculate current flow could be used to calculate both the current flow and heat transfer components of the coupled system.

The existing programs could also be modified to provide a quasi-3D solution of a modelled geometry that accounts for changes in the width of a sample. This could be performed by multiplying the resistivity function by a spatially dependent function that determines the z-axis depth of the geometry, $f(x,y)$. This is only a quasi-3D analysis as the current flow is assumed uniform along the z-axis direction.

There are a number of current flow problems which could be modelled using the programs developed in this thesis. The studies presented have assumed the superconducting material to be homogeneous. A study of current sharing between nonlinear conductive bodies with different n-values and/or J_c would allow for comparison of the relative significance of these factors for inhomogeneous materials. Current sharing between a HTS component and a normal metal substrate has been analysed in the vicinity of the initial contact region. However, a more detailed study of current flow at a point removed from the contact region could examine the behaviour of current flow at defects in HTSs and at the HTS normal metal interface. This could be useful in assessing current limiting mechanisms in PIT, dip coated, and other bulk HTS systems.

Appendix A

A.1 Field dependence of the critical current at different field values

Consider an arbitrary field profile $f(x)$. Given the assumed symmetry of the magnetic field profile considered in section 3.5.2, we have

$$
\begin{aligned}
&f(0)=0\\
&f(x)=-f(-x)\\
&f^{(1)}(x)=f^{(1)}(-x)\\
&f^{(2)}(x)=-f^{(2)}(-x)\\
&\ldots\\
&f^{(n)}(x)=f^{(n)}(-x),\ n=1,3\ldots\\
&f^{(n)}(x)=-f^{(n)}(-x),\ n=0,2\ldots
\end{aligned}
$$

where $f^{(n)}(x)$ is the *n*th derivative of $f(x)$.

At an applied magnetic field, the field profile is given by the function $f(x+\delta)$, since $f(x)$ is displaced by an amount δ and we can then write

$$
\begin{aligned}
f(x+\delta)&=\sum_{n=0}^{\infty}\frac{\delta^n}{n!}f^{(n)}(x)\\
f(a+\delta)&=\sum_{n=0}^{\infty}\frac{\delta^n}{n!}f^{(n)}(a)\\
f(-a+\delta)&=\sum_{n=0}^{\infty}\frac{\delta^n}{n!}f^{(n)}(-a).
\end{aligned}
$$

Since $\Delta H=f(a+\delta)-f(-a+\delta)$ and $H_{app}=\left[f(a+\delta)+f(-a+\delta)\right]/2$, we have

$$
\begin{aligned}
\Delta H(\delta)&=2\sum_{n=0,2.4\ldots}^{\infty}\frac{\delta^n}{n!}f^{(n)}(a)\\
H_{app}(\delta)&=\sum_{n=1,3,5\ldots}^{\infty}\frac{\delta^n}{n!}f^{(n)}(a)
\end{aligned}
\qquad \text{(A.1)}
$$

and therefore

$$\frac{d(\Delta H)}{dH_{app}} = \frac{d(\Delta H)}{d\delta}\frac{d\delta}{dH_{app}} = 2\frac{\sum_{n=2,4\ldots}^{\infty}\frac{\delta^{n-1}}{(n-1)!}f^{(n)}(a)}{\sum_{n=1,3\ldots}^{\infty}\frac{\delta^{n-1}}{(n-1)!}f^{(n)}(a)}.$$

In addition, at the point of inflection, the slope of the field profile at the surface A is $df(x)/dx\big|_{x=0}$ since the profile has been displaced half the thickness of the sample, and from

$$\left.\frac{df(x)}{dx}\right|_{x=0} = \frac{dH_A}{d\delta} \text{ and } H_A = H_{app} - \frac{\Delta H}{2},$$

we have

$$J(0) = \left.\frac{df(x)}{dx}\right|_{x=0} = \frac{dH_{app}}{d\delta}\left(1 - \frac{1}{2}\frac{d(\Delta H)}{dH_{app}}\right).$$

Substituting $a+\delta$ in equation (A.1) gives

$$H_{app} = (a+\delta)f^{(1)}(a) + \frac{(a+\delta)^3}{3!}f^{(3)}(a) + \ldots,$$

from which we have the result

$$\frac{dH_{app}}{d\delta} = f^{(1)}(a) + \frac{(a+\delta)^2}{2}f^{(3)}(a) + \ldots.$$

By neglecting terms above the second derivative, and using the fact that $f^{(1)}(a) = J\left(H_{sf,x=a}\right) = J(\Delta H/2)$, where $H_{sf,x=a}$ is the field at $x=a$ at zero applied field and ΔH_{sf} is the value of ΔH at zero applied field, we get the expression of section 3.5.2,

$$J(0) = J\left(\frac{\Delta H_{\max}}{2}\right)\left(1 - \frac{1}{2}\left.\frac{d(\Delta H)}{dH_{app}}\right|_{H_{app}=H^*}\right).$$

Appendix B

B.1 The linear triangular element and shape function

A typical triangular element is defined by nodes (or solution points) l, m, n at the vertices with positions $(x_l, y_l), (x_m, y_m), (x_n, y_n)$, joined by straight-line boundaries. A linear variation of the solution is assumed throughout the element, with the solution possessing one degree of freedom at each node. The solution at any position x, y within the element can be represented by the simple polynomial

$$\hat{u} = \alpha_1 + \alpha_2 x + \alpha_3 y .$$

If the nodes l, m, n are numbered 1,2,3 then the values at those nodes are

$$\left.\begin{array}{ll} \hat{u} = u_1 & \text{at } x = x_1, y = y_1 \\ \hat{u} = u_2 & \text{at } x = x_2, y = y_2 \\ \hat{u} = u_3 & \text{at } x = x_3, y = y_3 \end{array}\right\}$$

and thus

$$\left.\begin{array}{l} u_1 = \alpha_1 + \alpha_2 x_1 + \alpha_3 y_1 \\ u_2 = \alpha_1 + \alpha_2 x_2 + \alpha_3 y_2 \\ u_3 = \alpha_1 + \alpha_2 x_3 + \alpha_3 y_3 \end{array}\right\}. \qquad \text{(B.1)}$$

Solving for $\alpha_1, \alpha_2, \alpha_3$ gives

$$\begin{aligned} \alpha_1 &= \left(\frac{1}{2A^e}\right)\left[(x_2 y_3 - x_3 y_2)u_1 + (x_3 y_1 - x_1 y_3)u_2 + (x_1 y_2 - x_2 y_1)u_3\right] \\ \alpha_2 &= \left(\frac{1}{2A^e}\right)\left[(y_2 - y_3)u_1 + (y_3 - y_1)u_2 + (y_1 - y_2)u_3\right] \qquad \text{(B.2)} \\ \alpha_3 &= \left(\frac{1}{2A^e}\right)\left[(x_3 - x_2)u_1 + (x_1 - x_3)u_2 + (x_2 - x_2)u_3\right]. \end{aligned}$$

Where A^e is the element area defined by

$$2A^e = (x_1 y_2 - x_2 y_1) + (x_3 y_1 - x_1 y_3) + (x_2 y_3 - x_3 y_2).$$

Combining (B.1) and (B.2) provides an approximation for u over the element in terms of the nodal values

$$\hat{u} = N_1^e u_1 + N_2^e u_2 + N_3^e u_3 \qquad \text{(B.3)}$$

where the shape functions N_1^e, N_2^e, N_3^e are given by

$$N_1^e(x,y) = \left(\frac{1}{2A^e}\right)\left[(x_2y_3 - x_3y_2) + (y_2 - y_3)x + (x_3 - x_2)y\right]$$

$$N_2^e(x,y) = \left(\frac{1}{2A^e}\right)\left[(x_3y_1 - x_1y_3) + (y_3 - y_1)x + (x_1 - x_3)y\right]$$

$$N_3^e(x,y) = \left(\frac{1}{2A^e}\right)\left[(x_1y_2 - x_2y_1) + (y_1 - y_2)x + (x_2 - x_1)y\right].$$

The approximation for the element, with domain Ω^e and nodes l,m,n can be represented more succinctly in the form

$$u \approx \hat{u} = \sum_{\Omega^e}^{i=l,m,n} N_i^e(x,y)a_i^e = \begin{bmatrix} N_l^e & N_m^e & N_n^e \end{bmatrix}\begin{Bmatrix} a_l^e \\ a_m^e \\ a_n^e \end{Bmatrix} = \mathbf{N}^e\mathbf{a}^e \qquad \text{(B.4)}$$

where the components of the matrix $\mathbf{N}^e$ are the shape functions ($\mathbf{N}^e$ is also referred to as the shape function) and $\mathbf{a}^e$ represents the nodal values of the solution variables on a particular element. The functions $\mathbf{N}^e$ naturally maintain continuity at the element boundaries in that they satisfy the following condition

$$N_i^e(x_l, y_l) = 1$$

while

$$N_i^e(x_m, y_m) = N_i^e(x_n, y_n) = 0\text{, etc.}$$

The shape functions preserve the nodal values of the function at the node positions; i.e. $N_i^e = 1$ at x_l and y_l but zero at other vertices, and similarly for the other nodal sites[1].

B.2 References

1 O. C. Zienkiewicz, *The Finite element method*, Vol. 1, 4th ed. (McGraw-Hill, London, 1989-1991).

Appendix C

C.1 Published papers

R. P. Baranowski, D. R. Watson, and J. E. Evetts, Institute of Physics Conference Series**,** 1619-1622 (1997).

M. Chen, D. M. Glowacka, B. Soylu, D. R. Watson, J. K. S. Christiansen, R. P. Baranowski, B. A. Glowacki, and J. E. Evetts, Ieee Transactions On Applied Superconductivity **5,** 1467-1470 (1995).

B. Soylu, J. Christiansen, D. M. Astill, R. P. Baranowski, J. Engel, and J. E. Evetts, Institute Of Physics Conference Series **148,** 135-138 (1995).

P. Kosmetatos, A. Kursumovic, D. R. Watson, R. P. Baranowski, and J. E. Evetts, Institute Of Physics Conference Series**,** 1049-1052 (1997).

C.2 Submitted papers

A. Kursumovic, R. P. Baranowski, and J. E. Evetts, Accepted for publication in the Journal of Applied Physics (1999).

R. P. Baranowski, A. Kursumovic, and J. E. Evetts, Submitted to the Institute of Physics Conference Series (1999).